

# Vortex generators and turbulent boundary layer separation control

by

Ola Lögdberg

October 2006  
Technical Reports from  
Royal Institute of Technology  
KTH Mechanics  
SE-100 44 Stockholm, Sweden

Akademisk avhandling som med tillstånd av Kungliga Tekniska Högskolan i Stockholm framlägges till offentlig granskning för avläggande av teknologie licenciatexamen fredagen den 3:e november 2006 kl 10:30 i sal E36, KTH, Vallhallavägen 79, Stockholm.

©Ola Lögdberg 2006

Universitetsservice US-AB, Stockholm 2006

## **Vortex generators and turbulent boundary layer separation control**

### **Ola Lögdborg, 2006**

Linné Flow Centre  
KTH Mechanics  
SE-100 44 Stockholm, Sweden

### **Abstract**

Boundary layer separation is usually an unwanted phenomenon in most technical applications as for instance on airplane wings, on ground vehicles and in internal flows such as diffusers. If separation occurs it leads to loss of lift, higher drag and results in energy losses. It is therefore important to be able to find methods to control and if possible avoid separation altogether without introducing a too heavy penalty such as increased drag, energy consuming suction etc.

In the present work we study one such control method, namely the use of vortex generators (VGs), which are known to be able to hinder turbulent boundary layer separation. We first study the downstream development of streamwise vortices behind pairs and arrays of vortex generators and how the strength of the vortices is coupled to the relative size of the vortex generators in comparison to the boundary layer size. Both the amplitude and the trajectory of the vortices are tracked in the downstream direction. Also the influences of yaw and free stream turbulence on the vortices are investigated. This part of the study is made with hot-wire anemometry where all three velocity components of the vortex structure are measured. The generation of circulation by the VGs scales excellently with the VG blade height and the velocity at the blade edge. The magnitude of circulation was found to be independent of yaw angle.

The second part of the study deals with the control effect of vortex generators on three different cases where the strength of the adverse pressure gradient (APG) in a turbulent boundary layer has been varied. In this case the measurements have been made with particle image velocimetry. It was found that the streamwise position where the VGs are placed is not critical for the control effect. For the three different APG cases approximately the same level of circulation was needed to inhibit separation. In contrast to some previous studies we find no evidence of a universal detachment shape factor  $H_{12}$ , that is independent of pressure gradient.

**Descriptors:** Turbulent boundary layer separation, adverse pressure gradient, vortex generators, control of separation



## Preface

Parts of this work have been published in:

LÖGDBERG, O. & ALFREDSSON, P.H. 2005 Turbulent boundary layer separation-passive control. In *4th International Symposium on Turbulence and Shear Flow Phenomena. Vol 2*, 549-554

LÖGDBERG, O. 2006 Flow control in an adverse pressure gradient boundary layer. In *Euromech Fluid Mechanics Conference 6* p. 374

October 2006, Stockholm

*Ola Lögdberg*



# Contents

<b>Abstract</b>	iii
<b>Preface</b>	v
<b>Chapter 1. Introduction</b>	1
1.1. Truck aerodynamics	2
1.2. Objectives	7
<b>Chapter 2. Turbulent boundary layers, separation and separation control</b>	8
2.1. Some basic concepts	8
2.2. Turbulent boundary layers	10
2.3. Separation	11
2.4. Separation control	13
<b>Chapter 3. Experimental set up</b>	21
3.1. Wind tunnels	21
3.2. Measurement techniques	24
3.3. Vortex generators	30
<b>Chapter 4. Zero pressure gradient experiments</b>	34
4.1. The turbulent boundary layer without vortex generators	34
4.2. The turbulent boundary layer with vortex generators	35
<b>Chapter 5. Adverse pressure gradient experiments</b>	73
5.1. Description of the test flow	73
5.2. Uncontrolled case	74
5.3. Controlled case	85
<b>Chapter 6. Conclusions</b>	104

<b>Acknowledgements</b>	106
<b>References</b>	107

## CHAPTER 1

# Introduction

With the increase in oil prices and the increased environmental concerns, regarding both toxic exhausts, particulates and green house gases, the reduction of fuel consumption is an important issue both for vehicle manufactures and those who utilise the vehicles. Large improvements have been made over the last decades in terms of engine efficiency, aerodynamic drag etc. but there is still possibilities for future improvements. This thesis deals with a fundamental aerodynamic problem, namely how to control flow separation, a phenomenon that in most cases lead to increased aerodynamic drag. It is an experimental wind tunnel study where an advanced optical measurement technique has been used to study the separated flow with a without so called vortex generators. Vortex generators are in common use on the upper side of the wing of many commercial aircraft to avoid separation during take-off and landing. The present study aims at developing a fundamental knowledge of such vortex generators in order to be able to optimize their size and position in applications. The results may be useful in many engineering situations, but the work is motivated by the possibility to reduce the aerodynamic drag on long haulage trucks.

In the thesis this introductory chapter gives a background to truck aerodynamics, how it influences the economy of truck operation and some measures that have been undertaken in order to improve future designs. Also the objectives of the current study are given. Chapter 2 gives a review of turbulent boundary layers both for zero pressure gradient and adverse pressure gradients for which flow separation may occur and it also reviews previous work on separating turbulent boundary layers. Finally this chapter also discusses various forms of flow control methods that have been employed in order to hinder or mitigate flow separation. Chapter 3 describes the various experimental set-ups that have been used, including two wind tunnels and the experimental measurement techniques.

In chapter 4 the flow dynamics of the vortex generators that have been used are studied in detail in a zero-pressure gradient boundary layer using hot-wire anemometry and flow visualisation. Three different adverse gradient boundary layers have been studied and in the first part of chapter 5 they are described and the results are compared with other studies. In this case all



FIGURE 1.1. The author performing a smoke visualisation on a Scania truck in the German-Dutch LLF wind tunnel in 2001. The largest test section with a cross sectional area of  $9.5 \times 9.5 \text{ m}^2$  is used for this test.

velocity measurements are taken using Particle Image Velocimetry (PIV). In the second part of chapter 5 various set-ups using the vortex generators have been studied and their influence on separation is reported. A main conclusion of the study is that the effect on separation can be related to the circulation induced by the vortex generators. The conclusions are finally summarised in chapter 6.

### 1.1. Truck aerodynamics

A heavy truck (for example the Scania R-series truck shown in figure 1.1), with warm low resistance tires, driven on a flat dry road at a speed  $U_x$  of 80 km/h has a rolling resistance which is approximately 50% of the total tractive resistance. The rest is aerodynamic drag. The rolling resistance coefficient  $f_r$  is known to be almost independent of the speed and therefore the drag from the tires increases linearly with speed ( $F_{x,tire} = f_r U_x$ ). Also the aerodynamic drag coefficient ( $C_D$ ) is fairly independent of the speed for a truck, which means that the aerodynamic drag ( $F_{x,aero} = \frac{1}{2} \rho C_D U_x^2$ ) increases quadratically with speed. At a speed above approximately 80 km/h the contribution of the aerodynamic to the total drag overshadows that of the tires as can be seen in figure 1.2.

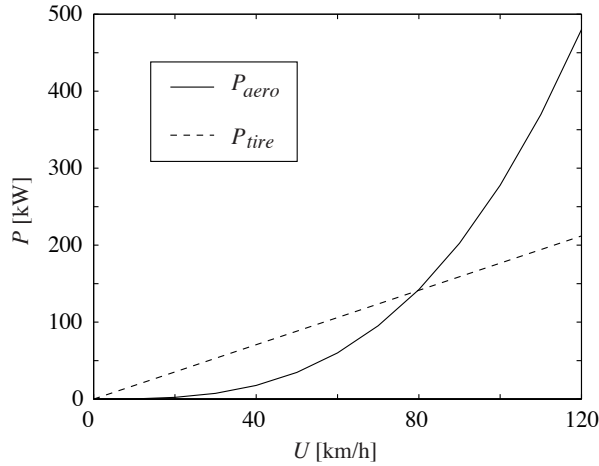


FIGURE 1.2. The engine power needed to overcome aerodynamic drag  $P_{aero}$  and tire rolling resistance  $P_{tire}$ . To produce this approximate plot the coefficients of wind averaged drag and rolling resistance were assumed to be  $C_{D,wa} = 0.6$  and  $f_r = 0.0045$ .

The analysis above is however slightly oversimplified since very few long haulage routes in the real world are completely flat, and vehicles usually also occasionally have to slow down or even stop. Therefore it is necessary to take into account both "hill climbing" and acceleration. According to detailed simulations performed at Scania (personal communication) a "rule of thumb" that is valid at moderately hilly long haulage routes (like Stockholm-Helsingborg) is that the aerodynamic drag constitutes around 30% of the total drag. This is for a truck trailer combination with a relatively smooth-sided trailer, low resistance tires and a modern twelve litre engine.

Since a truck manufacturer does not develop tires and cannot change the topography (although most companies work on systems to store brake energy) or do much about the traffic situation, aerodynamic drag is the one component of the tractive resistance that is possible to reduce. Apart from the environmental benefits of bringing down the fuel consumption the economical gains are substantial. Figure 1.3 demonstrates the relation between aerodynamic drag, fuel consumption and the annual cost of fuel for a long haulage operator. The truck in figure 1.4 was developed in 1999 as a technology demonstrator and one of the main features was the low  $C_{D,wa}$ <sup>1</sup>. In figure 1.3 this concept vehicle

<sup>1</sup>Since  $C_D$  increases with yaw for a normal truck a wind averaged drag coefficient  $C_{D,wa}$  is calculated by averaging the drag measured at different yaw angles. The measured  $C_D$  values are weighted to reflect the average wind speed at a certain distance from the ground.

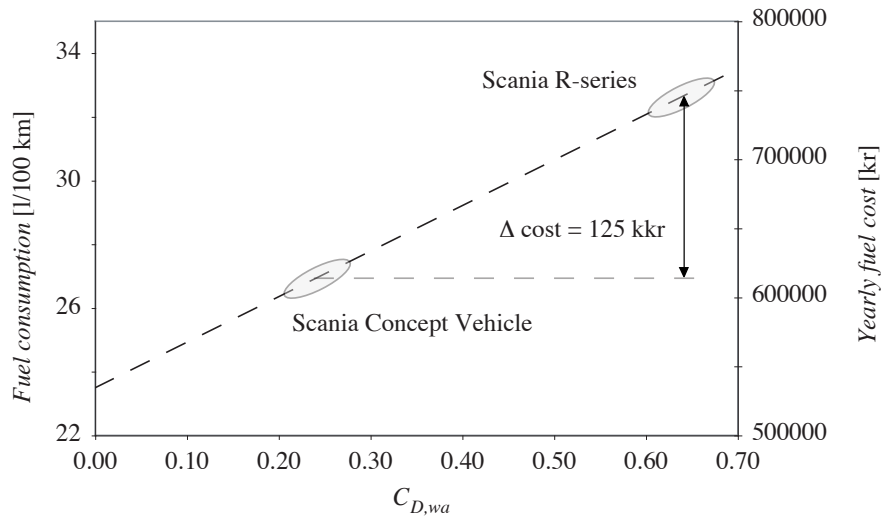


FIGURE 1.3. Fuel consumption and fuel cost for a truck used in long haulage operation. The fuel cost is based on an annual mileage of 200000 km and the price of diesel oil in May 2006 (11.41 kr/l). This is a slight overestimation since all large transport companies get great discounts on fuel.

is chosen to represent the realistic limit for aerodynamic drag reduction. The Scania R-series in the figure is typical for an aerodynamically well-designed truck of today and the span of  $C_{D,wa}$  given is to show how great the variation due to trailer choice can be.

A truck can be viewed as a bluff body and about 80% of the drag is pressure drag, which means that friction is less important. In the beginning trucks were shaped like bricks and there was massive separation all around the front. During the 70s and 80s the front of the trucks went from sharp cornered to rounded and air deflectors were fitted to the roof and the sides to smooth the transition from the cab to the body. This is illustrated as the change from a) to b) in figure 1.5. When the front radii are greater than 300 mm and the air deflector kit is properly designed there are not any major improvements to be made on the front. However, there are still many areas to improve on the sides, around the wheels and on the underbody, but in order to drastically reduce aerodynamic drag the separation at the end needs to be addressed.

The conventional - and very effective - way to reduce the wake is by tapering the rear end. Aerodynamically the best thing would be a full boat tail, like on an airplane, but this would result in a very long and not very driveable vehicle. Fortunately the marginal benefit decrease with length and a cut off

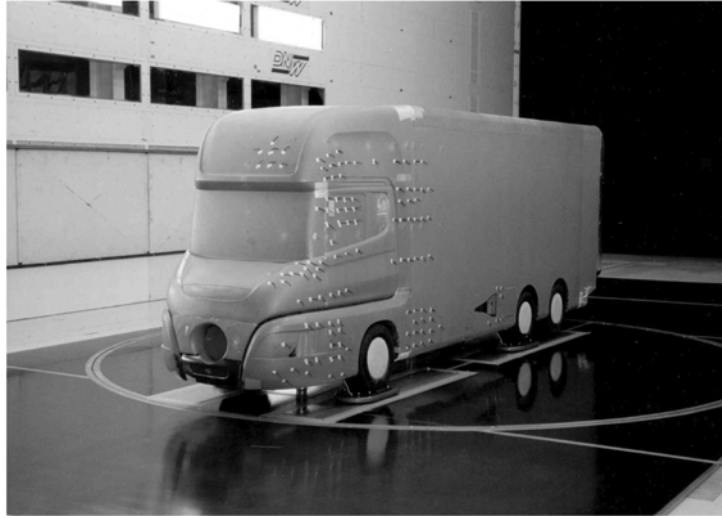


FIGURE 1.4. A Scania low drag concept truck from 1998. The shown configuration is without the accompanying trailer.

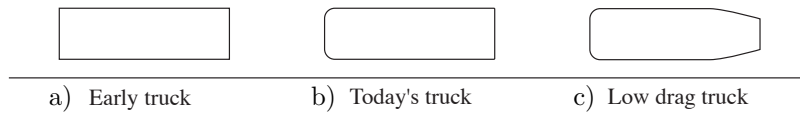


FIGURE 1.5. The aerodynamic development of trucks since the 1970s.

boat tail (so called Kamm back) like in figure 1.5 c) or figure 1.6 gives much of the benefit of a full boat tail without sacrificing the possibility to actually use the truck on the road. In figure 1.6 a boat tail tested by Scania can be seen. This particular device reduced  $C_D$  about 0.10.

Unfortunately, even an elongation of only 1 m is very difficult to apply on a european long-haulage truck. This is because of the rigorous legislation on vehicle length in the European Union. Since most of the cargo is box shaped and geometrically adapted to the internal width of a trailer<sup>2</sup> the tapered part must be an add-on device or at least not a part of the effective cargo volume. Thus a 1 m boat tail will lead to a loss of about 7% of the cargo space in a

<sup>2</sup>A Euro pallet is 1200×800 mm and the internal width of a trailer is approximately 2450 mm



FIGURE 1.6. A 1 m long boat tail attached to the back end of the 1998 Scania concept truck. The tapering angle is  $15^\circ$  and the flow is kept attached until the cut off of the boat tail.

standard 13.6 m trailer. To compensate for this,  $C_D$  must be reduced to a value close to zero, when fuel, the driver's salary and the capital cost of the vehicle are taken into account.

To make a boat tail work within the current legislation the angle must be much larger. Hence the air must be made to withstand a steeper pressure gradient without separation. In 2001 the author performed a wind tunnel test with a short boat tail with slot blowing. The device was mounted on the 1:2 scale model shown in figure 1.4. With the blowing turned on the maximum non-separating tapering angle increased from  $15^\circ$  to  $25^\circ$ . Even though the concept was implemented in a very crude way the principle was shown to work. However, the energy consumption of the fans needed to supply air to the blowing slot was so high that it neutralised the gains from the drag reduction and the space needed for the fans, valves and tubing not only reduces the cargo volume but impede access. Therefore it would be desirable to find another technical solution for the separation control; one that would have a similar effect but would be easier to implement. Such a possible solution would be to use vortex generators which, as already mentioned, are the topic of the present thesis.

## 1.2. Objectives

The objective of the work presented in this thesis is to increase the knowledge on separation control in turbulent boundary layers. This work is an extension of previous work of Angele (2003) where we now use three different pressure gradients, one similar to the one used by Angele and two which are more severe and which produce larger separations. This also means that separation control becomes more difficult in these two latter cases.

The objectives can be subdivided into a number of questions to be answered:

- How does the relative size of the vortex generator influence the vortex strength?
- How do the vortices move and develop in the boundary layer?
- How does yawing of the vortex generators influence their effectiveness?
- How to modify the existing APG experimental set-up to produce a larger separation bubble?
- How does the circulation required to stop separation change with bubble size, *i.e.* with pressure gradient?
- How important is the streamwise position, relative to the point of separation, where the circulation is produced?

## CHAPTER 2

# Turbulent boundary layers, separation and separation control

This chapter introduces several concepts and definitions that will be used when presenting the results in later chapters. It is not intended as a review of the literature on turbulent boundary layers nor separation, several recent extensive reviews of these areas are at hand and will be referenced below. However, with regard to separation control, and especially the use of vortex generators we intend to review previous work in more detail.

### 2.1. Some basic concepts

We start by stating the time averaged boundary layer equations for steady two-dimensional flow over a flat surface, namely the continuity equation

$$\frac{\partial U}{\partial x} + \frac{\partial V}{\partial y} = 0 \quad (2.1)$$

the  $x$ -momentum equation

$$U \frac{\partial U}{\partial x} + V \frac{\partial U}{\partial y} = -\frac{1}{\rho} \frac{\partial P}{\partial x} + \frac{\partial}{\partial y} \left[ \nu \frac{\partial U}{\partial y} - \overline{uv} \right] \quad (2.2)$$

and finally the  $y$ -momentum equation

$$\frac{\partial P}{\partial y} = 0 \quad (2.3)$$

Here  $x$  and  $y$  are the coordinates in the streamwise direction and the direction normal to the plate, respectively, whereas  $U$  and  $V$  are the mean velocity components in these directions, and  $u$  and  $v$  the corresponding fluctuating components. Overbar denotes time-averaging. The spanwise direction is  $z$  and the corresponding mean and fluctuating velocity components are  $W$  ( $W = 0$  in the two-dimensional case) and  $w$ . Since the pressure is constant across the boundary layer we can write

$$\frac{\partial P}{\partial x} = \frac{dP}{dx} \quad (2.4)$$

We can also write the pressure gradient in terms of the external mean flow velocity  $U_e$ , i.e. the undisturbed velocity outside the boundary layer, and according to the Bernoulli equation we obtain

$$\frac{1}{\rho} \frac{dP}{dx} = -U_e \frac{dU_e}{dx} \quad (2.5)$$

The boundary conditions to this system of equations are

$$y = 0 : U = 0, V = 0, u = 0, v = 0$$

$$y \rightarrow \infty : U \rightarrow U_e,$$

By integrating the  $x$ -momentum equation between the wall and the boundary layer edge (i.e.  $y = \delta$ , where  $\delta$  is the boundary layer thickness) it is possible to obtain the following relation

$$\frac{1}{2} c_f = \frac{d\delta_2}{dx} + \frac{1}{U_e} \frac{dU_e}{dx} (\delta_1 + 2\delta_2) \quad (2.6)$$

The skin friction coefficient is defined as

$$c_f = \frac{\tau_w}{\frac{1}{2} \rho U_e^2} \quad (2.7)$$

where

$$\tau_w = \left( \mu \frac{dU}{dy} \right)_{y=0} \quad (2.8)$$

$\tau_w$  is the time averaged wall shear stress and  $\mu$  ( $= \rho\nu$ ) is the dynamic viscosity. The quantities  $\delta_1$  and  $\delta_2$  are two integral boundary layer parameters, the displacement thickness

$$\delta_1 = \int_0^\delta \left( 1 - \frac{U}{U_e} \right) dy \quad (2.9)$$

and the momentum loss thickness

$$\delta_2 = \int_0^\delta \frac{U}{U_e} \left( 1 - \frac{U}{U_e} \right) dy \quad (2.10)$$

The shape factor is the ratio of the two integral boundary layer parameters

$$H_{12} = \frac{\delta_1}{\delta_2} \quad (2.11)$$

The vortical structures in cross-flow planes is often quantified by the stream-wise vorticity

$$\omega_x = \frac{\partial w}{\partial y} - \frac{\partial v}{\partial z} \quad (2.12)$$

and by the circulation around a contour  $C$ , that encloses a vortex

$$\Gamma = \int_C \mathbf{u} \cdot d\mathbf{x} \quad (2.13)$$

Stoke's theorem gives

$$\int_C \mathbf{u} \cdot d\mathbf{x} = \int_A (\nabla \times \mathbf{u}) \cdot \mathbf{n} dA \quad (2.14)$$

In the cross-flow plane, this reduces to

$$\Gamma = \int_C v dy + w dz = \int_A \left( \frac{\partial w}{\partial y} - \frac{\partial v}{\partial z} \right) dy dz \quad (2.15)$$

Thus the circulation around a contour can be obtained by integrating the streamwise vorticity of the area inside the contour

$$\Gamma = \int_A \omega_x dy dz \quad (2.16)$$

Another cross-flow parameter is the streamwise component of the swirling strength

$$Q_x = \frac{\partial w}{\partial y} \frac{\partial v}{\partial z} \quad (2.17)$$

The swirling strength is the second invariant of the velocity gradient tensor. It is a useful parameter, since there is no contribution from pure shear and it only coincides with the vorticity in roughly circular eddies. Thus the swirling motion become more obvious.

## 2.2. Turbulent boundary layers

### 2.2.1. Zero pressure gradient

The turbulent boundary at Zero Pressure Gradient (ZPG) and at Adverse Pressure Gradient (APG) are still in the centre of the debate in fluid dynamics, among other things there is still controversy regarding the scaling of the mean flow and the Reynolds stresses. This is despite the fact that several high quality experiments and high Reynolds number simulations have been made available over the last decade. However, recently an excellent review of the underlying theory and description of the present understanding is given in Panton (2005), mainly for ZPG turbulent boundary layers. It clearly shows that the traditional scalings, *i.e.* inner and outer can be seen as composite expansions, naturally giving rise to the logarithmic mean velocity region in between. It also shows

how the traditional scalings can be modified by taking higher order terms into account.

For instance Panton (2005) shows that an intermediate region exists with a logarithmic velocity distribution which could be expressed as

$$U^+ = \frac{1}{\kappa} \ln y^+ + B \quad (2.18)$$

where superscript + means scaling with wall variables,

$$U^+ = \frac{U}{u_\tau}, y^+ = \frac{yu_\tau}{\nu} \quad \text{and} \quad u_\tau = \sqrt{\frac{\tau_w}{\rho}} \quad (2.19)$$

where  $u_\tau$  is a wall velocity scale, which is usually called the friction velocity. The logarithmic distribution is valid from  $y^+ \approx 50$  to  $y/\delta \approx 0.15$ . Although most researchers agree that the logarithmic form of the mean velocity profile is appropriate there have been conflicting views on the value of the so called von Karman constant ( $\kappa$ ). From a thorough review of available data Panton (2005) suggested that  $\kappa$  should be close to 0.38.

### 2.2.2. Adverse pressure gradient

A newly published paper by Maciel (2006) is devoted to the scaling of the APG boundary layer upstream of the detachment point. It also contains a short review on earlier experimental studies of APGs and the reader is referred to that paper for further information. As pointed out by Maciel (2006) the wall velocity scale,  $u_\tau$  is inappropriate close to the point of separation since  $u_\tau \rightarrow 0$  there. Instead he advocates the use of the so called Zagarola-Smits velocity scale (Zagarola (1998)) which is defined as

$$U_{ZS} = U_e \frac{\delta_1}{\delta} \quad (2.20)$$

and the boundary layer thickness as the outer length scale. The paper shows excellent agreement for the outer layer mean velocity distribution, but it also scales the Reynolds stresses. Panton (2005) points out that wall scaling actually is proportional to the the Zagarola-Smits velocity scale for high Reynolds numbers.

## 2.3. Separation

Separation of boundary layers occurs either due to a strong adverse pressure gradient (pressure induced separation) or is due to drastic change in the geometry of the surface (geometry induced separation). Typical examples of the latter is obtained where there is a sharp edge or strong curvature such as for a backward facing step, bluff bodies (typical truck geometries etc). For strong

adverse pressure gradient flows along flat or mildly curved surfaces the occurrence of separation does however not only depend on the local pressure gradient but also on the local boundary layer state.

The separation point (or maybe more accurately the separation line) and the so called "separated region" or "separation bubble" are not well defined quantities in a turbulent boundary layer. The separation point (sometimes called the detachment point) is usually defined as the point where  $\tau_w = 0$ . However this means that part of the time the fluctuating wall shear stress is positive and part of the time negative. Another definition of the separation point uses the backflow coefficient ( $\chi$ ), *i.e.* the fraction of time the flow is in the backward direction. The separation point is then defined as the point where on the average the flow is directed backwards 50% and forwards 50% of the time, *i.e.*  $\chi = 0.5$ . This position does only correspond to the position where  $\tau_w = 0$  in case the probability density distribution of the fluctuating wall shear stress is symmetric around zero.

The reattachment point, *i.e.* the position where the boundary layer reattaches to the surface (if it does), can be defined in a similar way as for the separation point.

Simpson (1989) has proposed a classification of the stages of the turbulent boundary layer separation process. It is based on the backflow coefficient:

- Incipient Detachment (ID):  $\chi = 0.01$ .
- Intermittent Transitory Detachment (ITD):  $\chi = 0.2$ .
- Transitory Detachment (TD):  $\chi = 0.5$ .
- Detachment (D):  $\tau_w = 0$ .

The separated region can be defined as the region where the flow is recirculating in a time averaged sense. The demarcation line is hence called the dividing or separation streamline. Other definitions of the demarcation line is the contour line where the streamwise velocity is equal to zero or the contour line on which  $\chi = 0.5$ . The two latter definitions usually give regions of similar size whereas the dividing streamline definition naturally gives a larger separated region.

Many reviews, papers and thesis have been written on separation and we mention only a few here for further reference. Simpson (1989) reviews the field up to 1989 and also references his own extensive research. Later work was done by Fernholz and co-workers on an axisymmetric body and Kalter & Fernholz (2001) also contain an up-to-date review of the literature. Also worth mentioning are the thesis presented within KTH Mechanics on separation related issues, experiments by Häggmark (2000) and Angele (2003) on laminar and turbulent boundary layer separation, respectively, the experiments by Törnblom (2006) on diffuser flow separation and the DNS studies by Skote & Henningson (2002) on boundary layer flow separation.

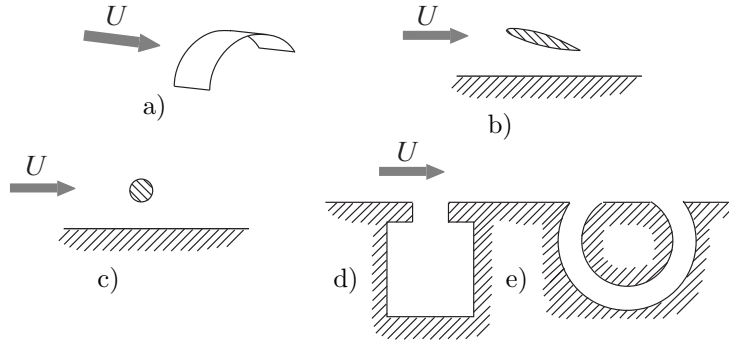


FIGURE 2.1. Different control devices: a) elongated arches, b) large-eddy breakup device, c) spanwise cylinder, d) Helmholtz resonator and e) fluidic flapper.

## 2.4. Separation control

Control of separation of boundary layer flows can be achieved through different approaches. A well known example is the golf ball, where the dimples on the surface promotes transition from a laminar to a turbulent boundary layer, which makes the separation line move backwards on the ball, thereby reducing the pressure drag substantially. For turbulent boundary layers suction at the wall, tangential blowing, vortex generators of different kinds are possible methods. In the following we intend a thorough review on the available literature regarding vortex generators. Note that if nothing else is written the reviewed experiments are performed at zero pressure gradient.

### 2.4.1. Comparisons of different separation control devices

There are many reviews of flow control techniques and there are also some comparison experiments reported. For extensive reviews on flow control see for example the book written by Gad-el Hak (2000) or the earlier article by Gad-el Hak & Bushnell (1991)

The performance of several arrays of passive and active devices for controlling a separated region on a backward-facing ramp was investigated in Lin, Howard & Bushnell (1990). Of the tested methods vortex generators, vortex generator jets, elongated arches and large-eddy breakup devices (LEBU) all reduces separation. Spanwise cylinders, Helmholtz resonators and fluidic flappers were less successful. Except for vortex generators and vortex generating jets, that are described in detail later, the different control devices are shown

in figure 2.1. The experimenters claim that the vortex generators should be placed three to ten blade heights upstream of the separation line. Another study in the same test section by Lin, Howard & Selby (1989) only addresses passive devices. Vortex generators submerged in the boundary layer give the best compromise between effectiveness in reducing separation and device-drag according to the authors.

Stanislas & Godard (2005) made a comparison of passive vane-type vortex generators and active jets in an adverse pressure gradient mimicking the suction side of an airfoil. Both actuator types were configured in co-rotating and counter-rotating arrays. The flow field in the area downstream of the devices were shown to be fairly similar for the active and passive counter-rotating cases, but for the co-rotating configuration the jet is much more effective than the vane.

#### 2.4.2. *Passive vortex generators*

The first experiments on conventional vane-type passive vortex generators were reported by Taylor (1947). This type of vortex generator normally consists of a row of blades or airfoils, slightly higher than the boundary layer thickness, set at an angle against the on-coming flow.

Schubauer & Spangenberg (1960) tried a variety of fixed mixing devices at different adverse pressure gradients. They concluded that the effect of mixing is equivalent to a decrease in pressure gradient. One year later Pearcy (1961) published an early design guide. In this article inviscid theory was applied to predict the cross-plane movements of vortex centers as the vortices are convected downstream. Both co-rotating and counter-rotating vortices are studied (see figure 2.2 for definitions) According to him the vortices in a counter-rotating pair with a common downflow, that is arranged in a larger array, will first move away from each other and towards the wall. As the vortex is getting closer to one of the vortices of the neighboring vortex pair it starts to rise and after a while stops its spanwise movement and forms a new counter-rotating pair with common upflow. The new pairs will continue moving away from the wall. When the vortices move apart a thin diverging boundary layer is formed in

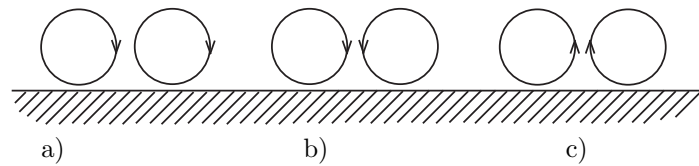


FIGURE 2.2. Different types of vortex pairs: a) co-rotating, b) counter-rotating with common downflow and c) counter-rotating with common upflow.

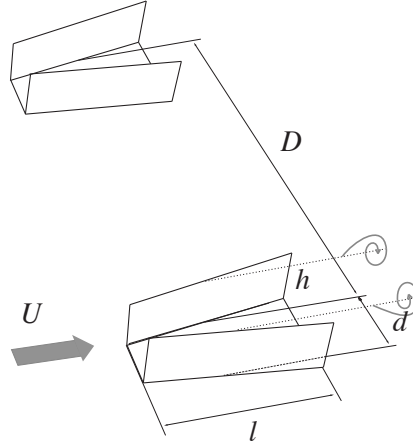


FIGURE 2.3. Schematic showing the main dimensions of a VG array.

between them. It is also reported that counter-rotating VG arrays can be as efficient as co-rotating arrays in preventing separation when the blade spacing is greater than three times their height. According to Pearcy the optimum ratio of the spanwise spacing of the VG pairs  $D$  and the spanwise blade spacing within the pair  $d$  is  $D/d \approx 4$  (see figure 2.3). He also claims that  $D$  should be approximately ten times the blade height  $h$ .

The evolution of a single vortex embedded in a turbulent boundary layer was thoroughly investigated by Shabaka, Mehta & Bradshaw (1985). To reduce the axial velocity variation the vortex was generated on the floor of the settling chamber. The experimental results show some evidence that close to the wall the vortex induces vorticity, which has opposite sign compared to the primary vortex. This induced vorticity was observed to be convected to the up-wash side of the vortex. It is also claimed that since turbulence diffuses both the boundary layer and the vortices their ratio stay constant when moving downstream over the plate. The lateral "snaking" of the vortex was shown to be small. In a continuation of this study Mehta & Bradshaw (1988) describes experiments with a counter-rotating vortex pair in same basic set-up. The vortices have a common upflow from the surface and although entering the test section embedded in the boundary layer, at some distance downstream, the distance from the wall of the vortex centers is about twice the boundary layer thickness. Boundary layer fluid is lifted by the vortices and entrained into them. Compared to the single vortex case the circulation from each vortex is about 20% stronger. This is probably due to the impermeable constraint imposed as vortices act as mirror images of each other, and hence increase the

circulation (lift) by "ground-effect". Throughout the test section there is very little direct interaction between the vortices. Just as in the single vortex case the lateral wandering is small. Vortices generated by wishbone type vortex generators were surveyed by Wendt & Hingst (1994). They also form counter-rotating pairs with common upflow and show the same strong tendency to rise up through the boundary layer.

Experiments by Cutler & Bradshaw (1993*a,b*) examine the case of a strong ( $\Gamma/(U_\infty/\delta) > 10$ ) counter-rotating vortex pair; first above the boundary layer and then embedded in it. In the case where the vortices are introduced above the boundary layer, the vortex pair is moving down towards the wall, but the vortex never enters the boundary layer and the effect of the interaction with the boundary layer on the vortices are reported to be small. Below and between the vortices the boundary layer is thinned by lateral divergence and it almost stops growing. The divergence causes  $c_f$  to increase approximately 10% along the centreline. On the sides of the vortex pair lateral convergence causes reduced skin friction. In case of the low vortex pair separation lines<sup>1</sup> are formed on the outboard of the vortices. The lines are present along most of the test plate length. Above the lines, regions of low momentum fluid of opposite sign vorticity are formed. As the two vortices entrain the fluid of opposite sign vorticity they are weakened.

Another important study of a single vortex in a boundary layer was performed by Westphal, Pauley & Eaton (1987). The vortex was produced by a delta wing that was somewhat higher than the boundary layer thickness. They examined the vortex core area growth and showed that when the core radius reaches a certain fraction of the height of the vortex centre to the wall, the vorticity contours become elliptic in shape. This was thought to be a symptom of meandering, but no evidence of any lateral movement of the vortices was found. The overall circulation when the vortex evolved downstream was decreasing slowly or remained almost constant for different cases. This study established today's normal practices on how to define the vortex centre, the circulation and the core area. One configuration was tested in an adverse pressure gradient. The results are reported both in Westphal *et al.* (1987) and Westphal, Eaton & Pauley (1985) and show an increased vorticity diffusion and hence a more rapid vortex centre growth. The onset of vorticity contour flattening was accelerated by the pressure gradient. To investigate more thoroughly whether the ellipticity was caused by vortex meandering an experiment with a laterally oscillating vortex generator was carried out by Westphal & Mehta (1989). The results indicate that the unforced vortex is laterally stable and also show that the initial meandering caused by the moving VG is damped as the vortex is convected downstream.

---

<sup>1</sup>Discontinuities onto which the surrounding wall streamlines converge. They are caused by the interaction between the vortex up-wash and the boundary layer.

Pauley & Eaton (1988) examined the streamwise development of pairs and arrays of longitudinal vortices embedded in a turbulent boundary layer in a zero pressure gradient. This study varies vortex generator blade spacing and blade angle and examines the difference between counter-rotating vortices with common upflow and downflow and co-rotating vortices. All configurations use blade heights well above the boundary layer thickness. The authors claim that the interaction of the secondary flow and the no-slip condition produce negative vorticity below the vortex. This vorticity is swept up on the side of the primary vortex to create a small region of opposite vorticity. A rollup into a secondary vortex is never observed. The vortex centre movements in the cross-plane are as expected from inviscid theory, although the paths are slightly modified by secondary flow structures. The proximity of other vortices does not affect circulation decay, but increases the vorticity diffusion. The rate of circulation decay is governed by the proximity to the wall.

In most experiments the first measurements are taken at more than 10 blade heights downstream of the vortex generators. To study the initial circulation and peak vorticity Wendt (2001) started to measure just one chord length ( $0.4 < c/h < 4$ ) downstream of the blade trailing edge of an array of vortex generators. Several counter- and co-rotating configurations are investigated and the aspect-ratio, the blade length and the blade angle are varied. The vortex strength was observed to be proportional to the free stream velocity, the blade angle and the ratio between blade height and boundary layer thickness. With these three parameters held constant an increasing aspect-ratio reduces circulation. In the study counter-rotating vortices show greater circulation magnitude than a single vortex produced by the same blade parameters. For co-rotating vortices the produced circulation is lower than for the single vortex. The circulation is shown to be accurately modeled by an equation based on Prandtl's relation between circulation and airfoil geometry. Wendt *et al.* (1995) earlier studied the decay of counter-rotating vortices in approximately the same set-up. The vortices have their common flow directed upwards and their distance to the wall increases as they evolve downstream. Thus the wall friction decreases and the decay is probably less than for vortices with common downflow. The circulation decay is almost linear until  $x/h = 70$ .

In order to reduce the drag penalty caused by the vortex generators work is done to reduce their size, hopefully without sacrificing mixing. The comprehensive review on low-profile vortex generators by Lin (2002) show that small ( $h/\delta \sim 0.2$ ) vortex generators are just as effective in preventing separation as the normal ( $h/\delta \sim 1$ ) sized devices. According to the review low-profile VGs should be applied when the detachment point is relatively fixed and the VGs can be positioned close to the separated region. One of the studies that were reviewed is the one by Yao, Lin & Allan (2002) where stereoscopic PIV is utilised to compare a low-profile vortex generator ( $h/\delta = 0.2$ ) with a conventional one. Here the maximum vorticity generated increases as the angle of

attack increases for the small VG, but it decreases with angle of attack for the large VG due to stall. Apart from that there are no fundamental differences between the two VGs. Both sizes of vortices decay in an almost linear way, but at a higher rate down to  $x/h = 30$  and then slower. The size of the vortex centre area also evolves linearly.

Godard & Stanislas (2006) recently published an optimisation study on co- and counter rotating submerged vortex generators. They conclude that triangular blades are better than rectangular blades, both in terms of increased vortex strength and in reduced drag. They also found that the counter-rotating set-up was twice as effective as the co-rotating in increasing the wall shear stress and that the optimum angle of attack is about  $18^\circ$ .

The unsteady interaction between a pair of longitudinal vortices and a boundary layer was studied by Angele & Grewe (2002). They claim that there is a time-dependent vortex stretching, which as a result gives an inverse correlation between vortex size and the maximum vorticity. Later on Angele & Muhammad-Klingmann (2005a) investigated the effect of longitudinal vortices on the mean flow and the turbulence structure of a separating boundary layer. The counter-rotating and initially non-equidistant vortices evolve toward an equidistant state within the boundary layer as the swirling velocity component decreases and the boundary layer becomes two-dimensional. Lögdberg & Alfredsson (2005) and Lögdberg (2006) continued these experiments for larger pressure gradients.

#### 2.4.3. Active vortex generators

Flow control by vortex generator jets (VGJ) was first described by Wallis (1952). He claimed that an array of VGJs is as effective as passive vortex generators in suppressing separation on an airfoil. The advantage of an active system is that it can be turned off when it is not needed and thus the parasitic drag of conventional vortex generators can be avoided. In the following text the yaw and pitch angle is used to define the jet direction. The pitch angle is the angle between the wall and the jet centreline. Yaw is the angle between the wall projection of the jet centreline and the free stream direction. The definitions are also found in figure 2.4. Note that in some articles the yaw angle is referred to as skew angle.

After some more experiments by Wallis very little was published until the 1990s. The study by Johnston & Nishi (1990) demonstrated how streamwise vortices are produced by an array of pitched jets at  $90^\circ$  yaw (*i.e.* the jets are perpendicular to the main flow direction). A pitch angle of less than  $90^\circ$  was needed in order to generate vortices effectively. Some success in reducing the size of a separated region in APG was also demonstrated when the ratio of jet speed to free stream velocity (VR) was 0.8 or higher.

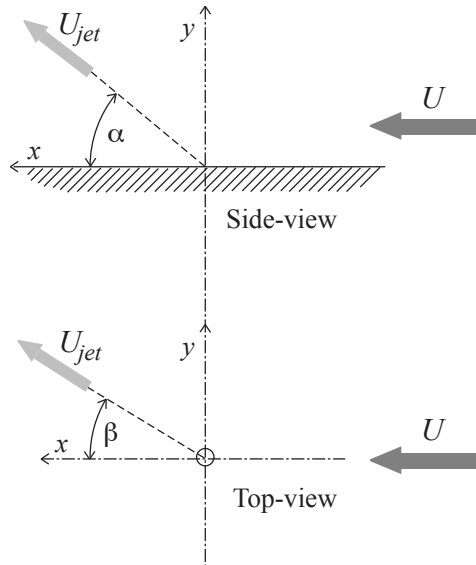


FIGURE 2.4. Schematic showing how the jet direction is defined. The angle  $\beta$  is yaw and the angle  $\alpha$  is pitch.

Compton & Johnston (1992) studied VGJs pitched at  $45^\circ$  and yawed from  $0$ - $180^\circ$  from the mean flow (a  $180^\circ$  yaw angle means that the jet is directed in the upstream direction). A yaw between  $45$  and  $90^\circ$  was found to give the strongest vortices. Circulation was also found to increase monotonically as the VR was increased up to  $1.3$ . In a comparison to delta-shaped VGs the vortices from the jets decayed more rapidly.

In an experiment on a zero pressure gradient flow followed by a backward facing  $25^\circ$  ramp Selby, Lin & Howard (1992) measured the increase in pressure recovery of different VGJ array configurations. The pressure recovery increased monotonically up to the highest tested VR ratio of  $6.8$ . It was shown that a small pitch angle ( $15^\circ$  or  $25^\circ$ ) is beneficial, since momentum transfer occurs closer to the wall. The optimum yaw angle appears to be between  $60^\circ$  and  $90^\circ$ . An interesting comparison with tangential slot blowing at an equal flow rate per unit width showed substantially better pressure recovery for the VGJ case.

According to the review by Johnston (1999) the VR is the dominant parameter in generating circulation. He also concludes that a pitch angle below  $30^\circ$  and a yaw angle in the range  $60^\circ$  to  $90^\circ$  from the free stream are the most effective. The exact streamwise location of the VGJ row seems less important since the boundary layer reacts likewise independent of where it is energised. The VGJ spacing, the hole diameter and the hole shape are yet to be optimised.

Khan & Johnston (2000) showed detailed measurements of the flow field downstream of one VGJ. Their data support earlier experiments when they claim that a yaw angle of  $60^\circ$  produces the highest peak vorticity. For pitch they write that  $30^\circ$  is the optimum angle, but the only other angle that is tested is  $45^\circ$ . The flow field seems similar to that of solid VGs.

Zhang (2000) showed that a rectangular jet can produce higher levels of vorticity and circulation compared to a circular jet of equal hydraulic diameter and VR. The circulation decay is linear for both nozzle configurations. The complicated near field structures around a rectangular skewed jet was earlier investigated by Zhang, Zhang & Hurst (1996). Another experiment on the jet hole design by Johnston, Moiser & Khan (2002) showed that the inlet geometry affects the near-field but not the far-field.

For a fixed direction single VGJ the VR was varied in an experiment by Rixon & Johari (2003). The jet creates a pair of vortices of which one is significantly stronger. The weak vortex was found to decay rapidly and only the strong one persisted downstream. Both circulation and the vortex centre distance to the wall increased linearly with VR for ratios between one and three. Somewhat surprisingly the vortex core was observed to meander up to  $0.3\delta$  in both the wall normal and spanwise directions.

Zhang (2003) studied co-rotating vortices produced by a spanwise array of VGJs where both yaw and pitch are set to  $45^\circ$ , and described the complicated near field. The ratio of vortex strength of the primary and secondary vortices (cf. Rixon & Johari (2003)) are shown to depend on VR. Compared to a single vortex the array of co-rotating vortices experience a larger spanwise movement as they evolve downstream, but after a certain distance opposing secondary flow structures seem to halt the spanwise motion.

In all previous reports the vortex strength have been reported to increase monotonically with VR, but Milanovic & Zaman (2004) finds a maximum in the region of  $VR = 2.0$ – $2.8$ . The optimum yaw angle and pitch angle are in accordance with earlier experiments.

## CHAPTER 3

### Experimental set up

In this chapter the two wind tunnels that are used in the present study are described. Thereafter the implementation of the measurement techniques are presented, *i.e.* single- and X-wire anemometry, particle image velocimetry (PIV) and smoke visualisation. Finally the vortex generator design is discussed.

#### 3.1. Wind tunnels

##### 3.1.1. MTL wind tunnel

The MTL<sup>1</sup> wind tunnel was used to investigate the flow field development downstream pairs and arrays of different vortex generators. The MTL wind tunnel (see figure 3.1) is designed to achieve very low free stream turbulence levels. The streamwise turbulence intensity near the test section centreline is less than 0.015%. The temperature variation in time is also very low, which makes this tunnel suitable for hot-wire measurements. In order to be able to control the streamwise velocity distribution the top and bottom walls are

<sup>1</sup>For "Minimum Turbulence Level" or "M.T. Landahl", former professor at KTH Mechanics

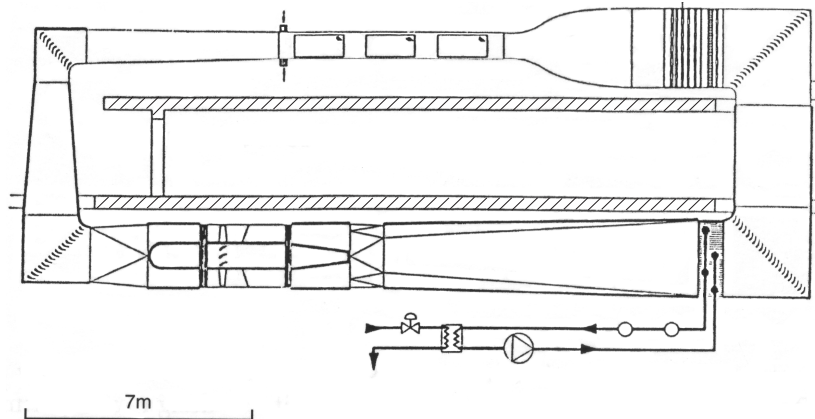


FIGURE 3.1. Schematic of the MTL wind tunnel at KTH



FIGURE 3.2. The test section seen from the contraction. In the ceiling the slot for the traversing system can be seen and in the center of the image the flat plate is resting on its two supporting beams.

adjustable. A detailed study of the flow quality in the wind tunnel was reported by Lindgren & Johansson (2002).

The test section is 7.0 m long and has a cross-sectional area of  $1.2 \times 0.8 \text{ m}^2$  (width  $\times$  height). A horizontal 5.8 m (except the trailing edge flap) long plate, which spans the whole width of the test section, was mounted with its upper surface 0.51 m from the ceiling. The plate can be seen in the test section in figure 3.2. The coordinate system is chosen so that  $x$  is positive downstream and  $x = 0$  at the leading edge of the plate,  $y$  is positive in the wall normal direction and  $y = 0$  at the surface and  $z$  is the spanwise component with its direction given by  $x$  and  $y$  and  $z = 0$  at the tunnel centreline. The boundary layer was tripped by means of eight rows of turbulator tape at the flat plate leading edge to ensure a fully turbulent boundary layer. The plate was waxed to make it smooth, but no measurements of the surface roughness were performed since this parameter was considered less important in this particular experiment.

The variation of the free stream velocity was measured by traversing a hot wire along the test section centreline at  $y = 120 \text{ mm}$ . The position of the test section ceiling was adjusted to give a velocity variation of less than 0.5%. In figure 3.3 the relative velocity variation in the downstream direction ( $x$ ) is shown.

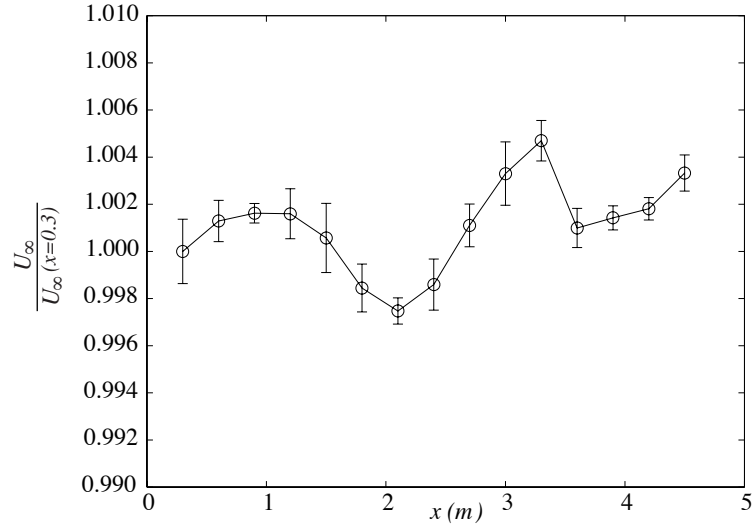


FIGURE 3.3. The relative streamwise variation of  $U_{\infty}$  along the test section centreline at  $U_{\infty} \approx 26.5$  m/s with error bars showing the standard deviation.

### 3.1.2. *BL wind tunnel*

The adverse pressure gradient experiments were all conducted in the BL<sup>2</sup> wind tunnel at KTH Mechanics (figure 3.4). The test section is 4.0 m long and has a cross-sectional area of  $0.75 \times 0.5$  m<sup>2</sup> (height  $\times$  width). For a detailed description of the wind tunnel the reader is referred to Lindgren & Johansson (2004). A schematic of the experimental setup is shown in figure 3.5. A vertical flat test plate made of Plexiglas, which spans the whole height and length of the test section, is mounted with its upper surface 300 mm from the back side wall of the test section. After 1.25 m the test section is diverged by using a flexible wall in order to decelerate the flow. Suction is applied on the flexible wall to prevent separation on the curved wall and induce an adverse pressure gradient (APG) on the test plate. In figure 3.6 a) the test plate and the curved ceiling can be seen. It is also possible to catch a glimpse of the suction tubing through the flexible wall. The tubing is connected to a radial fan shown in figure 3.6 b). The suction rate in this experiment was set to 6–7% of the flow over the flat plate at the inlet of the test section in APG case I. In case II the suction rate was 12.5–13% and in case III it was approximately 17%.

<sup>2</sup>For "Boundary Layer" or "Björn Lindgren", after the designer of the tunnel.

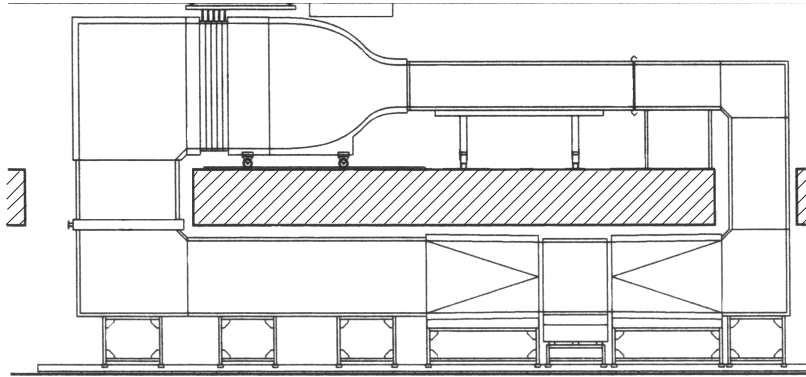


FIGURE 3.4. Schematic of the BL wind tunnel at KTH.

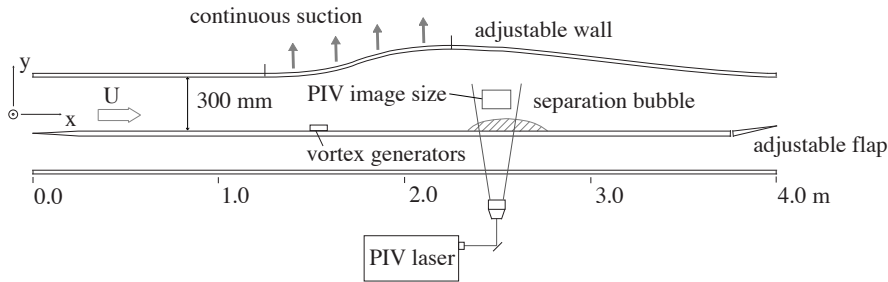


FIGURE 3.5. Schematic of the BL test section. The test section is seen from above in this figure.

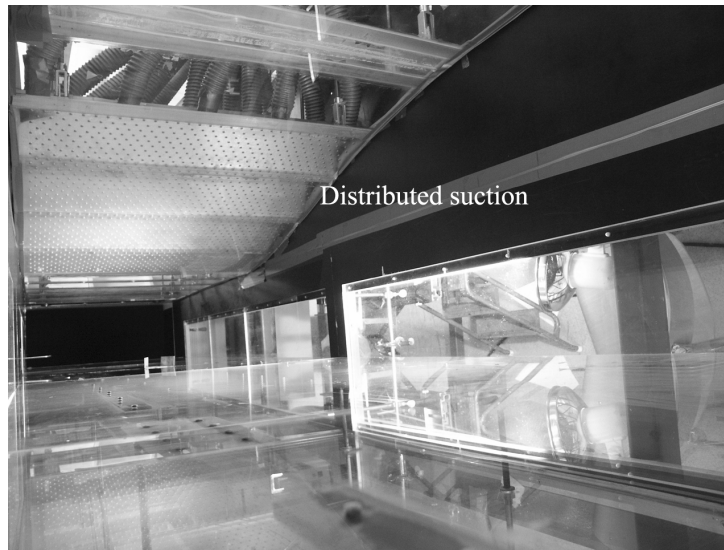
## 3.2. Measurement techniques

### 3.2.1. Hot-wire anemometry

All the velocity measurements in the MTL wind tunnel were performed using hot-wire probes operating at constant temperature.

The traversing system is shown to enter the test section from a slit in the ceiling in figures 3.2. With the probe holder in figure 3.7 the probe can be traversed from  $x \approx 200$  mm to  $x \approx 5300$  mm, from  $y = 0$  mm to  $y \approx 130$  mm and from  $z = -72.5$  mm to  $z = 72.5$  mm.

Since the flow is two-dimensional when there is no VGs on the test plate a single-wire probe could be used. When the vortex generators were mounted on the plate it was necessary to employ X-wire probes in order to be able to measure all three velocity components. Both the single-wire probe and the X-probes were made from  $5.0 \mu\text{m}$  platinum wire with about 1 mm between



a)



b)

FIGURE 3.6. Details of the BL wind tunnel test section. a) Inside of BL wind tunnel test section. The shape of the ceiling is adjustable and fitted with suction holes. A vortex generator pair is mounted on the test plate. Note that the photograph is rotated  $90^\circ$ . b) The BL wind tunnel suction system. The tubing is connected to the perforated wall of the test section. The suction rate is controlled by a bypass valve on the fan.

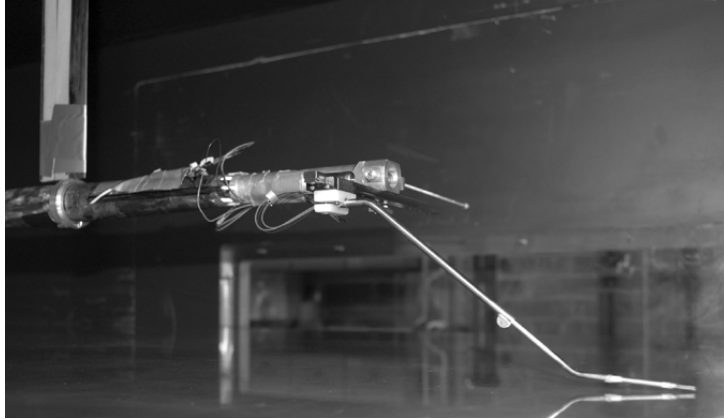


FIGURE 3.7. The traversing system is designed not to disturb the flow field around the probe.

the prongs. The hot-wire probes are calibrated in the wind tunnel, outside the boundary layer. A calibration function for a single wire probe, with a term added to King's law to compensate for natural convection, was used. The procedure is described in Johansson & Alfredsson (1982). In this case the extra term is less important because the velocities are quite large.

Normally the probe (shown in figure 3.8) is rotated  $90^\circ$  around its stream-wise axis to measure the  $U$  and  $V$  components and the  $U$  and  $W$  components respectively. In this case the traversing system did not allow probe rotation and therefore two probes had to be used: one oriented to measure the  $U$  and  $V$  velocity components and another oriented to measure the  $U$  and  $W$  velocity components. The calibration procedure for the X-probe was similar to the one described by Österlund (1999). The data points for the calibration were measured at eleven velocities from 7 to 28 m/s and at nine angles of attack from  $-40^\circ$  to  $+40^\circ$ . Then two two-dimensional fifth order polynomials were fitted to the data with the coefficients determined by a least-square method. Unlike the single-wire case and King's law this fit is not based on any physical relation. Therefore data points outside the calibrated region are not to be trusted. In figure 3.9 the data points (only every tenth in order to make the figure easier to interpret) for the VG case with the largest secondary velocities are plotted together with the instantaneous data points.

The wall distance of the single-wire probe was found by decreasing the wind speed to make the boundary layer laminar. Then an extrapolation of a linear fit to six velocity measurements close to the wall made it possible to accurately determine the position of the probe. The X-wire probe was photographed next to a precision manufactured 0.77 mm long cylinder and then the wall distance

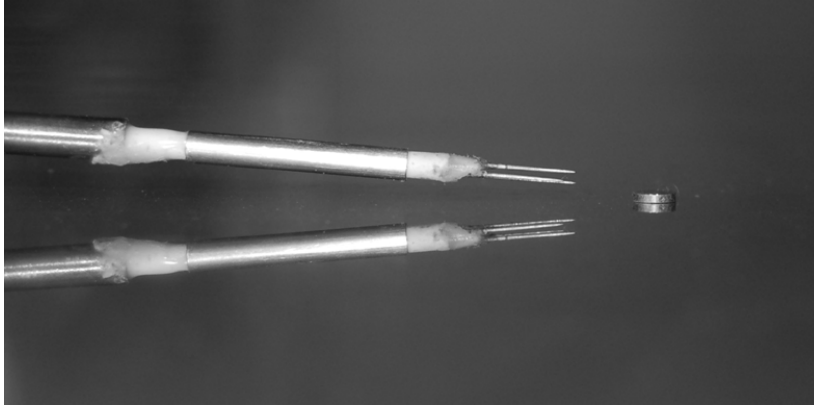


FIGURE 3.8. One of the cross-wire probes near the test plate. Next to the probe a 0.77 mm high cylinder can be seen. Note that the lower probe in the picture is a reflection in the test plate.

was determined by measuring the probe position relative to the top of the cylinder on the photograph.

Normally seven planes were measured downstream of each configuration. In each measurement plane there are 266 ( $19 \times 14$ ) or 322 ( $23 \times 14$ ) data points. The traversing and collection of data is automatic and takes approximately 14 hours for seven planes. Before every new 14 hours run the calibration was checked against the wind tunnel Prandtl tube. Usually a new calibration had to be performed after two seven plane runs.

The velocity data from an X-wire probe in a gradient perpendicular to the wires need to be corrected because the simplifying assumption of uniform velocity in the probe measurement volume is no longer valid. In this experiment the worst case is when the probe is oriented to measure the  $U$  and  $W$  velocity components in the boundary layer. Then the distance  $\Delta$  between the wires causes the normal velocity to the wires and hence the cooling velocities to differ considerably. Normally this does not produce any significant errors in the  $U$  component that is proportional to  $E_1 + E_2$  and thus a function of the mean cooling velocity in the measurement volume. The spanwise  $W$  component, on the other hand, is proportional to  $E_1 - E_2$ . This means that any velocity gradient in  $y$  will produce an erroneous measured velocity in  $W$ . In the experiments reported here the data is corrected using the procedure described by Cutler & Bradshaw (1991). Only  $V$ ,  $W$ ,  $\overline{u'v'}$  and  $\overline{u'w'}$  are corrected. In  $U$  the error is very small and the correction terms of the Reynolds normal stresses  $\overline{u'^2}$ ,  $\overline{v'^2}$  and  $\overline{w'^2}$  include terms not known from the measurements.

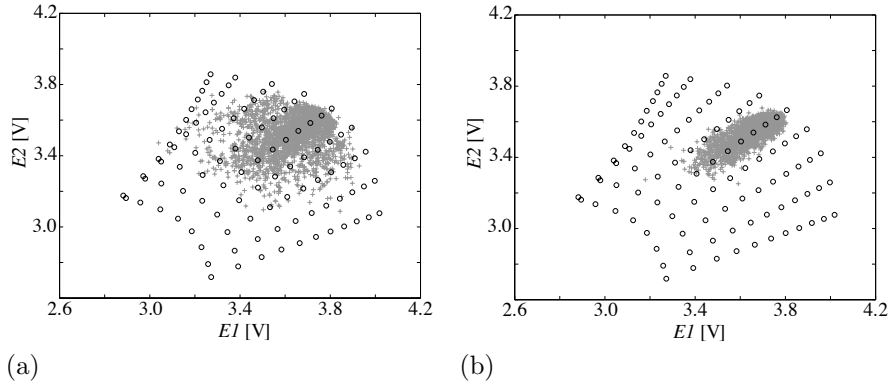


FIGURE 3.9. Hot wire calibration plot, superimposed on instantaneous measurement data taken at  $U_\infty = 26.5$  m/s. a) 0.06 m downstream of the VG ( $x_{VG} = 0.06$  m). b)  $x_{VG} = 2.67$  m. The case with 18 mm vortex generators is shown, since this is the "worst case", emph.i.e. with the largest secondary velocity components.

Errors due to high turbulence (Cutler & Bradshaw (1991)), blockage by the probe and displacement of the wires so that they do not cross at their mid-points (Talamelli, Westin & Alfredsson (2000)) are not corrected for.

### 3.2.2. PIV

The PIV-system used consists of a 400 mJ double cavity Nd:Yag laser operating at 15 Hz and a  $1018 \times 1008$  pixels CCD camera with 8 bit resolution. The air was seeded with smoke droplets generated by heating glycol and injected in the pressure equalizer slit downstream of the test section. The droplets are large enough to render a particle image size larger than 2 pixels in all measurements. According to Raffel, Willert & Kompenhans (1997) this is enough to avoid peak-locking due to problems with the peak-fit algorithm. The number of particles inside the interrogation areas (*ias*) is above the value of five, recommended by Keane & Adrian (1992), in all measured  $xy$ -planes and most of the  $xz$ -plane.

Conventional post-processing validation procedures were used. No particles moving more than 25% of the interrogation area length were allowed in order to reduce loss-of-pairs and the resulting zero-velocity bias. The peak height ratio between the highest and the second highest peak in the correlation plane must be more than 1.2 if the vector should be kept. Using these criteria on the data resulted in a validation rate of more than 95% for the  $xy$ -plane measurements at  $x = 2500$  mm (APG case II). At some  $x$ -positions the validation rate is

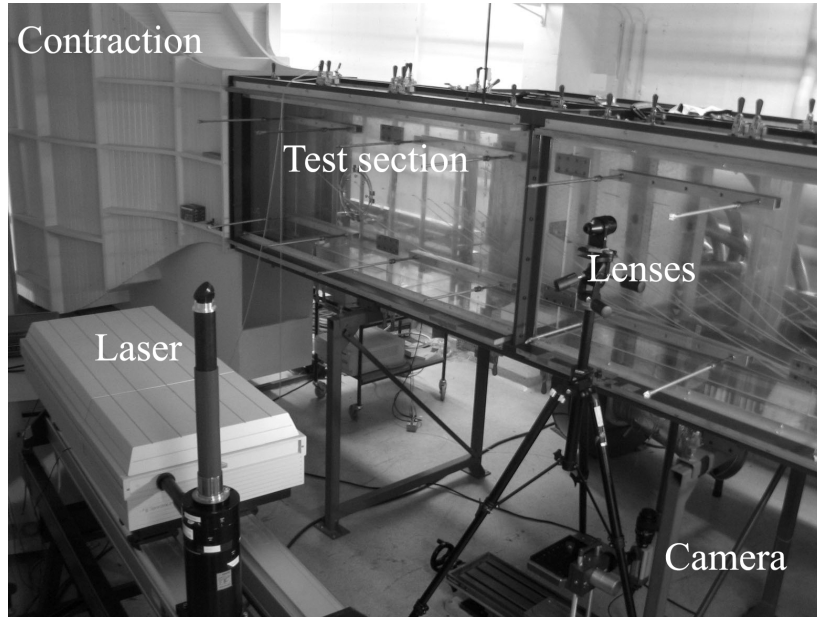


FIGURE 3.10. PIV set-up. After the first 2 m of the Plexiglas test section there is a steel beam that interrupt the measurements. This can be seen in some of the figures later on.

much lower due to bubbles in the Plexiglas that reduces the light intensity and makes the laser sheet streaky. But in those cases there are almost always high quality areas in the image that are large enough to produce a reliable  $U$ -profile.

When measuring APG case II the images are all approximately  $90 \times 90 \text{ mm}^2$ . Using  $32 \times 32$  pixels interrogation areas the spatial resolution is 2.8 mm. The time ( $t$ ) between the cross-correlated image pairs was 30–35  $\mu\text{s}$ . This makes the ratio between the discretization velocity  $u_d$  and the  $rms$  value of the streamwise velocity less than 2. According to Angele & Muhammad-Klingmann (2005b) this reduces errors due to peak-locking effects in mean and  $rms$  values to less than 1%. In order to be able to obtain velocity data for the full height of the boundary layer images were taken at two different positions in the wall normal direction at each  $x$ -station. To follow the uncontrolled boundary layer development measurements were made at eleven different  $x$ -stations. Typically 1024 or 2048 image pairs were taken at each position.

The image size used for the  $xy$  planes in APG case I and III are typically  $150 \times 150 \text{ mm}^2$ . The time  $t$  was also increased to keep  $u_d / u_{rms}$  close to 2.

The  $xz$ -planes measured in APG case III are about  $90 \times 90 \text{ mm}^2$ , but in this case there are mean velocities out of the plane and  $t$  must be shorter. Therefore the errors due to peak-locking also increases. The number of particles inside

the interrogation area decreases closer to surface and in  $xz$  measurements at  $y < 4$  mm there are less than five particles in the  $ia$ . Another source of noise when the laser sheet is close to the surface are particles and scratches on the Plexiglas that reflect light.

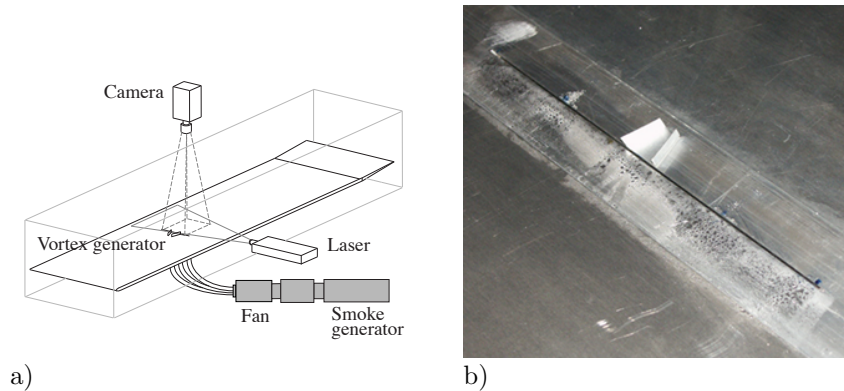


FIGURE 3.11. Smoke visualization set-up. (a) Schematic showing the main components and (b) a photograph of a vortex generator and the smoke inlet slit.

### 3.2.3. *Smoke visualization*

A smoke visualization was carried out before the hot-wire experiments in the MTL wind tunnel. The smoke was injected into the tunnel from a pressurized chamber through a 1 mm slot downstream of the VGs, see figure 3.11 a) and b). A continuous laser illuminated an area from the slot and approximately 250 mm downstream of the slot. Above the enlightened area a high speed (8.22 Hz) digital camera was mounted in the traversing system slot in the test section ceiling.

The laser sheet was adjusted to be parallel to the plate. At  $z = 0$  (the test section spanwise centreline) the sheet thickness was 2.5 mm, spanning  $y = 3-5.5$  mm. 300 images were taken at each visualised configuration.

### 3.3. Vortex generators

The geometry of the vortex generators (see figure 2.3) that were used to create pairs of counter-rotating vortices near the wall is summarised in table 1. The blade angle is  $15^\circ$  and the design follows the criteria suggested by Percy (1961). The four different sizes are geometrically "self-similar". Figure 3.12 shows a schematic of the generated vortices and where they induce outflow and inflow in the wall normal direction.

Although no direct measurements of the generated circulation were made it can be estimated as

TABLE 1. Physical dimensions of the VG sets used in the experiment.

$h$ (mm)	$d$ (mm)	$l$ (mm)	$D$ (mm)	$l/h$	$D/h$	$Z/D$
6	12.5	18	50	3	8.33	15
10	21	30	83	3	8.33	9
18	37.5	54	150	3	8.33	5
30	62.5	90	250	3	8.33	3

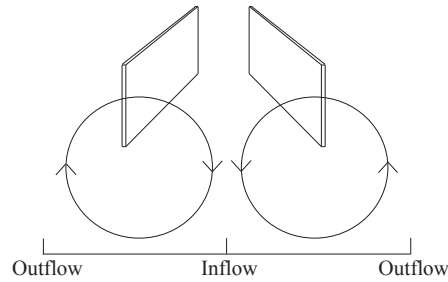


FIGURE 3.12. Vortex generator geometry. The flow direction is out of the picture. All of the VG configurations produce counter-rotating vortices with a common inflow.

$$\Gamma_e = 2hU \quad (3.1)$$

for a VG pair where  $U$  is the mean velocity at the VG blade tip. The estimation is rough but makes it possible to rank the different VG configuration in terms of circulation generated. This is of course possible only if the blade angle is constant for all configurations. This simplified procedure of classification was first used by Angele & Muhammad-Klingmann (2005a). Later it will be shown that this method works in a consistent way. For an array of vortex generators, like in figure 3.13, it is better to estimate the circulation generated per unit width

$$\gamma_e = 2 \frac{hU}{D} \quad (3.2)$$

Note that in the case of the VG pair the estimated production of circulation increases linearly with  $h$ , but for the array the VG density increases with decreasing blade height, *i.e.*  $h/D$  is constant. The parameter that makes  $\gamma_e$

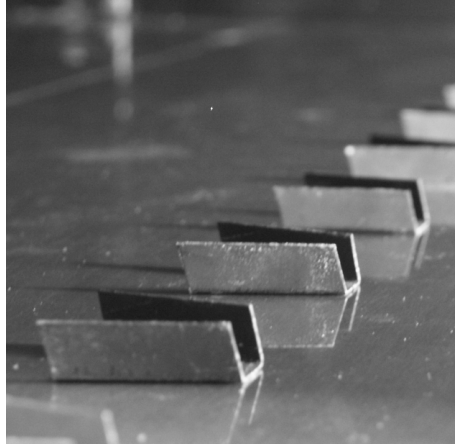


FIGURE 3.13. An array of 10 mm vortex generators. The flow direction is from right to left.

increase with  $h$  is  $U$  that is getting larger as the the blade height increases and reaches higher up in the boundary layer.

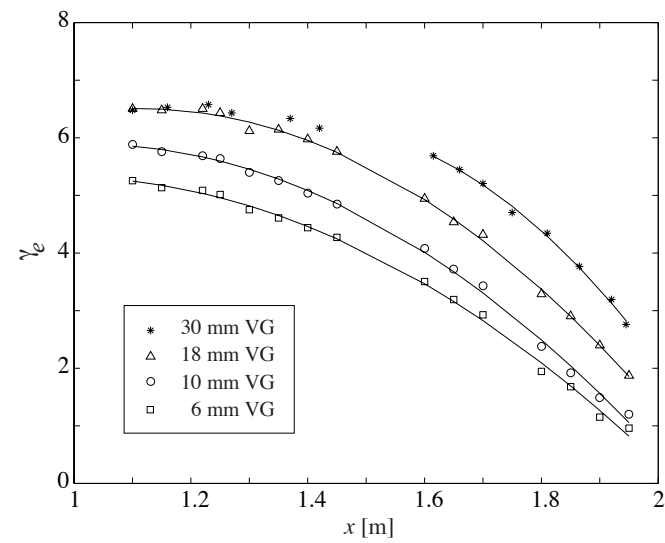


FIGURE 3.14. Estimated production of circulation per unit width in APG case III for the arrays described in table 1.

The circulation is varied by means of changing the VG absolute height and, in the APG case, by varying the  $x$  position and thereby changing the relative height to the boundary layer thickness. A way to illustrate how  $\gamma_e$  varies with  $x$  position and blade height is shown in figure 3.14. Profiles of streamwise velocity were measured at 15 positions from  $x = 1100$  mm to  $x = 1950$  mm. Then  $\gamma_e$  is calculated for the four different values of  $h$  at each  $x$  position, using equation 3.2. The lines are second order polynomials fitted to the calculated points by a least-square method. Note that the more upstream half of the points in the case of  $h = 30$  mm do not follow the curve. This is because the blades reach up out of the boundary layer, where the velocity does not increase any more. The first two estimated points of  $h = 18$  mm are also outside the boundary layer.

Since  $\gamma_e$  is a measure of  $U$  it appears to be possible to find the approximate point of separation by extrapolating the 6 mm VG curve to  $\gamma_e(x) = 0$  m/s in figure 3.14. Note that this is the position of zero mean streamwise velocity at  $y = 6$  mm and that the point of separation is defined as the streamwise position of zero mean velocity at the wall (actually a small distance above the wall). Even so, the velocity gradient close to the position of separation is small (cf. figure 5.4) and therefore the positions of  $U = 0$  close to the wall and at  $y = 6$  mm, respectively, is at approximately the same streamwise position. The position of separation is predicted to be at  $x \approx 2.03$  m if the 6 mm VG curve fit is extended to  $\gamma_e(x) = 0$  m/s. The measured point of separation in this pressure gradient is at  $x = 2.09$  m. Thus, this method does not predict the point of separation very accurate. If  $U$  was measured closer to the wall the accuracy would probably be improved.

## CHAPTER 4

### Zero pressure gradient experiments

In this chapter it is first shown that the turbulent boundary layer that develops on the flat plate in the MTL wind tunnel has the characteristics that are typical for a zero pressure gradient boundary layer. The main part of this chapter, however, describes the development of the longitudinal vortices behind pairs and arrays of VGs. The influence of the size of the VGs is investigated as well as the effect of yaw and free stream turbulence.

#### 4.1. The turbulent boundary layer without vortex generators

The zero pressure gradient experiments were performed in the MTL wind tunnel, described in section 3.1.1. At all velocity measurements the free stream velocity  $U_\infty$  was set to 26.5 m/s and the temperature was kept constant at 18.1°C. Single-wire velocity measurements were performed at nine different streamwise positions from  $x = 500$  mm to  $x = 4500$  mm. The main features of the boundary layer are presented in table 2. According to Österlund (1999) the boundary layer is fully developed, in the sense that there exists a significant logarithmic overlap region, when  $Re_\theta > 6000$ . In the present experiment  $Re_\theta$  reaches a value of 6000 a small distance upstream of  $x = 2000$  mm.

Skin friction is not measured independently, but calculated from  $Re_\theta$  using the equation

$$c_f = 2 \left[ \frac{1}{\kappa} \ln(Re_\theta) + C \right]^{-2} \quad (4.1)$$

Österlund *et al.* (2000) fitted this relation to a large set of data obtained using oil-film and near-wall methods in the MTL wind tunnel. The values of the constants determined in this way are  $\kappa = 0.384$  and  $C = 4.08$ . Since the constants were obtained under similar conditions as the present in MTL they could be applied to the present experiment with some confidence. When the skin friction is known the friction velocity can be calculated as  $u_\tau = U_\infty (c_f/2)^{1/2}$

In figure 4.1 the mean velocity profiles, except from the most upstream and downstream  $x$ -positions, are shown in inner scaling. Österlund (1999) performed very comprehensive and accurate velocity measurements in the MTL

TABLE 2. Description of the ZPG boundary layer

$x$ (mm)	$U_\infty$ (m/s)	$u_\tau$ (m/s)	$1000 c_f$	$Re_\theta$	$\theta$ (mm)	$\delta_*$ (mm)	$H_{12}$	$\delta_{99}$ (mm)
500	26.4	1.09	3.41	2260	1.28	1.88	1.47	10.4
1000	26.4	1.04	3.09	3670	2.08	3.02	1.45	17.2
1500	26.4	1.00	2.89	5100	2.89	4.01	1.39	23.7
2000	26.4	0.98	2.77	6370	3.60	5.04	1.40	29.9
2500	26.4	0.97	2.68	7540	4.26	5.97	1.40	35.9
3000	26.5	0.96	2.61	8710	4.90	6.78	1.38	41.6
3500	26.5	0.95	2.55	9780	5.51	7.66	1.39	47.5
4000	26.5	0.94	2.50	10770	6.07	8.63	1.42	53.2
4500	26.6	0.93	2.45	12200	6.86	9.62	1.40	60.2

wind tunnel and found the slope of the logarithmic region to be  $\kappa = 0.38^1$ . But the traditional value of  $\kappa = 0.41$  fit the present set of data better as can be seen from the figure. This is probably due to less accurate measurements of the probe's  $y$ -position in experiments reported here.

## 4.2. The turbulent boundary layer with vortex generators

### 4.2.1. Smoke visualisation

The basic set-up of the smoke visualisation is described in section 3.2.3. A 6 mm vortex generator pair was mounted immediately upstream of the slot (figure 3.11 b)). The free stream velocity was approximately 25 m/s and the camera exposure time was set to 0.10 ms for a good compromise between light and resolution. The light vertical line that can be seen on the figures 4.3 b) at  $x/h \approx 4$  is just a small step between the smoke injection insert and the flat plate that is reflecting light.

The case without vortex generators can be seen in the instantaneous image in figure 4.2. The lower limit of the laser sheet is at  $y = 3$  mm and it is evident that the smoke is not diffused high enough to be illuminated by the laser until  $x/h \approx 8$ . The structures are quite clearly seen from  $x/h = 10$  to  $x/h = 30$ . From what can be seen on the image the illuminated area looks like a normal turbulent boundary layer.

An instantaneous image taken with the configuration in figure 3.11 b) can be seen in figure 4.3 a). Since the smoke is lifted up to the laser sheet by the

<sup>1</sup>Note that the constant  $\kappa$  is determined from velocity measurements in this case. The value given earlier is determined from wall-shear stress measurements.

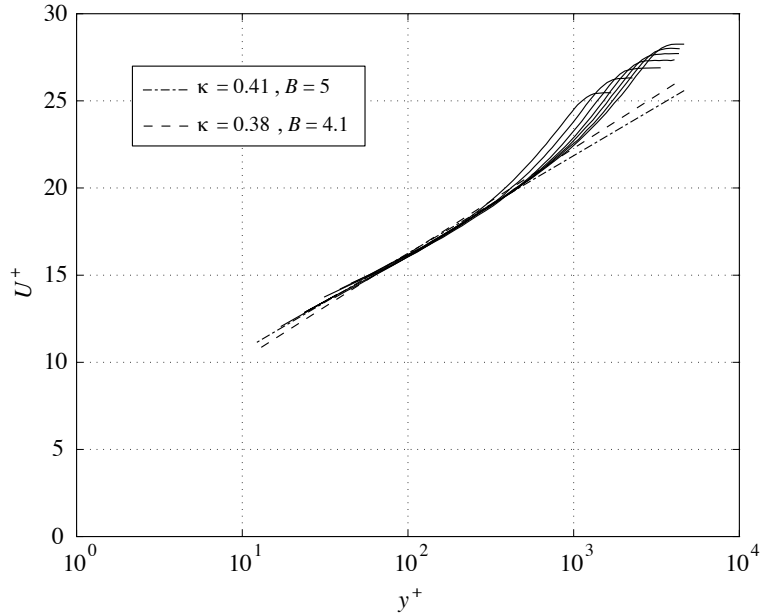


FIGURE 4.1. Mean velocity profiles in inner-law scaling. The dashed and the dash-dotted lines show  $U^+ = \kappa^{-1} \ln y^+ + B$ .

vortices, it can be seen instantly after the injection slot. The vortices produce clear smoke bands that do not move very much from image to image. When VGs are added to the single pair to form an array, the smoke bands from the neighbouring VGs seem to converge from about  $x/h = 25$  (figure 4.3 b)).

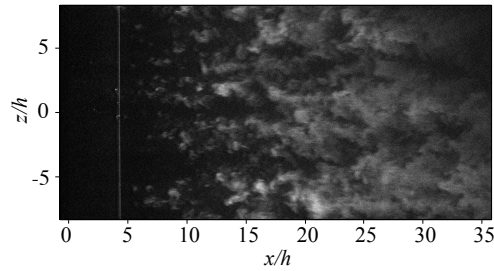


FIGURE 4.2. An instantaneous image without vortex generator. The smoke is injected at  $x/h = 0$  but is not visible until approximately  $x/h = 7$  when the particles are diffused high enough to be in the enlightened zone..

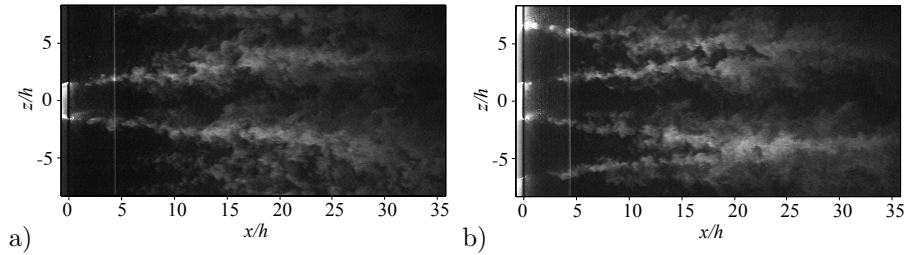


FIGURE 4.3. Instantaneous images at 26.5 m/s with one vortex generator a) and five vortex generators b).

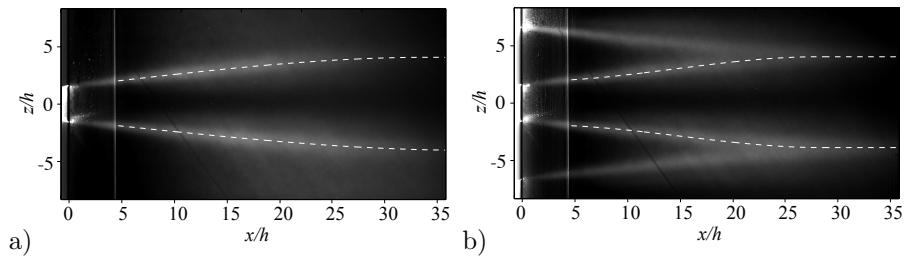


FIGURE 4.4. All the 300 images averaged, with dashed lines indicating the peak light intensity. a) One vortex generator. b) Five vortex generators.

Figure 4.4 a) shows the mean of 300 images taken of the VG pair configuration and figure 4.4 b) shows an averaged image of the VG array configuration. This produces an image where the light intensity indicate the probability of the smoke band being at that position. A least-square fit was made to the light intensity peaks of each pixel column to produce the white dashed lines. Note that the lines do not show the paths of the vortex centres. It is rather the position of maximum mean positive velocity in  $V$  at  $y = 3-5.5$  mm. Thus the vortex centre paths are located somewhere in between the white lines.

In figure 4.5 the two lines from figures 4.4 a) and b) are compared. The light intensity variation across the image is also shown at a number of  $x$ -positions. The reduction of the peak height, with increasing  $x$ , is a combination of smoke diffusion and an increase in vortex size. Somewhat surprisingly, the lines for the VG pair and the VG array seem to collapse, but it should be noted that in the area where they were expected to deviate - the most downstream part of the image - the smoke density is getting lower and the results are less reliable.

Compared to the rest of the experiments the visualisation is made close to the VGs and there is not enough hot-wire data in this region to draw any lines showing the vortex centre paths. But the vortex centres in the two most

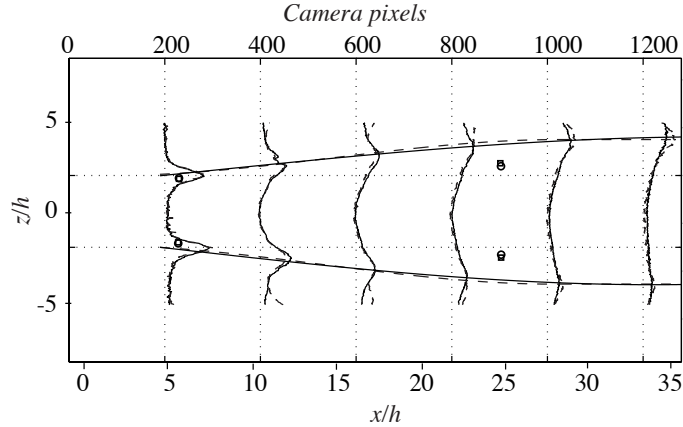


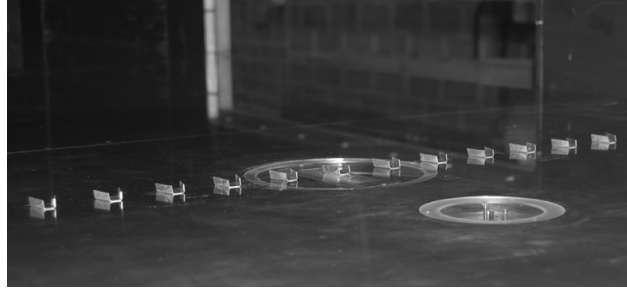
FIGURE 4.5. The white lines from figure 4.4 a) and b) superimposed on each other. The full line is the case with one VG and the dashed line with five VGs. Also shown is how the light intensity varies in the spanwise direction at six  $x$ -positions. The circles and the squares indicate the position of the vortex centres in the VG pair and the VG array configurations, respectively, from the hot wire measurements.

upstream measurement planes are indicated in figure 4.5. In both VG configurations they are clearly located in between the smoke lines.

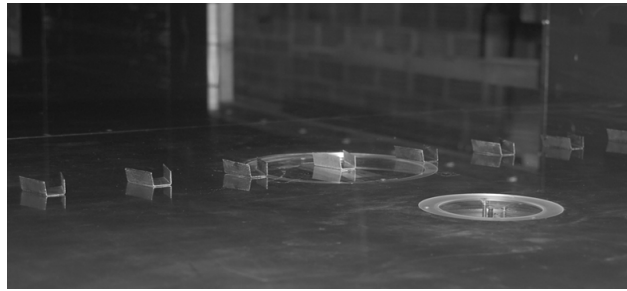
#### 4.2.2. Configurations

The three vortex generators that are used are described in section 3.3. They are tested as single VG pairs and as VG arrays. Arrays of all three blade heights are shown in figure 4.6. The spanwise extension of the arrays is  $\approx 660$ – $750$  mm and thus they do not span the whole width of the test section, only about 55–65%. For the 6 mm array 13 VGs are used, for the 10 mm array nine VGs are used and the 18 mm array consists of five VGs. The vortex generators are mounted with the trailing edge of the blades at  $x = 1830$  mm, where the boundary layer have reached  $Re_\theta \approx 6000$ . This is to ensure a fully developed turbulent boundary layer and thus to avoid any peculiarities from the transition process.

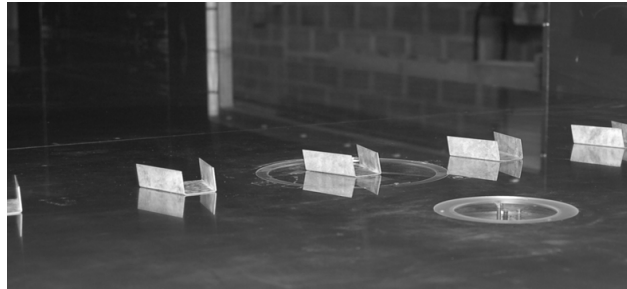
In figure 4.7, the mean streamwise velocity profile at  $x = 1830$  mm, with no vortex generators in the test section, is plotted. The profile is an interpolation from the data at  $x = 1500$  mm and  $x = 2000$  mm. The position of the blade tips of the three vortex generators are also shown in the figure. Their heights relative to the boundary layer thickness  $h/\delta_{99}$  and the velocities at their respective blade



a)



b)



c)

FIGURE 4.6. The three main vortex generator configurations:  
 a)  $h = 6$  mm, b)  $h = 10$  mm and c)  $h = 18$  mm.

tips  $U_h$  are given in table 3. The circulation estimates  $\Gamma_e$  and  $\gamma_e$  are calculated from equations 3.1 and 3.2 and the values are listed in table 3. Later on in this thesis, the generated circulation will be reported.

Table 5 summarises the VG configurations applied in the zero pressure gradient experiments and show what measurements have been made. The reason why not all seven planes are measured for all yaw angles is to save time,

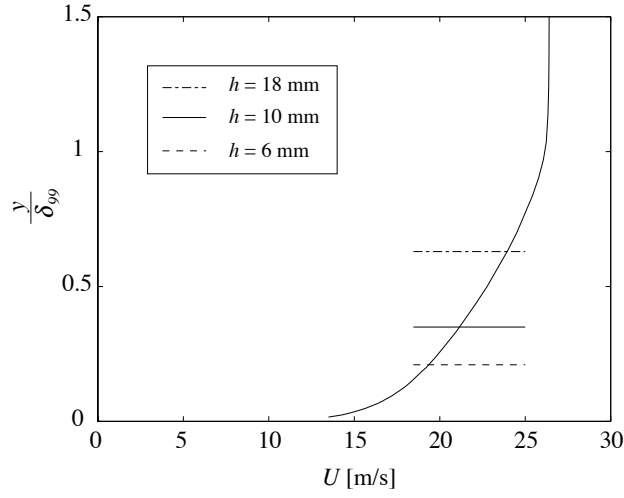


FIGURE 4.7. Mean velocity profile at the VG streamwise position ( $x = 1.83$  m). The horizontal lines show the height of the different vortex generators and the boundary layer height ( $\delta_{99}$ ) is 27.8 mm.

TABLE 3. Estimated circulation for three different sizes of VGs at  $x = 1.83$  m in the MTL wind tunnel.  $\Gamma_e$  is the estimated circulation generated by a VG pair and  $\gamma_e$  is the estimated circulation per unit width generated by a VG array.

	$h = 6$ mm	$h = 10$ mm	$h = 18$ mm
$h/\delta_{99}$	0.22	0.36	0.65
$U_h$ (m/s)	19.6	21.5	24.3
$\Gamma_e$ ( $m^2/s$ )	0.24	0.43	0.88
$\gamma_e$ (m/s)	4.7	5.2	5.8

but also because the vortices disappear out of the measurement plane in the most downstream positions. Unfortunately the traversing system did not allow wider planes in  $z$ .



4.2.3. 10 mm vortex generators at  $0^\circ$  yaw

For obvious reasons not all the data from all the planes will be presented. The 10 mm vortex generator is chosen for a more thorough presentation of all three mean velocity components, the corresponding *rms* values, the streamwise vorticity, the streamwise swirling strength and the turbulent kinetic energy. All seven measurement planes are shown, both for the 10 mm VG pair and the 10 mm VG array.

In figure 4.8 contours of  $U$ ,  $V$  and  $W$  are plotted from  $x/h = 6$  to  $x/h = 267$  for a pair of 10 mm vortex generators. There are clearly some errors in the  $V$ -component even after the corrections described in section 3.2.1. This is due to the difficulty in applying the appropriate correction when there are large velocity gradients in all directions. The  $U$ - and  $W$ -components are symmetric, however the asymmetry in the  $V$ -component is due to the large velocity gradients which affect the cooling velocities of the two wires of the X-probe differently. The maximum magnitude of the cross-flow components is approximately 15% of  $U_\infty$  in  $V$  and 26% of  $U_\infty$  in  $W$  in the first measurement plane downstream of a VG pair. For the VG array it is 13% and 26%, respectively. At this  $x$ -position both  $V$  and  $W$  are symmetrical in the sense that the negative and the positive velocities are of the same magnitude. Since the first plane is located  $6h$  downstream of the vortex generator the real maxima in the secondary components are certainly larger. As expected,  $V$  and  $W$  decrease downstream as the vortex grows. But as far downstream as  $x/h = 267$ , the range<sup>2</sup> of  $V$  and  $W$ , are still 1.8 and 3.2% of  $U_\infty$  in the VG pair case and 2.3 and 2.4% in the VG array case.

The mean velocities of the VG pair can be compared to that of an array in figure 4.9. Most noticeable is the larger symmetry in all three velocity components. With an array of VGs there is a slight increase in the boundary layer thickness. For counter-rotating vortices the  $V$  component of the neighbouring vortices is added and thus it persists longer downstream. For  $W$  the effect of the array is the opposite and this velocity component decays quicker compared to the VG pair case. Both effects are clearly visible in the figure. Whether this influences the generated circulation will be investigated in section 4.2.6.

The turbulence levels in the cross-plane directions increase with the array, as can be seen when figure 4.10 and figure 4.11 are compared. The streamwise turbulence appear to be less affected, although the changed flow structure make a direct comparison difficult.

In figure 4.12 the downstream evolution of the streamwise vorticity  $\omega_x$  (equation 2.12, the swirling strength  $Q_x$  (equation 2.17) and the turbulent

---

<sup>2</sup>At  $x/h = 267$  the wall normal velocity component  $V$  no longer has positive and negative velocities of the same magnitude. This is due to the boundary layer development and it makes the range between the maximum and the minimum value a better measure, when comparing with the still symmetrical  $W$ .

kinetic energy  $k$  is shown. For these parameters no comparison between a pair and an array is made. In the first measurement plane the contours of  $Q_x$  are more symmetrical than the  $\omega_x$  contours. This is due to the exclusion of measured pure shear, which appear to be more afflicted by measurement errors than the swirling motion. The difference in symmetry between  $\omega_x$  and  $Q_x$  disappears in the more downstream measurement planes. The turbulent kinetic energy shown in the third column in figure 4.12 is mainly concentrated to the vortex centres in the most upstream measurement planes. Note how the common downflow between the vortices creates a small region of lower turbulence around  $z = 0$ . As the vortices evolve downstream the turbulence is concentrated to the outer up-wash sides of the vortices.

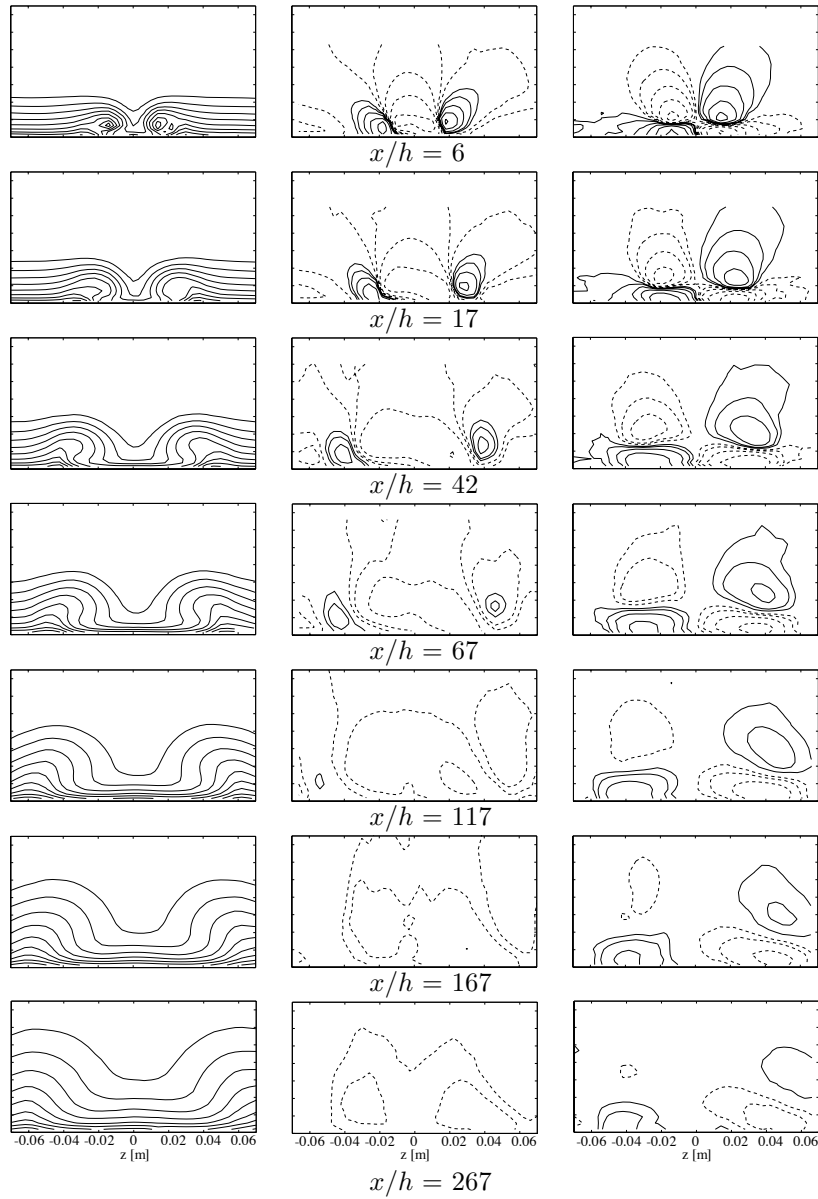


FIGURE 4.8. Mean velocity data at seven positions downstream of a 10 mm VG pair. The first column shows  $U/U_\infty$ , the second column shows the  $V/U_\infty$  and the third column shows  $W/U_\infty$ . For  $U/U_\infty$  the level of the uppermost contour is 0.95 and then the contour increment is 0.05. In  $V/U_\infty$  and  $W/U_\infty$  the starting contour is  $\pm 10^{-7/3}$  and the increment is  $10^{1/3}$

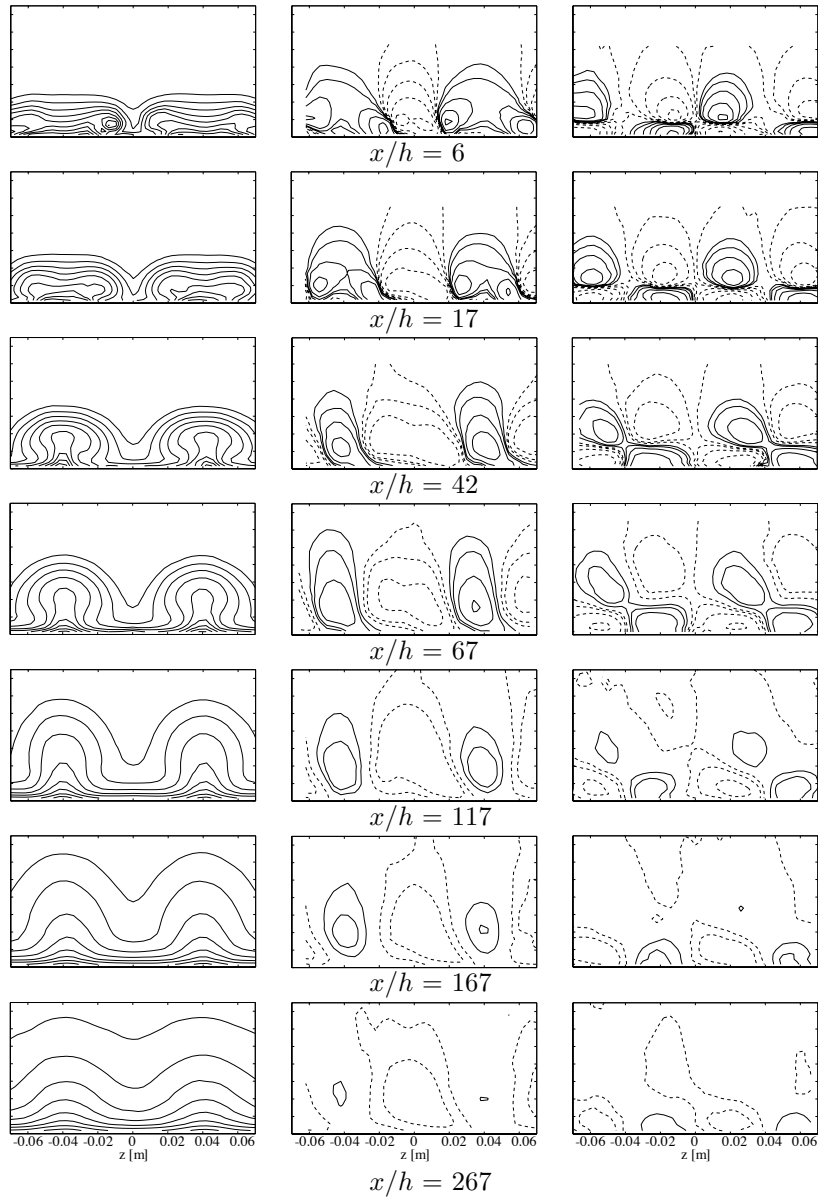


FIGURE 4.9. Mean velocity data at seven positions downstream of one 10 mm VG. The first column shows  $U/U_\infty$ , the second column shows  $V/U_\infty$  and the third column shows  $W/U_\infty$ . The contour levels are the same as in figure 4.8.

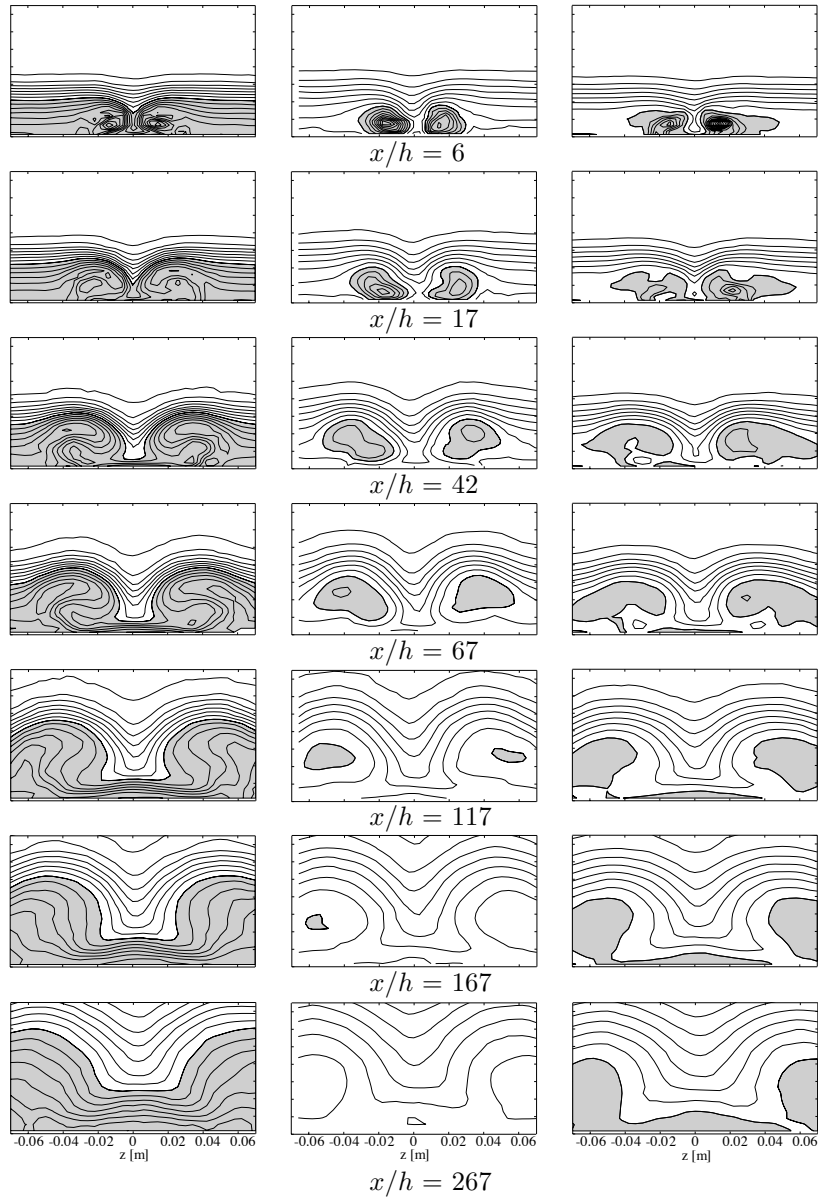


FIGURE 4.10. Turbulence intensity at seven positions downstream of one 10 mm VG pair. The first column shows  $T_u = u_{rms}/U_\infty$ , the second column shows  $T_v = v_{rms}/U_\infty$  and the third column shows  $T_w = w_{rms}/U_\infty$ . The uppermost contour is at 0.5% and the contour increment is 0.5%. The areas where  $T_i \geq 4\%$  are coloured grey.

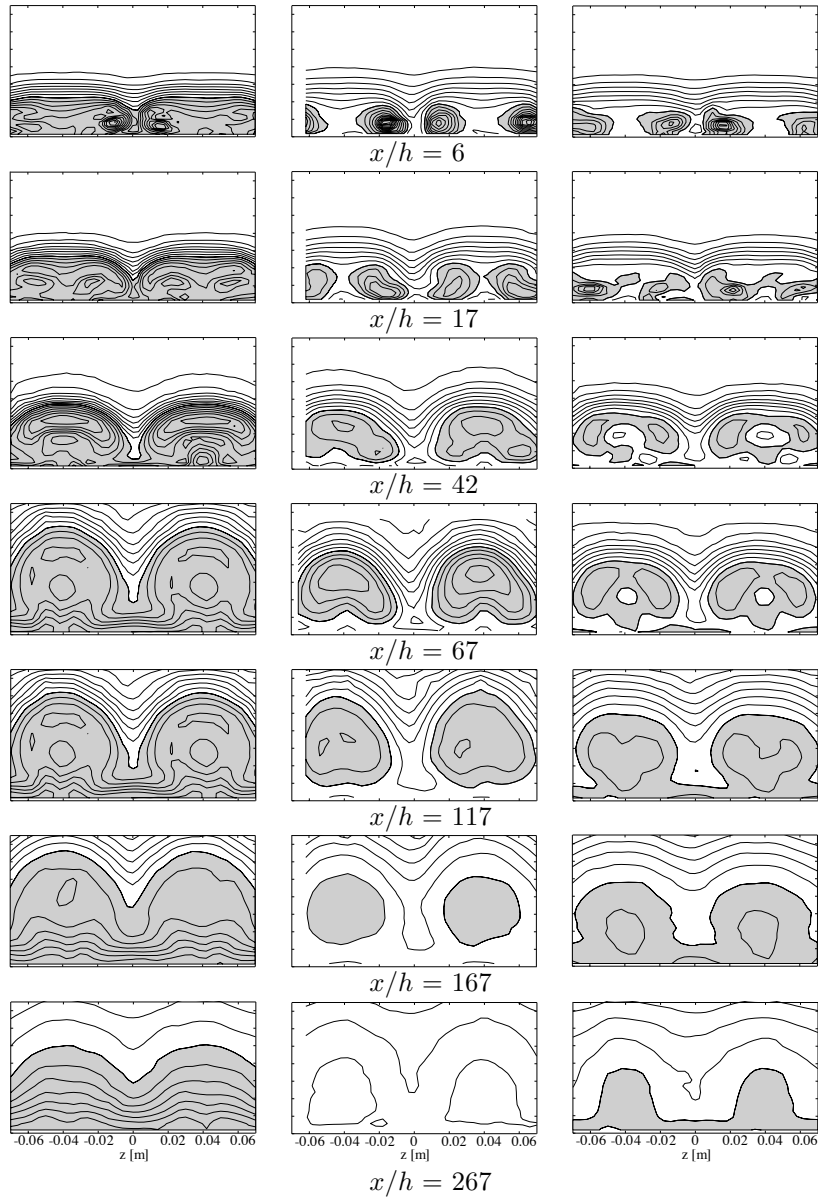


FIGURE 4.11. Turbulence intensity at seven positions downstream of a 10 mm VG array. The first column shows  $T_u = u_{rms}/U_\infty$ , the second column shows  $T_v = v_{rms}/U_\infty$  and the third column shows  $T_w = w_{rms}/U_\infty$ . The uppermost contour is at 0.5% and the contour increment is 0.5%. The areas where  $T_i \geq 4\%$  are coloured grey.

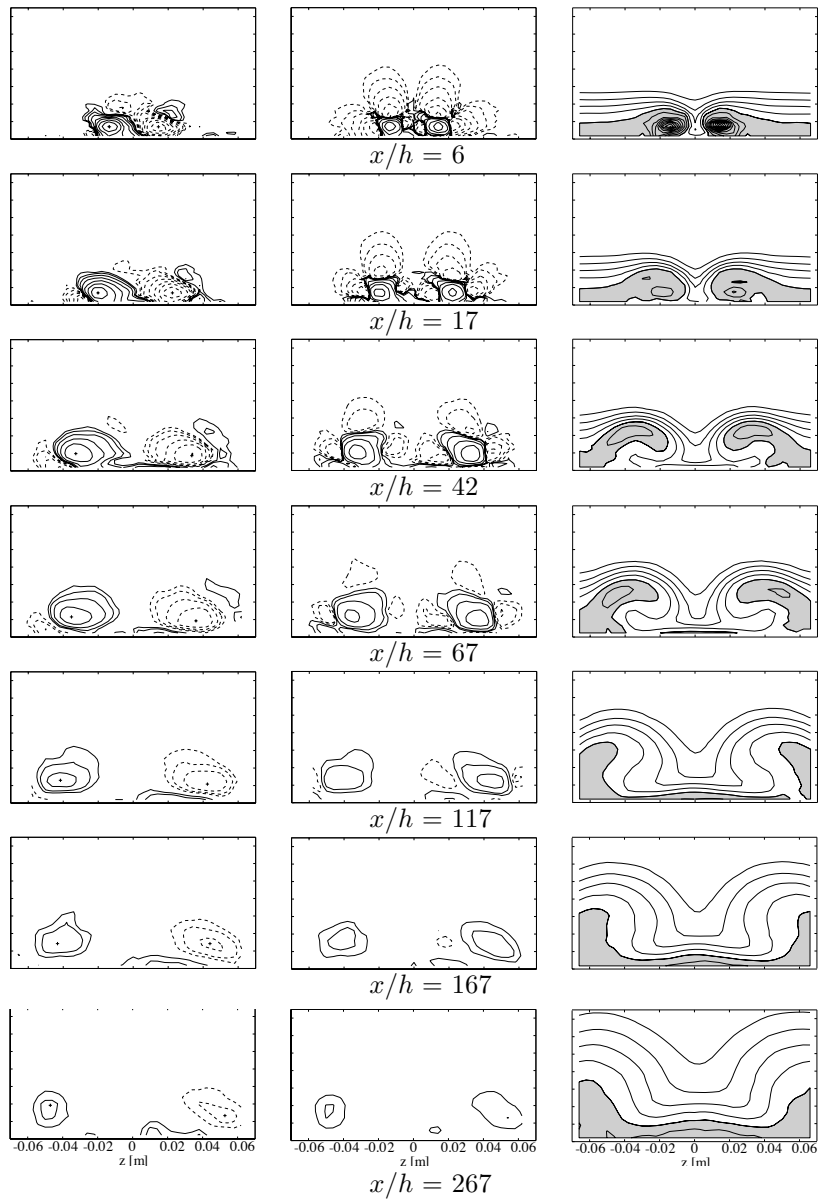


FIGURE 4.12. Data at seven positions downstream of one 10 mm VG pair. The two columns show  $\omega_x$  and  $Q_x$  with logarithmic spacing of the contour lines. The third column shows turbulent kinetic energy.

4.2.4. *Vortex centre paths*

The vortex centre is here defined as the position of maximum absolute streamwise vorticity  $|\omega_x|_{max}$ . Since the measurement grid is quite coarse,  $\Delta z = 7$  mm and  $\Delta y$  varies from 2 to 14 mm depending on  $x$ - and  $y$ -position, a simple interpolation scheme is used in order to estimate the centre of the vortex. To find the vortex centres of each plane the data positions of maximum and minimum streamwise vorticity are identified, for the positively and negatively rotating vortices respectively. Then, a cubic surface fit is performed on the surrounding 24 points ( $\pm 2$  in  $y$  and  $z$ ) in order to produce a  $20 \times 20$  matrix in which a new maximum or minimum is found. Since the peak of maximum absolute vorticity is getting flatter as the vortices are convected downstream and the vorticity is diffused so that the area of the vortex core is increased, the position of maximum/minimum vorticity is more diffuse. Thus the vortex centre coordinates get less precise with increasing  $x$ .

In figure 4.13 a) the vortex centre paths from pairs of 6, 10 and 18 mm VGs are normalised by  $h$  and projected on the  $yz$ -plane. The three curves do not start in the same place, since the first data points are not located at the same normalised streamwise position  $x/h$ . The paths of the vortices downstream the 10 and 18 mm VGs collapse nicely. When progressing downstream the paths of the two vortices move away from each other; first they sink slightly but then they rise steadily until the last measured streamwise position. The downward motion in the beginning is caused by the induced velocity of the other real vortex, but as the two vortices move away from each other this influence is getting smaller and the growth of the vortex causes the vortex centre to move out from the wall. It is the vortex mirror images that make the vortex paths diverge, but this is perhaps also partly helped by the vortex growth. However, the paths of the vortices generated from the 6 mm VG pair behave differently. After about  $x/h = 200$ – $250$  they make an unexpected turn and start to converge. A possible explanation to this will be given later on.

Moving on to figure 4.13 b) that show the paths of the vortices generated by VG arrays, they look similar to the one of the 6 mm VG pair. First they move apart and downward, for the same reasons as in the case of the VG pairs. But in the case of the array, when they move away from each other they are moving closer to the vortex from the neighboring vortex pair and eventually form a new counter-rotating pair – this time with common upflow. The induced velocities in the new pair will tend to lift the vortices and according to inviscid theory (Pearcy (1961)) they will just continue to rise from this point, along an asymptotic value of  $z/h$ . But the measurements show that the vortex centre paths of the original pair, while still rising, start to move toward each other again. This is probably due to vortex growth; when the vortex core areas grow the vortices are forced to a spanwise equidistant state. The influence from the other vortices (real or mirrored) is decreasing with increasing  $x$ . At

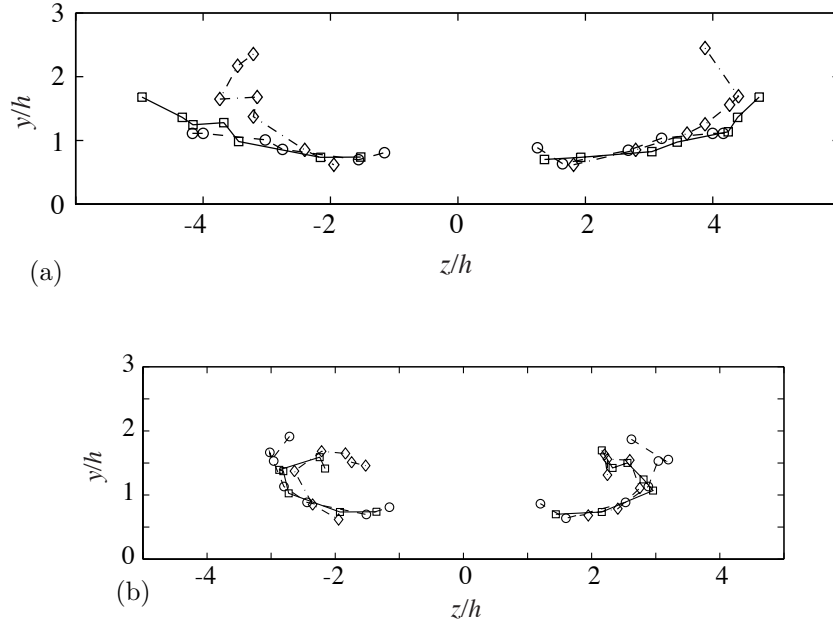


FIGURE 4.13. Vortex centre paths plotted in a plane normal to the stream (the  $yz$  plane). ( $\diamond$ ,  $\square$ ,  $\circ$ ) denotes  $h_{VG} = (6, 10, 18$  mm). Figure a) shows the paths downstream of a vortex generator pair and b) shows the same planes for an array of vortex generators .

$x/h = 50$  the circulation is reduced to half of the initial value and thus the induced flow is equally reduced. Since the distance between the VG pairs of the array is  $D$  and since this space will contain two vortices, the maximum vortex radius of in an equidistant system of circular vortices is  $D/4$ . If the distance from the vortex centre to the wall is  $D/4$ , the induced velocities from the real vortices and the three closest mirror vortices all cancel. The following mirror vortex images will produce small, alternating positive and negative, forces in the spanwise direction and the system will be nearly balanced. In these experiments  $D/h = 8.33$  and thus  $D/4 = 2.08h$ . Hence, if the assumption holds, the vortex centres should approach  $(y/h, z/h) = (2.08, \pm 2.08)$ . In figure 4.14, these coordinates are marked with small circles, whereas the large circles show the maximum size of a circular spanwise equidistant vortex. There seem to be a tendency for the vortex centres to move towards the predicted

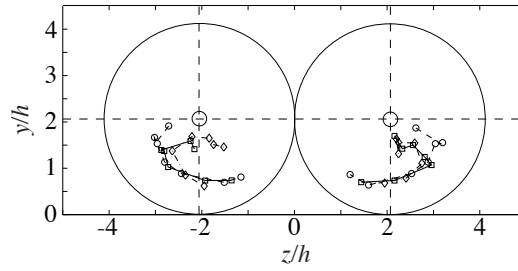


FIGURE 4.14. Two circles with radii =  $2.08 h$  illustrating the available area for circular equidistant vortices. The curves are the cross-plane vortex centre paths for the VG array case.

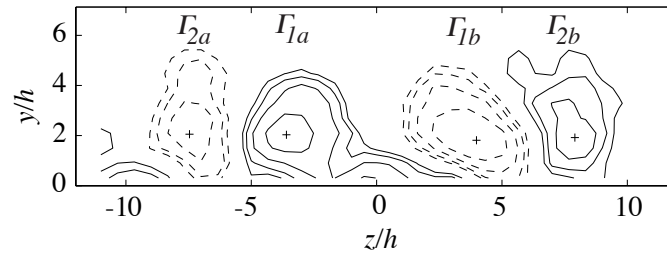


FIGURE 4.15.  $\omega_x$  in the  $yz$ -plane at  $x/h = 278$ , downstream of a 6 mm VG pair.  $\Gamma_1$  and  $\Gamma_2$  denotes the circulation of the primary and secondary (induced) vortices. The solid lines indicate positive vorticity and the dashed lines negative vorticity.

position, especially when the added difficulty of finding the vortex centres in the most downstream planes is taken into account. Note that the data points that deviates the most from the assumption are all from downstream positions in the 6 mm VG case.

Now it is possible to explain the odd vortex centre paths produced by the 6 mm VG pair in figure 4.13 a). In analogy to the paths of the vortices generated by the array, the curving back motion appears to indicate the existence of more vortices, outside of the primary pair. The three most downstream planes ( $x/h = \{194, 278, 445\}$ ) certainly show two more vortices flanking the original ones. The new secondary vortices are relatively strong: at  $x/h = 194$  their circulation is about 25% of that of the primary vortices and at  $x/h = 278$  they have reached a level of slightly less than 50%. At  $x/h = 445$  a small part of the secondary vortices are outside the measurement plane, but the major part is

inside and the circulation is about 55% of the primary vortices. Note that the circulation of the primary vortices have ceased to decay in this region and thus that the secondary vortices not only increase in strength relative to the primary vortex pair, but that they also grow in absolute numbers. Partly this is due to their increasing distance from the wall, that move more of the secondary vortices into the measurement plane, but mainly this increase in circulation must be due the continuous vorticity transfer from below the primary vortices to the up-wash regions. In figure 4.15, the plotted vorticity contours reveal the existence of an outboard pair of induced secondary vortices at  $x/h = 278$ .

The secondary vortices originate from the very thin layer of stress-induced opposing  $\omega_x$  under the primary vortex. This layer is too thin to detect in the experiments reported here, but is described by Shabaka *et al.* (1985). According to Pauley & Eaton (1988) there is some evidence that the layer of opposing vorticity is convected out to form a small low momentum region of opposing vorticity on the upflow side of the main vortex and close to the wall. To the authors knowledge it has not been shown before how this induced vorticity is rolled up into a vortex that rises up from the wall to influence the vortex centre path of the primary vortex.

In figure 4.16 a) the vortex paths from the VG pairs are shown in plan-view. The paths from the 6 mm VGs continue to  $x/h = 445$ , but in order not to compromise the resolution the figure is cut at  $x/h = 300$ . This also applies to figures 4.16 b) and 4.17. A divergence of the paths, from all VG sizes, caused by the mirror images can clearly be seen. The angle of divergence increases with vortex strength. The induced vortices cause the 6 mm paths start to converge from about  $x/h = 200$ , but this is perhaps hard to distinguish.

Vortex centre paths downstream of VG arrays are plotted in figure 4.16 b). In contrast to the paths of the pairs these paths all collapse, when normalised by the VG blade height. In plan-view it is perhaps easier to see the "overshoot", when the paths move apart at the same speed as in the case of the pair, up to about  $x/h = 50$  and then how they asymptotically converge towards spanwise positions that probably are close to  $z/h = \pm 2.08$ .

Shabaka *et al.* (1985) suggested that since turbulence diffuses both the boundary layer and the vorticity the proportion between vortex size and boundary layer thickness should remain constant at all  $x$ -stations for isolated vortices in a boundary layer. For a circular vortex, this implies a vortex centre that move out from the wall with the increase of the boundary layer thickness. According to the inviscid theory of Pearcy (1961) the interaction of the vortex pairs will make them move out from the wall linearly after a dip in the beginning. Earlier in this chapter it was suggested that the vortex centres will move towards a constant height  $y = D/4$ . In figure 4.17 the vortex centre paths are plotted on a plane parallel to the stream. The wall normal position is normalised by  $h$  and the boundary layer thickness  $\delta_{99}$  for the different VG

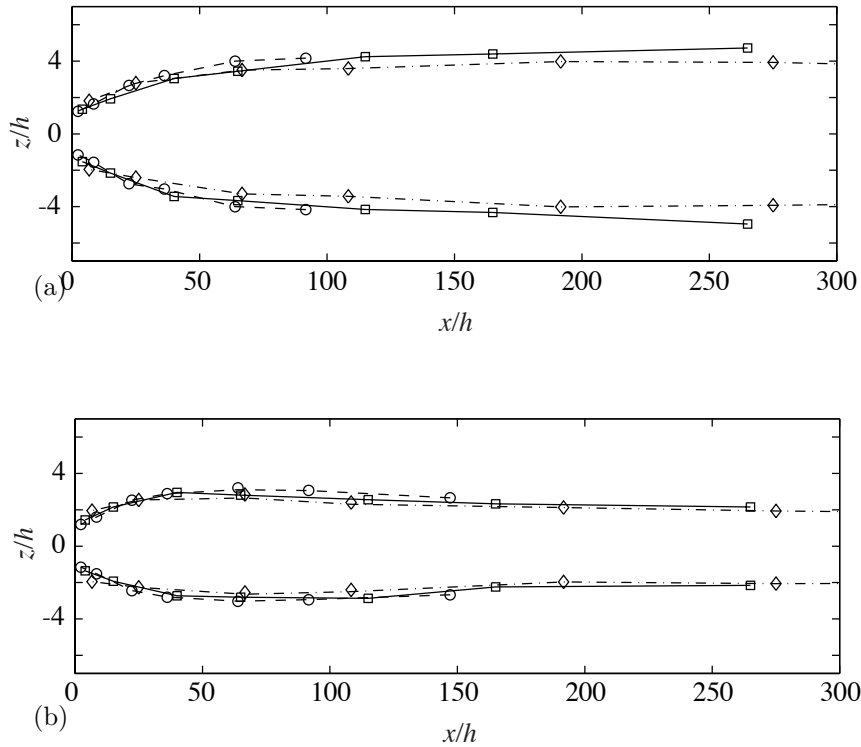


FIGURE 4.16. Vortex centre paths plotted in plan-view (the  $xz$ -plane). ( $\diamond$ ,  $\square$ ,  $\circ$ ) denotes  $h_{VG} = (6, 10, 18$  mm). Figure a) shows the paths downstream of a pair of vortex generators and b) shows the same planes for a vortex generator array. Note that for the array the paths of the neighboring vortices are actually within the figure area, but for the sake of clarity they are not shown.

sizes are also shown in the figure. It is obvious from the figure that the vortex centre height does not scale with the boundary layer thickness regardless of configuration. The paths seem to scale with  $h$ . The pairs in figure 4.17 a) continue rising through the test section, but the arrays in figure 4.17 b) seem to reach a constant height of  $y/h = 1.5$ – $2$ . Since the vortex centre position is a bit vague in the most downstream planes it is difficult to draw any conclusions, but the hypothesis that the centres stay at  $y = D/4$  have not been convincingly proven. When  $y_c < D/4$  the induced velocities from the mirror images produce a force towards the neighbouring vortex with which it shares a

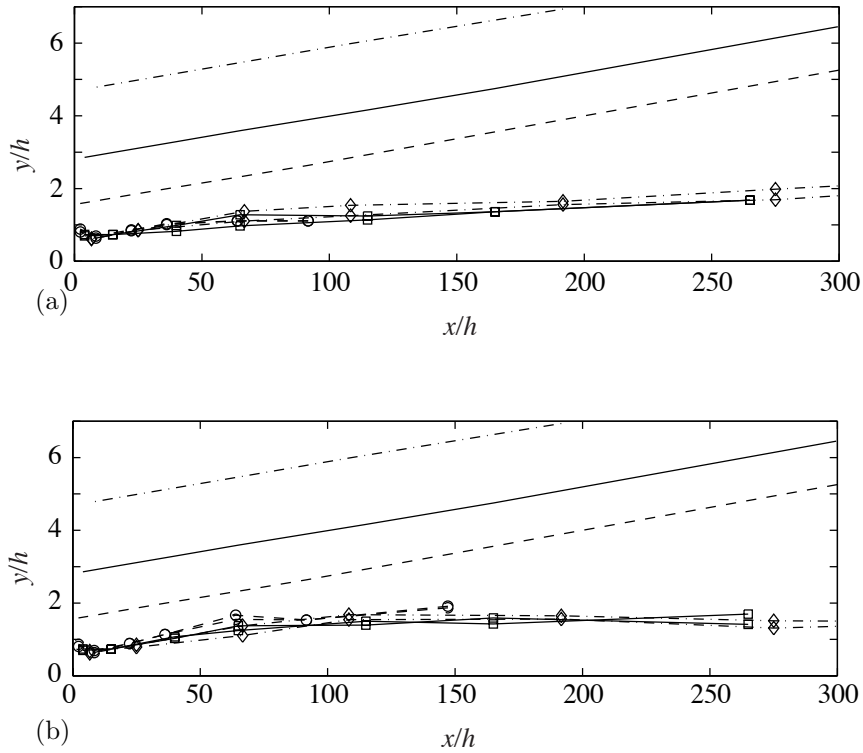


FIGURE 4.17. Vortex centre paths plotted in a plane parallel to the stream (the  $xy$ -plane). ( $\diamond$ ,  $\square$ ,  $\circ$ ) denotes  $h_{VG} = (6, 10, 18)$  mm). Figure a) shows the paths downstream of a pair of vortex generators and b) shows the same planes for a vortex generator array. The dash-dotted line shows the boundary layer thickness in the 6 mm case, the solid line is the 10 mm case and the dashed line is the 18 mm case. Note that the scale of the  $z$ -axis is more than 10 times that of the  $x$ -axis.

common outflow. But the paths in figure 4.13 b) and 4.16 b) show no tendency to diverge. Thus there must be an opposing force.

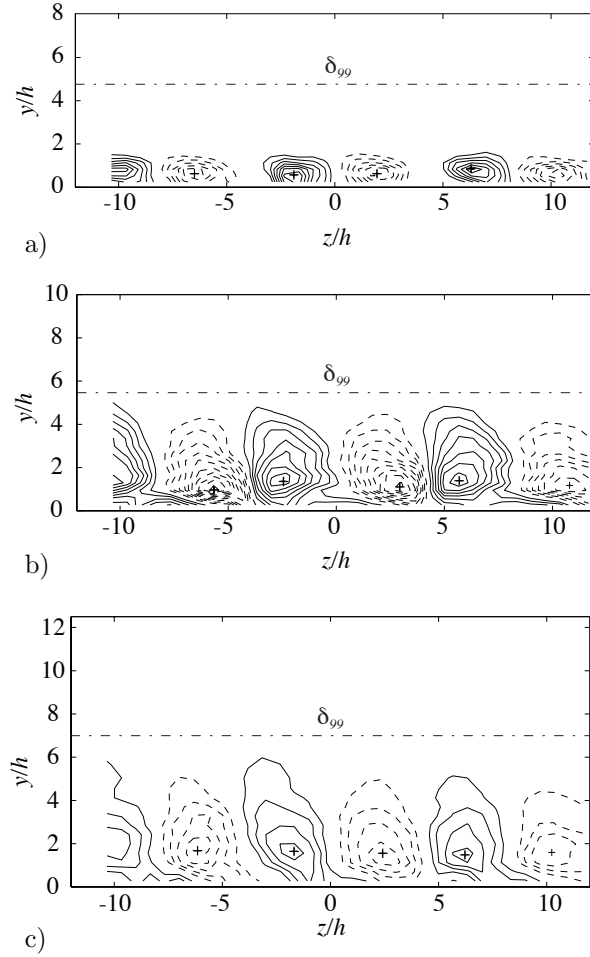


FIGURE 4.18. Streamwise vorticity contours ( $\omega_x$ ) at three  $x$ -positions downstream of an array of 6 mm vortex generators. Solid lines indicate positive vorticity and dashed lines negative vorticity. The small + show the positions of the vortex centres and the horizontal dash-dotted line corresponds to  $y = \delta_{99}$  without any vortex generators. a)  $x/h = 10$ , b)  $x/h = 69$  and c)  $x/h = 194$ .

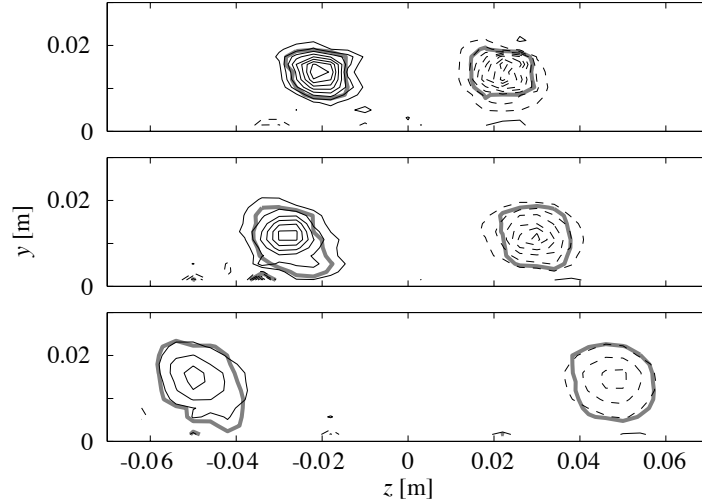


FIGURE 4.19. Contours of  $\omega_x/(U_\infty/h)$  in the first three planes after a 18 mm vortex generator pair. The thick contour  $Q_x = 0.05 Q_{x,max}$  encompasses the vortex core area  $A$ .

#### 4.2.5. Vortex growth

In figure 4.18 the shape of the vortices produced by 6 mm VGs is shown. At the first station ( $x/h = 10$ ), shown in figure 4.18 a), the vorticity contours indicate a quite flat, horizontally elongated, vortex. When the vortices have been convected down to  $x/h = 69$  they have changed shape and are now vertically elongated due to the spanwise space constraint. In figure 4.18 the vortex core area is the same in position  $x/h = 69$  and  $x/h = 194$ , but the vortex shape is different. At  $x/h = 194$  the vortex is more compressed in the spanwise direction and hence even more vertically elongated. In some sense the vortex seems to grow with the boundary layer, even though the area does not grow.

To determine the vortex core area ( $A$ ) its centre is first identified and then the area of the region where  $Q_x \geq 0.05 Q_{x,max}$  is calculated. Note that  $Q_{x,max}$  refer to the local maxima of the measured plane. The choice of cut-off level is of course somewhat arbitrarily, but chosen after tests of what level gives the most consistent results. The same cut-off level was used by Angele & Grewe (2002). Figure 4.19 shows the vortex areas of some measurement planes.

Figure 4.20 a) shows  $A$  as a function of downstream position for the VG pairs. The area presented is the average of the two counter-rotating vortices. No method of normalising the data made the curves collapse and thus the dimension is kept. To compare the vortex area with the boundary layer thickness

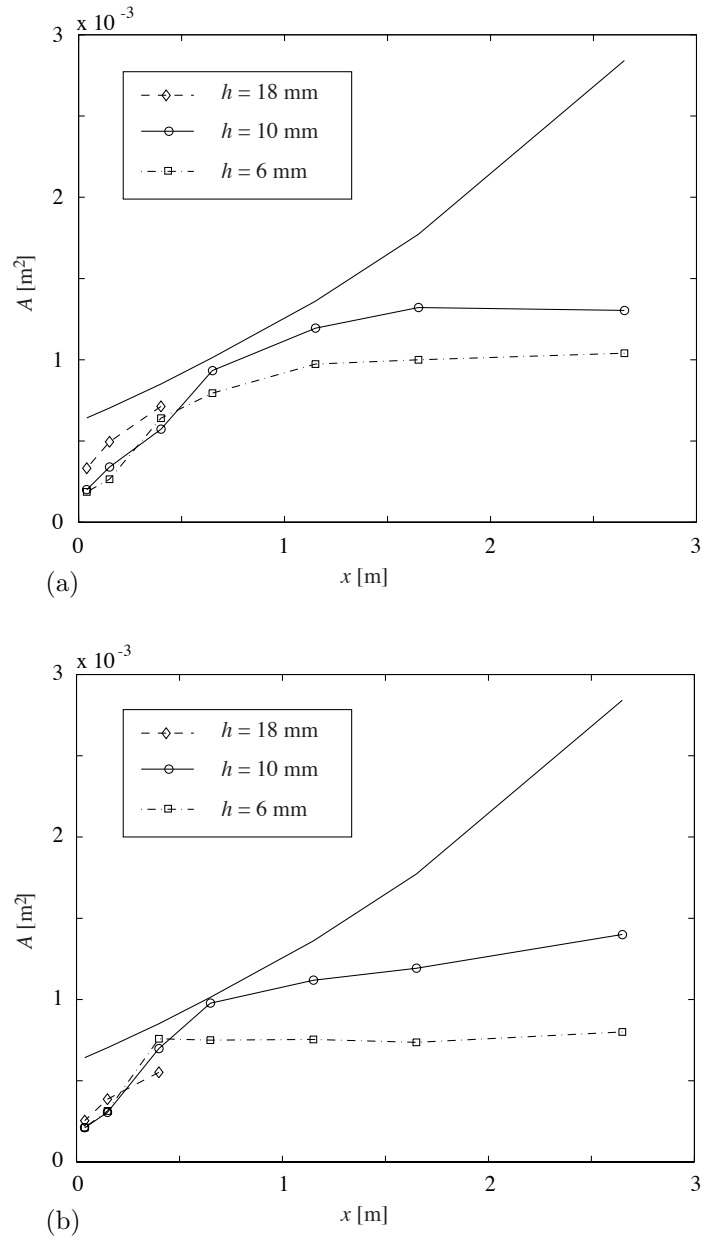


FIGURE 4.20. Vortex core area development. Average vortex area for vortices produced by a) a VG pair and b) an VG array. The line is the area of the largest possible circle to fit between the wall and  $y = \delta_{99}$  (see figure 4.21).

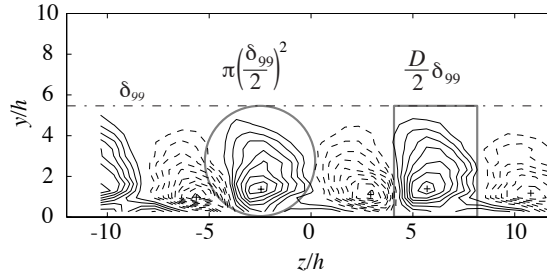


FIGURE 4.21. A circle fitted between the wall and  $y = \delta_{99}$  (uncontrolled case) and a rectangle fitted within the same height as the circle and with the width  $D/2$ .

a boundary layer area ( $A_{99}$ ) is defined as the area of a circle inscribed between the wall and  $y = \delta_{99}$ . If the vortex is circular and is to stay confined in the boundary layer  $A_{99}$  is the largest possible vortex size. In the case of the pairs the vortex area grows quickly in the beginning and then gradually levels off at about  $x = 1-1.7$  m or  $x/h \approx 170$ . It then stays quite constant. The 10 mm VG vortex grows close to  $A_{99}$ , but the vortex generated by the 6 mm VG vortex never reach that size. Unfortunately the vortices from the 18 mm VG move out of the measurement plane. Otherwise it would have been interesting to see whether they stay contained by the boundary layer.

The core area development for the vortex arrays is slightly different (see figure 4.20 b)). The 10 mm VG vortex grows even quicker in this case, but when the vortex area is equal to  $A_{99}$  the growth rate decreases abruptly. In both regions the growth is approximately linear. The 6 mm vortex display a similar behavior, with two quite linear phases. However, in this case the core area stays approximately constant in the second region.

There are, at least, two possible area constraints, or reference areas, for longitudinal vortices embedded in the boundary layer. Firstly, a circle can be inscribed below the boundary layer. This is the area  $A_{99}$ , mentioned above. Secondly, a square of  $D/2$  spanwise width can be fitted in the boundary layer. These two constraints are shown in figure 4.21 and they are valid if the vortices are to stay embedded in the boundary layer. Then there are two additional reference areas for vortex arrays: for circular equidistant vortices the maximum vortex area  $A_{max} = \pi(D/4)^2$  and in case of equidistant square areas  $A_{max} = (D/2)^2$ .

In figure 4.22 the core area development of the vortices produced by 6 mm and 10 mm VG arrays are compared to the four main reference areas. No vortices exceed the two boundary layer constraints, but the vortex from the 10 mm array touches the curve of the circle inscribed in the boundary layer.

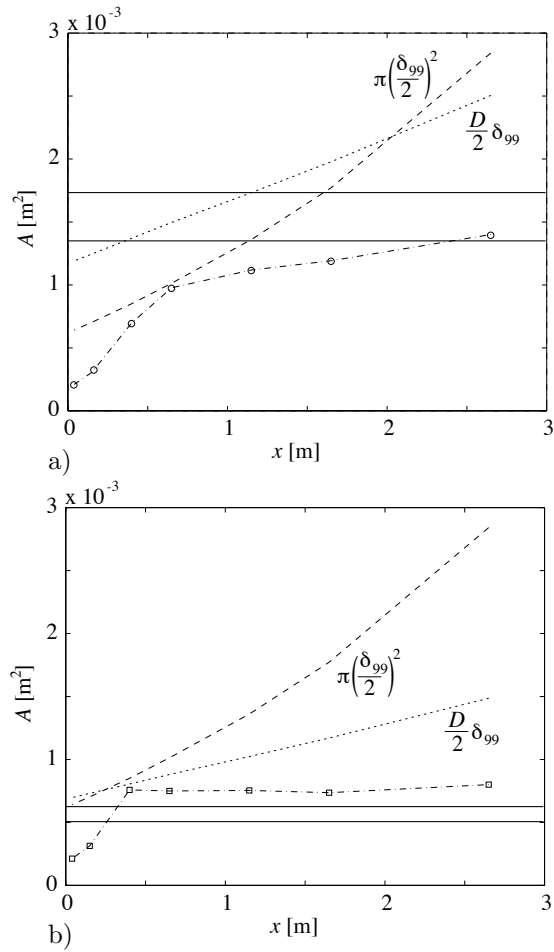


FIGURE 4.22. Vortex area development. In a) the vortices are produced by an array of 10 mm VGs and in b) by an array of 6 mm VGs. The two horizontal solid lines represent the equidistance constraints: the lower line shows the area of equidistant circles and the upper line the area of equidistant squares.

The area of the vortex generated by the 6 mm VG array touches the curve of the square in the boundary layer and thus the vortex most likely extends outside the boundary layer at that  $x$ -position. As mentioned earlier the growth can be divided into two different phases and during the second phase of slower growth

the area of the the 10 mm VG vortex exceed the constraint of circular equidistant areas. This indicates a vertically elongated, *i.e.* more elliptical vortex. The vortices from the 6 mm array quickly grow larger than both the equidistant area constraints. Thus, the vortices are even more vertically stretched than the 10 mm VG vortices. This can also be seen in figure 4.18. Since the distance to the wall from the vortex centre stay the same (figure 4.13 b)), the streamwise vorticity peak is no longer at the geometrical centre of the vortex. The reason why the area stops growing in the second phase is probably due to the fact that the vortices are as stretched as is possible. If this assumption is correct the area growth of the 10 mm VG vortices will continue until they are approximately 20% larger than the square equidistance constraint.

#### 4.2.6. Circulation decay

According to Kelvin's circulation theorem the circulation around a closed material circuit in an inviscid fluid is conserved. Thus the circulation would remain constant as the vortices are convected downstream from the VGs. In the present experiment the no slip condition at the wall generates a spanwise shear stress component that reduces the angular momentum, and hence circulation, of the vortex.

The vortex circulation is calculated by integrating the streamwise vorticity over the area  $A$

$$\Gamma = \int_A \omega_x dA \quad (4.2)$$

where  $A$  is defined as the area enclosed by the contour  $Q_x = 0.05 Q_{x,max}$ , as can be seen in figure 4.19. Since the aspect ratio and angle of attack is the same for all three VG sizes it is appropriate to normalise them by the height  $h$  and the streamwise velocity at the blade tip  $U_h$ . If the equations for estimated circulation are correct the data, for the different VG sizes, normalised by  $h$  and  $U_h$  will collapse.

In figure 4.23 the downstream development of circulation for the 6, 10 and 18 mm VG pairs is presented. The three curves collapse well. Down to  $x/h \approx 200$  the circulation seems to decay exponentially, but further downstream the circulation appear to reach a constant level. This is somewhat surprising, but it should be noted that this conclusion is based on data points where the circulation is difficult to calculate.

The data in figure 4.23 are re-plotted in in figure 4.24, where the asymptotic value has been subtracted, using a logarithmic scale for the axis of ordinates. This shows fairly convincingly that the decay initially is exponential.

For the arrays of vortex generators the decay look different as can be seen in figure 4.25. Instead of a smooth curve there seem to be two almost linear parts. The vortex core area development show a similar difference between the pairs

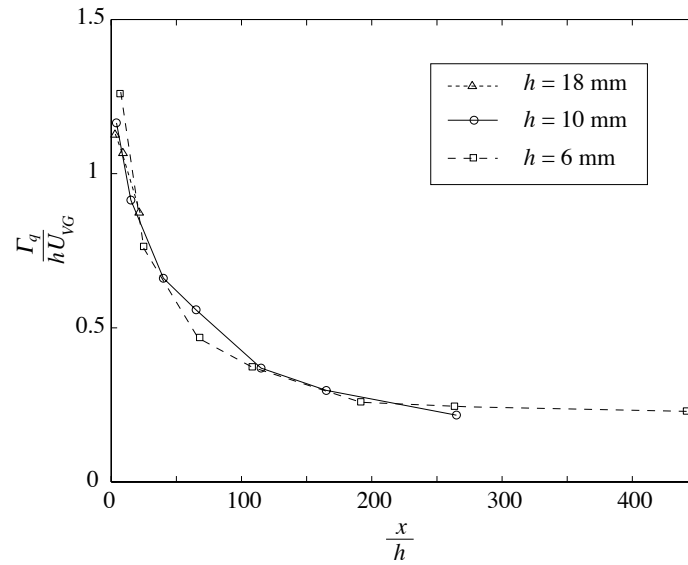


FIGURE 4.23. Decay of normalised circulation with  $x/h$  for vortex generator pairs.

and the arrays (cf. figure 4.20) and there is a connection, since the circulation is an integration of the vorticity over the vortex core area. The overall level of circulation is not very different compared to the VG pairs. Even so, the last data point indicates a higher rate of decay for the vortices produced by the array when  $x/h > 300$ . In section 4.2.3 it was shown that the spanwise velocity component  $W$  decreased quicker in an array of vortices compared to a pair. The wall normal component  $V$  decreased slower in the array but  $W$  is larger than  $V$  at all downstream positions. Thus  $W$  seems to be dominant in determining the level of circulation and the array ought to decay slightly faster than the pair.

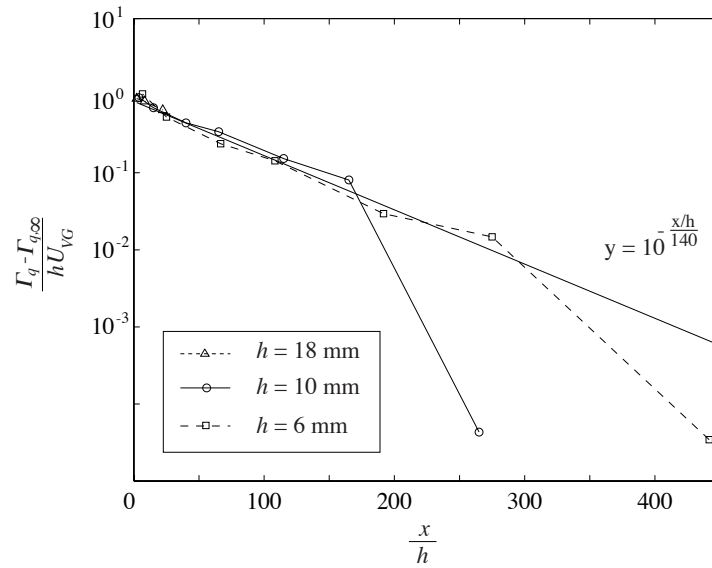


FIGURE 4.24. Decay of  $(\Gamma_q - \Gamma_{q\infty})/(hU_{VG})$  with  $x/h$ . The line  $y = 10^{-\frac{x/h}{140}}$  is fitted to the data points  $x/h \leq 200$ .

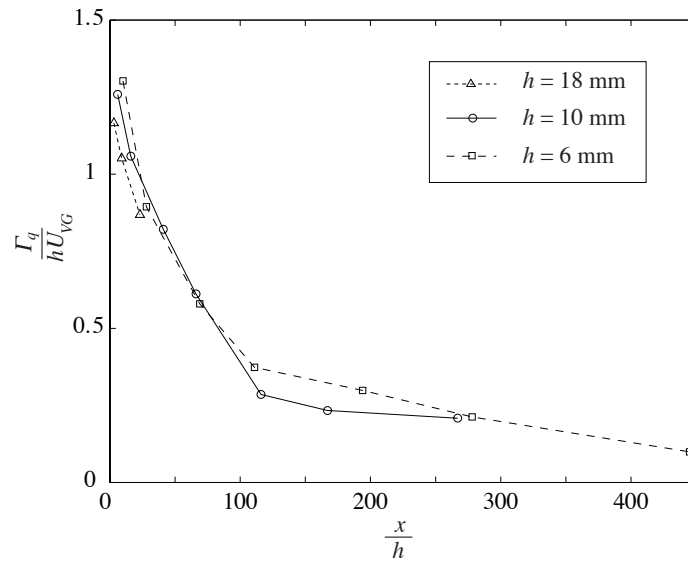


FIGURE 4.25. Decay of normalised circulation with  $x/h$  for vortex generator arrays.

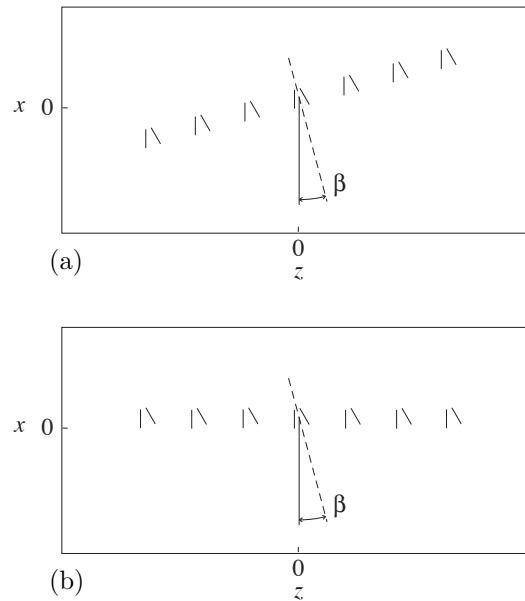


FIGURE 4.26. Two different ways of yawing vortex generators. The lower one was used in the present work.

#### 4.2.7. Yawed vortex generators

In practical applications, especially on ground vehicles, the VGs operate in yaw most of the time. Therefore it is of interest to study vortex generation and decay under such non-ideal conditions. To do this the 10 mm pair and array of vortex generators were tested at yaw. Yawing an array can be done in at least two different ways: either by yawing the whole array as one unit (figure 4.26 a)) or by yawing the individual VG pairs (figure 4.26 b)). In this experiment the VG pairs are yawed individually in order to have the same boundary layer thickness at all blades and thus produce the same circulation for all VGs. It is of course slightly inconsistent to yaw the VG pairs unitwise, when the array is not yawed as a unit. This is done for practical reasons and the difference in streamwise position between the two blades of each pair is still very small. A photograph of the set-up in the test section is shown in figure 4.27

The yaw angles tested were 0, 5, 10, 15 and 20°. They were chosen to be relevant for flow control on ground vehicles, such as trucks. Since the blade angles in a VG pair is  $\pm 15^\circ$  one blade will increase its absolute angle and the other blade will show a decreased absolute angle. The positive blade will be yawed to 15, 20, 25, 30 and 35° and the negative blade to -15, -10, -5, 0 and

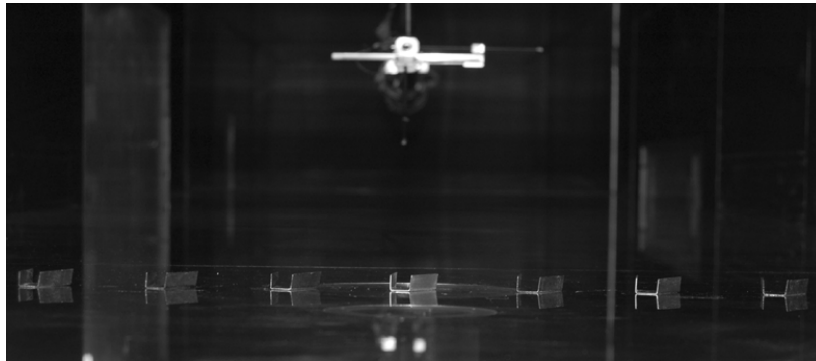


FIGURE 4.27. An array of 9 vortex generator pairs at  $20^\circ$  yaw.

$5^\circ$ . Hence the negative blade will be parallel to the flow in one configuration and it seems unlikely that it will produce a vortex at that angle of attack.

Figure 4.28 shows how the streamwise vorticity, produced by a VG pair, evolves downstream at different yaw angles. The vortex from the VG blade that is decreasing its angle of attack gets weaker as the VG pair is yawed, but there is still a region of positive vorticity left downstream of that blade at  $20^\circ$ . Since the "weak" blade would generate negative vorticity at  $20^\circ$  if the other blade was removed, it is perhaps reasonable to believe that this region of positive vorticity is induced by the stronger vortex. Even so, there is a continuity of the  $\omega_x$  contours at increasing yaw that seem to indicate that there is still a rest of the weaker vortex even at  $20^\circ$  yaw.

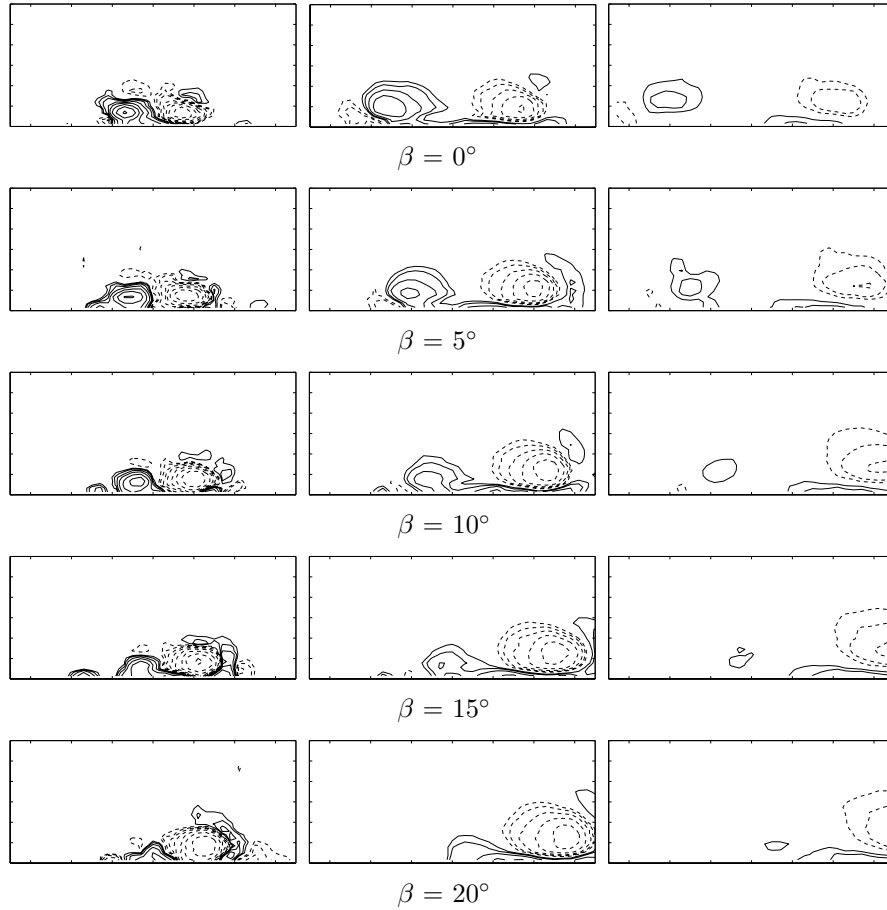


FIGURE 4.28. Normalised streamwise vorticity  $\omega_x/(U_\infty/h)$  in three planes downstream of a 10 mm VG pair that is yawed between  $0^\circ$  and  $20^\circ$ . The first column shows the measurement plane at  $x/h = 6$ , the second at  $x/h = 42$  and the third at  $x/h = 117$ . The lowest value contours are at  $\omega_x/(U_\infty/h) = \pm 10^{-7/4}$  and the contour increment is  $10^{1/4}$ .

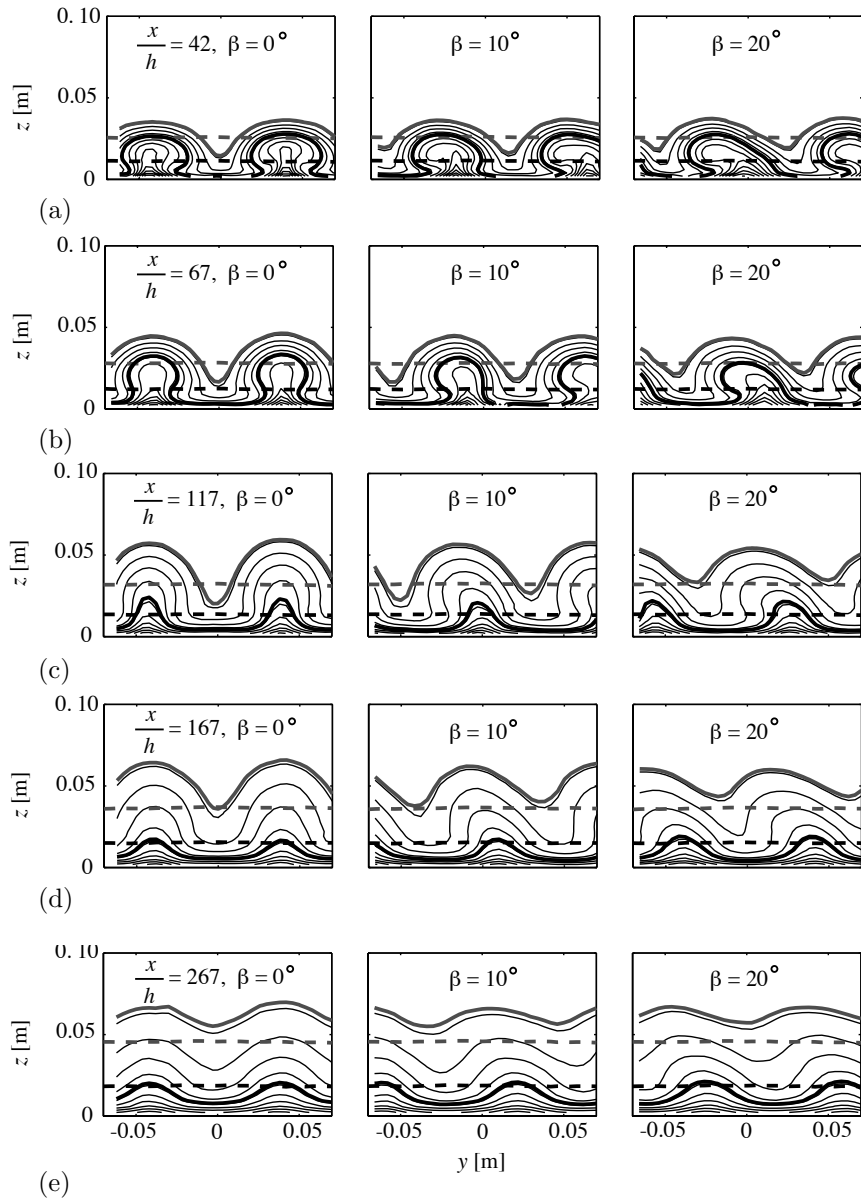


FIGURE 4.29. Contours of streamwise velocity at several  $x$ -positions downstream an array of 10 mm vortex generators at 0, 10 and  $20^\circ$  yaw. The dotted grey and black lines corresponds to  $y = \delta_{95}$  and  $y = \delta_{80}$  respectively, in the vortex free base flow. The thick grey and black lines indicate the same  $y$ -positions for the shown VG cases.

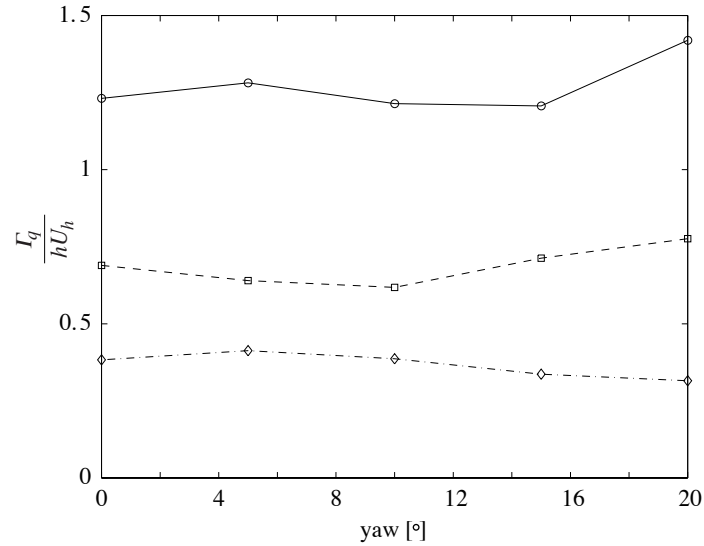


FIGURE 4.30. Total (from both vortices) circulation at (○)  $x/h = 6$ , (□)  $x/h = 41$  and (◇)  $x/h = 116$ . The vortex generators used is a 10 mm pair.

The purpose of introducing vortex generators in a flow is to increase the momentum near the wall. How this goal is affected by yaw is shown in figure 4.29. In this figure the original ZPG boundary layer, without any vortices, is compared to the boundary layer modified by the vortices from an array of VGs at 0, 10 and 20° yaw. In the upper part of the boundary layer ( $y = \delta_{95}$ , where  $\delta_{95}$  is the position where the streamwise velocity is 95% of the free stream velocity) the effect of the vortex generators is to reduce the velocity. This is more prominent in the downstream planes. Closer to the wall ( $y = \delta_{80}$ ) the vortices produce the desired velocity increase. The size of the area between the dotted and the solid black lines give a visual indication of the momentum increase caused by the vortices. This area is almost constant, independent of yaw angle, except, perhaps, for the first plane. This means that the momentum transfer to the lower part of the boundary layer neither decreases, nor increases with yaw. Hence a flow control system based on the tested type of vortex generators will remain stable.

When a VG pair is yawed the absolute angle of attack of one blade is increasing while the angle of attack of the other blade is decreasing. Thus one of the vortices in the counter rotating pair grows stronger and one is getting weaker. It is not obvious whether this is a linear process at both blades and therefore it is difficult to predict the total circulation generated by the VG pair.

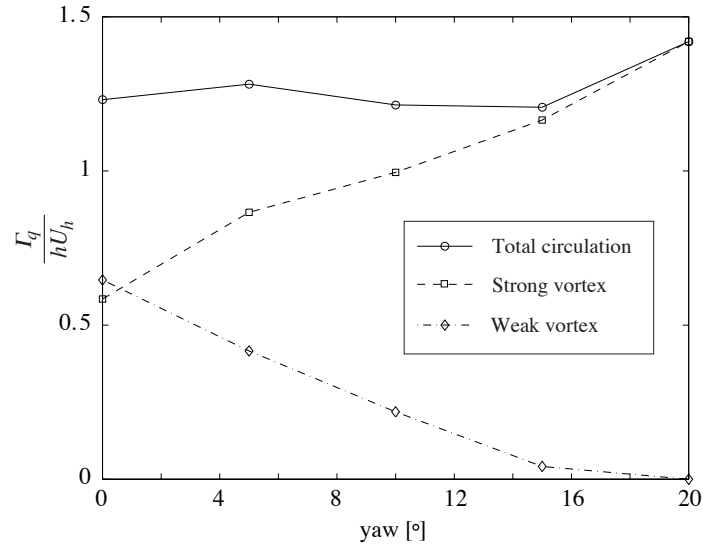


FIGURE 4.31. Circulation at  $x/h = 6$ . It is the same case as in figure 4.30, but with the circulation from the two vortices accounted for individually.

In this case the total circulation, up to a yaw angle of  $20^\circ$ , is almost constant as can be seen in figure 4.30. The circulation decay also seems to be almost independent of yaw. However, at  $20^\circ$  the circulation at  $x/h = 116$  is smaller than expected, when the value is compared to the large initial circulation at that yaw angle. This could be a result of experimental uncertainties or indicate a different flow structure when both VG blades have positive yaw.

In order to better understand the nearly yaw-independent total circulation revealed in this experiment, the two vortices from the VG pair are plotted individually against the yaw angle in figure 4.31. At  $0^\circ$  the two vortices should be of equal strength. The difference shown in the figure is mainly due to the not perfect positioning and manufacturing of the vortex generator and due to measurement errors. When the yaw angle increases the circulation of both vortices changes linearly up to an angle of  $15^\circ$ . According to the figure the blade that is parallel to the flow is still producing a vortex. The reason for this unexpected behaviour could be that the strong vortex is deflecting the flow to reach the parallel blade at an angle or, perhaps, that this is vorticity induced by the larger vortex. The strong vortex continues to gain circulation at  $20^\circ$ , but the weak vortex has disappeared. At this angle of the VG pair the blade producing the strong vortex is yawed  $35^\circ$  and it is likely that the flow will separate. Even so, Wendt (2001) have shown that the circulation generated by

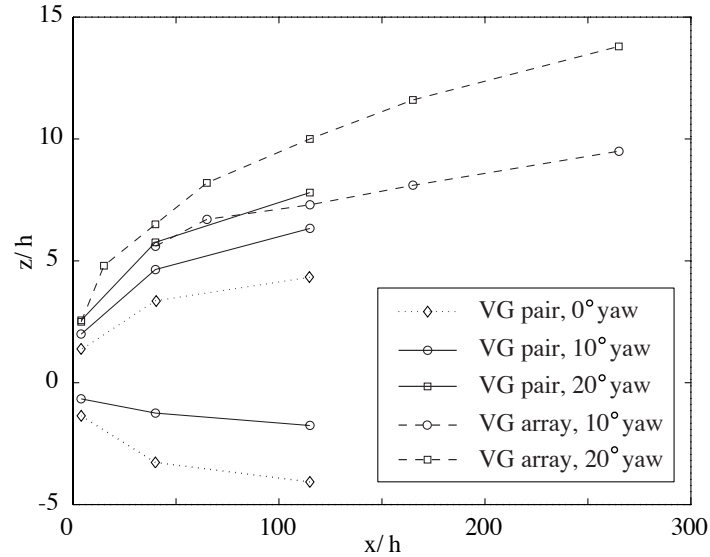


FIGURE 4.32. Vortex paths of VG pairs and VG arrays at  $0^\circ$ ,  $10^\circ$  and  $20^\circ$  yaw. For the VG pairs in  $0^\circ$  and  $10^\circ$  yaw both vortex centre paths are shown.

a VG blade keep increasing even after the blade stalls. By comparing with the circulation of the weak vortex at  $10^\circ$  yaw ( $-5^\circ$  blade angle) it is clear that there should be some circulation generated by the low angle of attack blade at  $20^\circ$  yaw ( $5^\circ$  blade angle). That this is not the case could be due to the possible deflection mentioned above, which might make the blade parallel to the flow or because the weak vortex might have merged with the strong co-rotating vortex.

Also the vortex centre paths are changed at yaw. This is due to the asymmetry when the two vortices of the counter-rotating pair are of different strength. In the  $0^\circ$  yaw case there is no net side force, but as soon as there is a difference in circulation the mirror images will induce a velocity that modify the vortex paths. The paths are deflected in the intuitive correct direction of the centreline of the VG pair. In figure 4.32 the vortex centre paths at different yaw angles can be seen.

When one of the vortices from the VG pair disappears, there is no longer a pair or array of counter-rotating vortices. In the case of a VG pair the result is a single longitudinal vortex. An array of VG pairs at yaw will produce a system of co-rotating vortices. Since the induced velocity of all the mirror images of the array work in the same direction the deflection angle is larger for an array compared to a pair at the same yaw angle. The path of a vortex from a VG pair at  $20^\circ$  yaw is approximately the same as that of a vortex generated in an

array at  $10^\circ$  yaw. It was only possible to track the paths of the vortices from the pair up to  $x/h = 116$  before they were deflected out of the measurement plane, due to the limited spanwise range of the traversing system. In case of the array it was possible to combine the vortex paths that were going out of the plane with the ones coming in from the other side.

#### 4.2.8. Free stream turbulence

Kalter & Fernholz (2001) have shown that the size of a separation bubble is strongly dependent of the free stream turbulence (FST). They managed to first reduce the bubble length and then to completely eliminate any mean reverse flow by increasing the FST. Since the main reasons for fitting VGs on a surface is to delay or prevent separation it is of interest to know how the vortex generation and the vortex decay are affected by the turbulence intensity ( $T_u = u_{rms}/U_\infty$ ). Since the vortices are embedded in the boundary layer where  $T_u$  is about 3–8%, the assumption is that the FST have little influence on the vortices.

In order to increase  $T_u$  a turbulence generating grid (shown in figure 4.33) was mounted approximately one meter upstream of the flat plate leading edge. This changes the turbulence intensity to 1.2% at the streamwise position of the VGs. The only vortex generator configuration tested in an increased free stream turbulence is the 10 mm pair.

In figure 4.34 the downstream development of circulation is shown with and without the grid. In the first planes the measured circulation seems independent of  $T_u$ , but further downstream the lines diverge and the vortices of

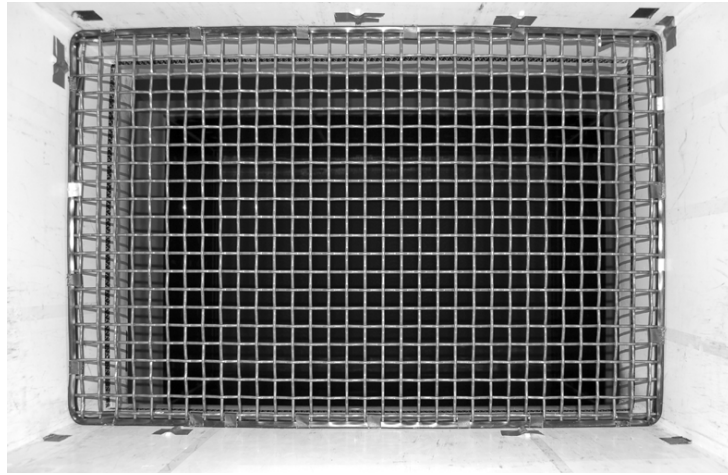


FIGURE 4.33. Grid mounted downstream of contraction. The distance between the wires are 36 mm and their diameter is 5 mm.

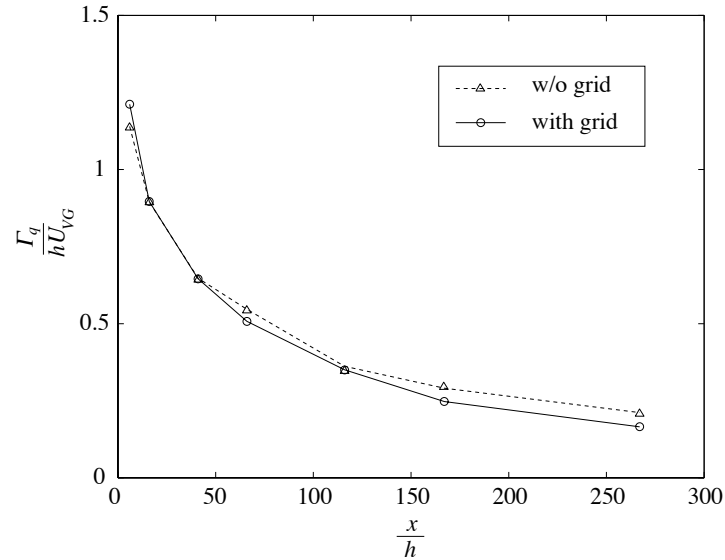


FIGURE 4.34. Circulation decay downstream of a pair of 10 mm vortex generators.

the high FST case decay faster. As expected, the initial magnitude of circulation is independent of the FST. The exponential decay up to  $x/h = 100$ – $150$  is caused by wall friction and the work on secondary vortex structures done by the primary vortices. Those mechanisms are more or less independent of FST and this makes the initial decay independent of FST. Further downstream the gradients are much smaller and other effects might be involved in the decay process. Even though the circulation curves diverge approximately 20% far downstream, the uncertainties involved in determining the circulation in the most downstream planes make it difficult to conclude whether the FST has any influence. In a normal application of vortex generators the area that is to be affected by the vortices are within  $x/h = 150$  and the turbulence level is probably not important.

The mean velocity does not seem to be affected by the increased turbulence intensity. Four  $U$ -profiles, at different spanwise positions, from  $x/h = 116$  are shown in figure 4.35 and although there are some differences between the two cases, they are too small to draw any general conclusions from. The other planes show even smaller differences in  $U$ . In figure 4.35 a) and b) contours of flatness  $F_u$  are displayed. Even though the overall structure is unchanged when the FST is increased the intermittency in the outer part of the boundary layer is reduced. This is even more clear in the flatness profiles of figure 4.35 c)

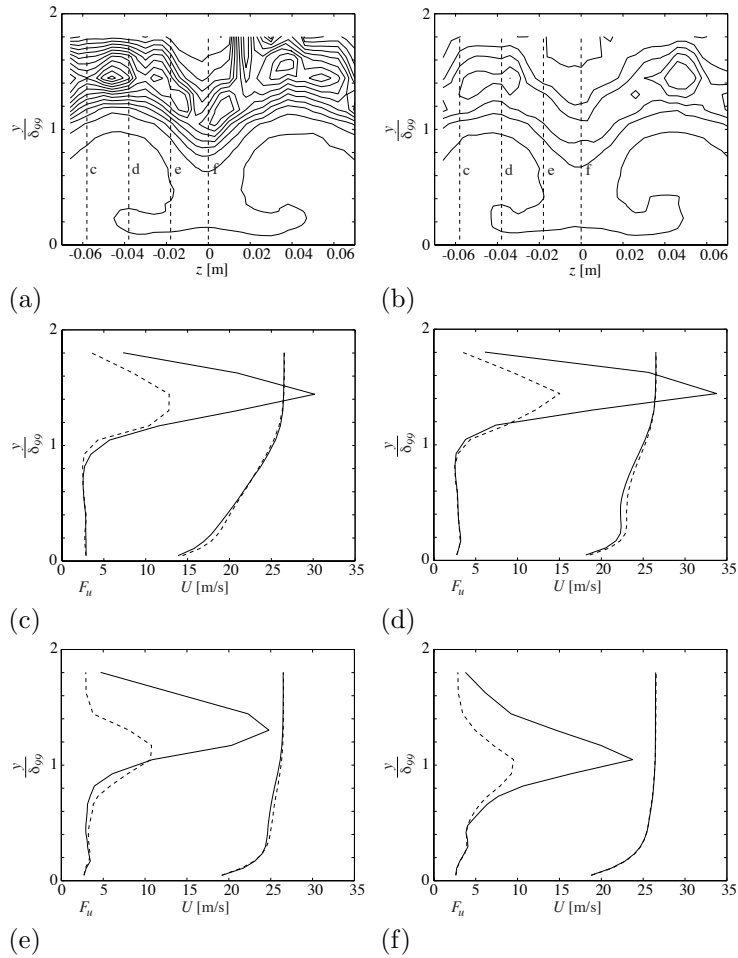


FIGURE 4.35. Flatness ( $F_u$ ) contours without and with grid. The dashed lines in the contour plots show where the  $F_u$ - and  $U$ -profiles a) - d) are measured. In a) - d) the full lines show profiles without the grid and the dashed lines show profiles with the grid mounted.

- f), where the peaks are reduced by approximately 60%. Outside the peak  $F_u$  is close to three. This is most clearly shown in figure 4.35 d).

## CHAPTER 5

### Adverse pressure gradient experiments

After examining the effect of the vortex generators in ZPG in the previous chapter they are now applied in adverse pressure gradient (APG) boundary layer flow. This chapter consists of two parts, first an investigation of the separated flow at different pressure gradients, and then control of the separation using vortex generators. All APG measurements, except those of the static wall pressure, are performed with PIV (described in section 3.2.2).

A separation bubble can be defined in at least three different ways (see section 2.3). Here the separation bubble is defined as the region where backflow occurs more than 50% of the time ( $\chi > 0.5$ ). Furthermore, the terminology proposed by Simpson (1989) will not be used in this thesis. Here "detachment" refer to when  $\chi = 0.5$  at the wall.

#### 5.1. Description of the test flow

All the APG experiments were made in the BL wind-tunnel and the free stream velocity  $U_\infty$  was 26.5 m/s at the inlet of the test section. The temperature was kept constant at 20°C.

The pressure gradient in the test section was set through a contoured wall and by changing the suction rate as described in section 3.1.2. Three pressure gradients are compared here: the first one (case I) is from experiments by Angele & Muhammad-Klingmann (2005a, 2006), in the same basic set-up and the other two (case II and III) are experiments performed by the author. Case I is just separating, case III is the largest possible separation with the present suction fan and geometry and case II is somewhere in between. Case II is the most thoroughly investigated configuration.

The wall static pressure  $P$  was measured along the spanwise centreline using a Furness pressure transducer. The pressure transducer has an accuracy of 0.025 % of full scale (2000 Pa), which in the present experiment produces a measurement accuracy of 1–3 %. In figure 5.1 a) the pressure coefficient

$$C_p = \frac{P - P_{ref}}{P_0 - P_{ref}} \quad (5.1)$$

for the wall static pressure and its gradient in the flow direction are plotted against the distance from the leading edge of the test plate.  $P_{ref}$  is taken on the wall at  $x = 0.45$  m and  $P_0$  is the total pressure at the same  $x$ -position.

The pressure gradient distribution is shaped for maximum pressure recovery; it is large in the beginning and then relaxed further downstream, as proposed by Schubauer & Spangenberg (1960). The adverse pressure gradient is strongest between  $x = 1.6$  and  $1.7$  m, figure 5.1 b). In this area the maximum  $dC_p/dx$  for the three APG cases are evenly distributed, 0.070, 0.078 and  $0.087 \text{ m}^{-1}$ . The separation point is further downstream, where  $dC_p/dx \approx 0.01 \text{ m}^{-1}$ . An important requirement when designing the test section was to achieve a smooth pressure gradient. From figure 5.1 b) it is clearly seen that this requirement is met.

The set-up aims at a two-dimensional flow, although this is difficult to achieve in a wind tunnel study. The adverse pressure gradient and the separation bubble cause problems. Firstly, the end wall boundary layers grow rapidly due to the APG and interacts with the test plate boundary layer. Secondly, the presence of the separation bubble causes blockage effects.

In order to verify the two-dimensionality of the mean flow in the separation bubble around the section centreline ( $-175 \text{ mm} < z < 175 \text{ mm}$ ) and the temporal stability (in the mean sense) of the bubble a number of  $xy$ -planes and  $xz$ -planes were examined at the position of maximum bubble height. All three APG cases show acceptable two-dimensionality (in  $U$  and  $u_{rms}$ ) and temporal stability in the region around the centreline. Only a  $xz$ -plane of the worst case (III) is presented here. In figure 5.2 a number of spanwise  $U$  profiles traverse the bubble in the wall normal direction. Since there was no need for high quality data to determine whether the velocity varies in the spanwise direction, only 128 image pairs were taken and the profiles look a little wiggly. A tendency of increasing  $U$  with  $z$  can be seen for  $y > 1.5$  mm. According to Hancock (2000) the ratio between the width of the wind tunnel and the length of the separated region should be at least 4 in order to ensure two-dimensionality in case of strong separation. In the present experiments this ratio vary between 0.75 (case III) and 2.5 (case I) and thus the bubble may show some signs of three-dimensionality.

## 5.2. Uncontrolled case

### 5.2.1. Overview of the separated region

An overview of the three investigated separation bubbles is given in table 5, where  $x_s$  and  $x_r$  are the separation and reattachment points, respectively,  $l_s$  is the length of the separated region and  $h_s$  its maximum height. The reattachment point is defined as  $\chi_w \leq 0.5$ . When the pressure gradient increases, the point of reattachment is moving downstream approximately the same distance as the separation point is moving upstream. Thus the position of the

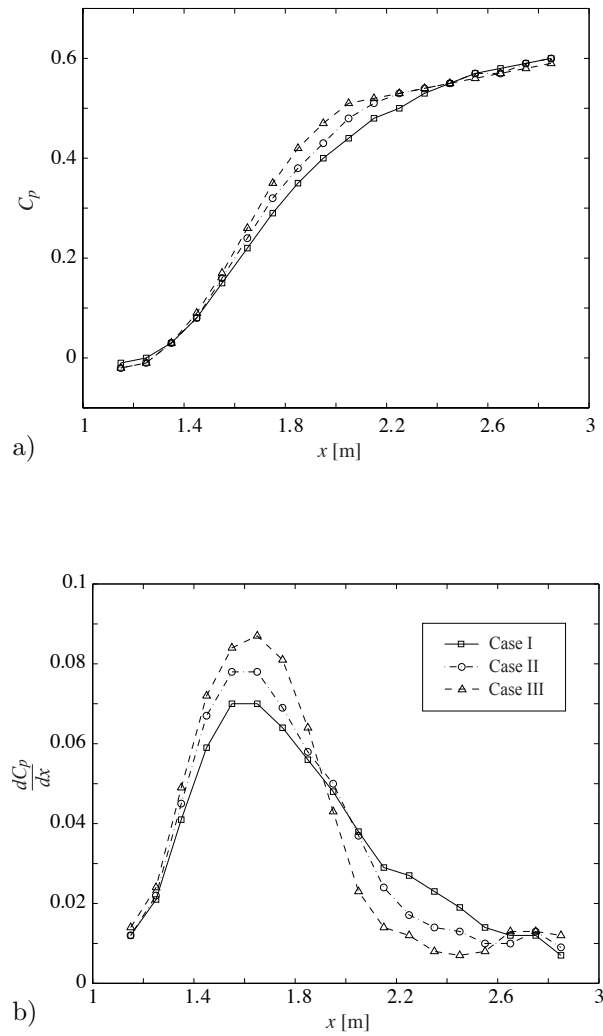


FIGURE 5.1. Pressure gradient in the test section. a)  $C_p$  and b)  $dC_p/dx$  for three suction rates.

separation bubble is almost constant in all three cases. Another feature is that the ratio of the height and the length of the bubble increases with increasing pressure gradient, *i.e.* the bubble becomes thicker.

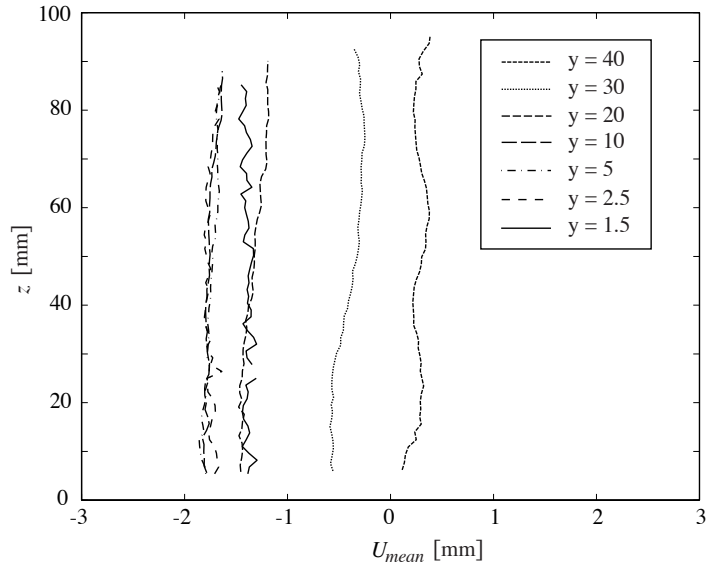


FIGURE 5.2. Mean velocity profiles at different wall normal positions in case III.  $y$  is given in mm.

TABLE 5. Separation bubble size. In case III the point of reattachment is approximated from visual inspection of tufts taped on the test plate. Thus  $x_r$  and  $l_s$  are quite uncertain for case III.

	Case I	Case II	Case III
$(dC_p/dx)_{max}$ ( $m^{-1}$ )	0.070	0.078	0.087
$x_s$ (m)	2.4	2.24	2.09
$x_r$ (m)	2.7	2.85	3.1
$l_s$ (m)	0.3	0.6	1.0
$h_s$ (mm)	7	17	35

In figure 5.3 a), profiles of the mean streamwise velocity are shown at the position of the maximum bubble height for all three different pressure gradients. The profiles all show a similar shape and the free stream velocity is approximately 17 m/s for all cases. That the free stream velocity is almost constant is due to the fact that the suction rate is different, depending on pressure gradient, and compensates for the increasing blockage. The similarity

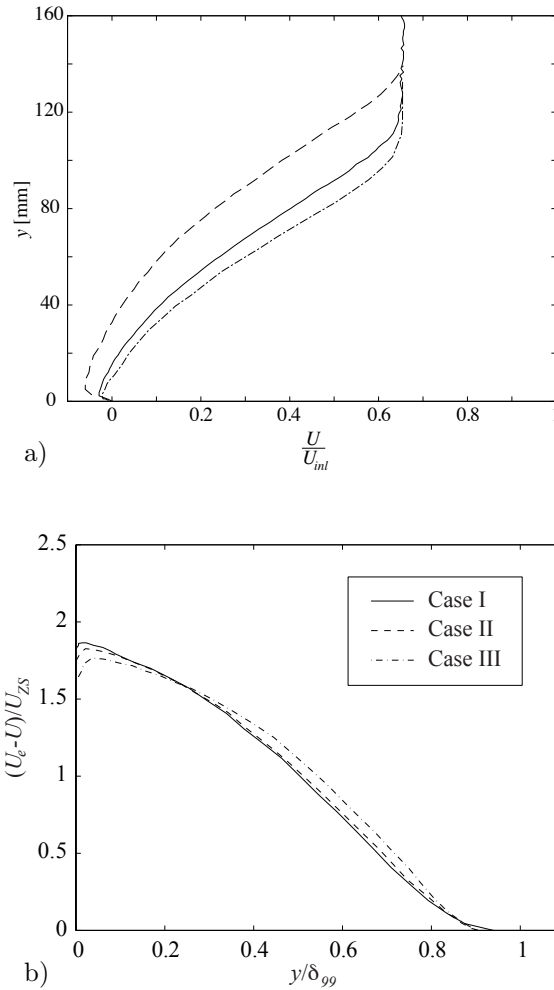


FIGURE 5.3. Streamwise mean velocity at  $x = 2500$  mm in case I (dash-dotted line) and at  $x = 2550$  mm in case II (solid line) and case III (dashed line).

becomes even more apparent when the profiles are plotted using the Zagarola-Smits velocity scale (see equation 2.20) as can be seen in figure 5.3 b).

Case II is the most thoroughly investigated and an overview of its separation bubble is shown in figure 5.4. In the figure the streamwise evolution of the mean velocity profile and the backflow coefficient is presented. A complete

profile was obtained from two slightly overlapping  $xy$ -planes at each position. Since the separation bubble of case II is almost completely covered by measurement planes there is approximately 500 data profiles of which only 5 are shown in the figure. The figure is not to scale and therefore the bubble appear to be about 50% thicker than it is. The point of separation is at  $x = 2240$  mm and the flow reattaches at  $x = 2850$  mm. In section 5.2.3 the procedure to calculate  $\chi_w$  is described in detail. Note that the  $y$ -position where  $\chi > 0$  is moving further out from the wall even after the bubble has passed its maximum height. At the reattachment point,  $y(\chi > 0)$  has moved closer to the wall so it seem to depend on both  $\chi_w$  and  $\delta$  which is perhaps natural. At all  $x$  the position of maximum  $\chi$  is at the data point closest to the wall ( $y = 1.5\text{--}3$  mm) and this is also valid for case I and III. In some experiments (Simpson, Chew & Shivaprasad (1981); Maciel (2006)) the maximum value of  $\chi$  is slightly above the wall in the separated region, but in other experiments (Angele & Muhammad-Klingmann (2006); Amy, Alving & Fernholz (1996))  $\chi_w$  is always the maximum value of  $\chi$ . In the present experiment, however, there are no measurement points close enough to the wall to register such an off-wall maximum, but the shape of the  $\chi$  curve seems to indicate a maximum at the wall.

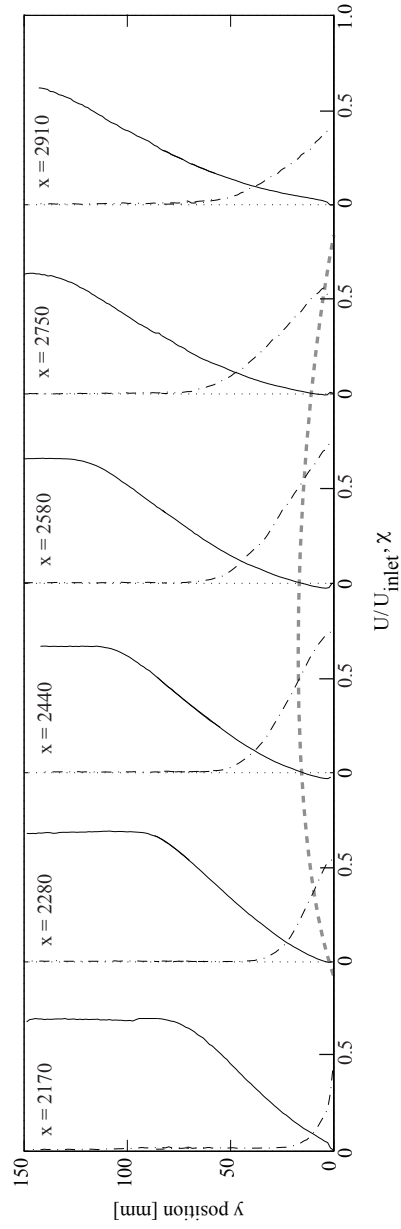


FIGURE 5.4. The separation bubble for the APG case II. The full lines show  $U/U_{inlet}$ , the dash-dotted lines show the backflow coefficient  $\chi$  and the thick dashed line show the region of mean backflow.

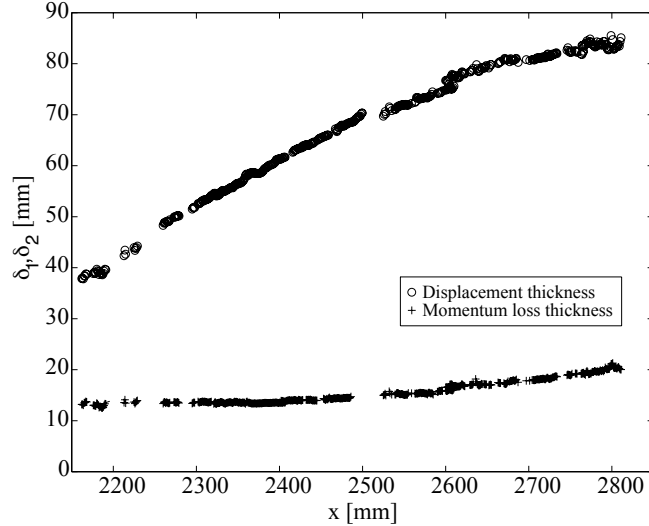


FIGURE 5.5. The development of the displacement thickness and the momentum loss thickness in the separation bubble of case II.

### 5.2.2. The shape factor

Figure 5.6 shows the shape factor  $H_{12}$  as it develops downstream for the three different APG cases. At  $x = 1.0$  m where  $dC_p/dx$  is close to zero  $H_{12}$  is 1.4 in all three cases. There are no pressure measurements at  $x = 1.0$  m, but when extrapolating the curves in figure 5.1 b) it seems likely that  $dC_p/dx = 0$ .  $H_{12}$  increases slowly until  $x = 1.7$ – $1.8$  m and up to that point there are no noteworthy differences between the three cases. Note that the pressure gradient peaks at  $x = 1.6$ – $1.7$  m. Downstream of  $x = 1.8$  m the three  $H_{12}$  curves increases even though the pressure gradient is relaxed. This shows that the boundary layer is able to withstand steep pressure gradients when the velocity profile is still full, but becomes more sensitive as soon as the shape factor increases. The flow separates at  $H_{12} = 3.45$  in case I, at  $H_{12} = 3.50$  in case II and at  $H_{12} = 3.75$  in case III.

Dengel & Fernholz (1990) claim that  $H_{12}$  is 2.85 at the point of separation (for a given bubble size, turbulence level and Reynolds number) and the results of similarity analysis of the outer region of the boundary layer by Castillo & Wang (2004) support this. In an article by Amy *et al.* (1996),  $H_{12}$  at detachment is still near 2.85 with a different pressure gradient history compared to the earlier work in the same wind tunnel (cf. Dengel & Fernholz (1990)).

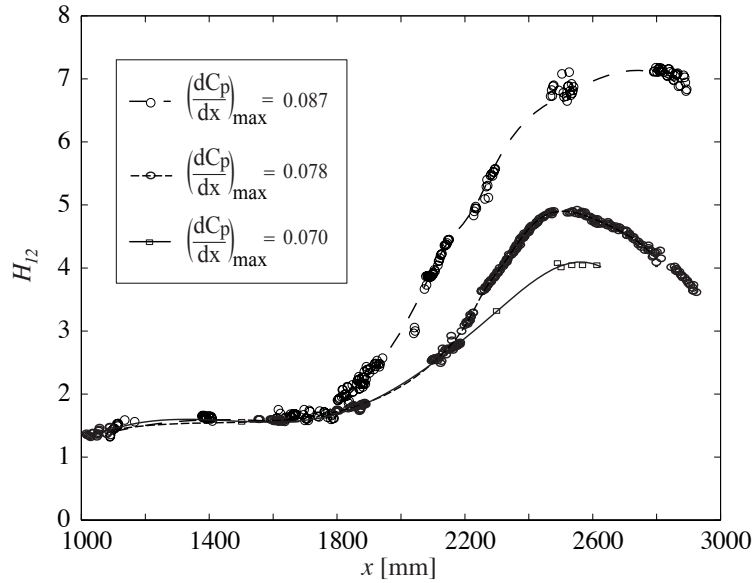


FIGURE 5.6. The development of  $H_{12}$  for the three investigated pressure gradients. The curves connecting the data points are splines added to provide visual aid.

From other experiments (Holm & Gustavsson (1999); Gustavsson (1999); Maciel (2006)), higher values are reported. Thus, the value of the shape factor at detachment does not appear to be universal.

In the present experiment, there seems to be a correlation between the maximum bubble height ( $h_s$ ) and the shape factor at detachment. In figure 5.7, the shape factor at separation is plotted against the bubble height. It is not obvious which parameter is dependent and the line is not to imply that there is a linear relationship between the two parameters. There are too few data points to suggest how  $H_{12}$  at separation varies with the bubble height and furthermore, the bubble height is an arbitrary measure of the separation strength. However, it is clear that the shape factor at detachment increases with separation strength in this set-up. The shape factor peaks in the region  $x = 2.5\text{--}2.6$  m in all APG cases and then starts to decrease. For case II,  $H_{12}$  at reattachment is 4.0, which is higher than at detachment. In Amy *et al.* (1996) the shape factor was 2.85 both at detachment and reattachment, although the value at reattachment was reported to be slightly unstable. This uncertainty is caused by the extreme sensitivity to the pressure gradient in the exact streamwise position of reattachment. Even so, in the present experiments the reattachment position was very stable. The reason for this difference is unknown.

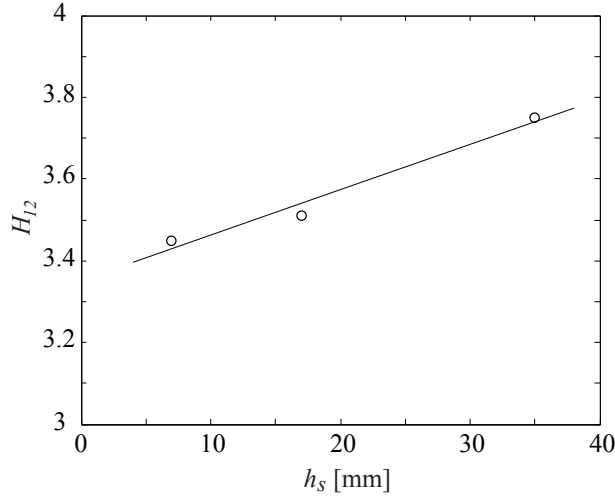


FIGURE 5.7. The circles show the shape factor at detachment as a function of the maximum bubble height. From left to right is case I, II and III.

### 5.2.3. The backflow coefficient

The point of separation was previously defined as the position where the backflow coefficient at the wall  $\chi_w$  reaches 0.5. Unfortunately this parameter is difficult to measure directly with PIV. In this experiment the data point closest to the wall is located at  $y = 1.5\text{--}3$  mm. Since  $\chi$  is a strong function of  $y$ , the  $\chi$ -measurement closest to the wall under-predicts  $\chi_w$ . Dengel & Fernholz (1990) used wall pulsed wires with the sensor wires only 0.03 mm above the wall to obtain an accurate value of  $\chi_w$ . According to their data,  $\chi$  is almost a linear function of  $y$  when  $\chi_w$  is larger than 0.4–0.5. Therefore,  $\chi_w$  here was estimated from a linear fit to the seven data points closest to the wall, as shown in figure 5.8. The described procedure will still under-predict  $\chi_w$ , especially upstream of detachment and result in a slight downstream displacement of the separation point, but  $\chi_w$  in the separation bubble will probably be quite accurate.

Figure 5.9 shows how  $\chi_w$  evolves downstream from  $x = 1.8$  m to  $x = 3.1$  m for case II. Upstream of the figure there is no reverse flow. The curve is built from several measurement planes taken at different times, but the data show a smooth curve, which indicates that the separation bubble is stable. There is a spanwise structure below the test section at  $x = 2.0$  m which makes it impossible to perform PIV measurements in that area. This hides both the incipient detachment (ID) and the intermittent transitory detachment (ITD).

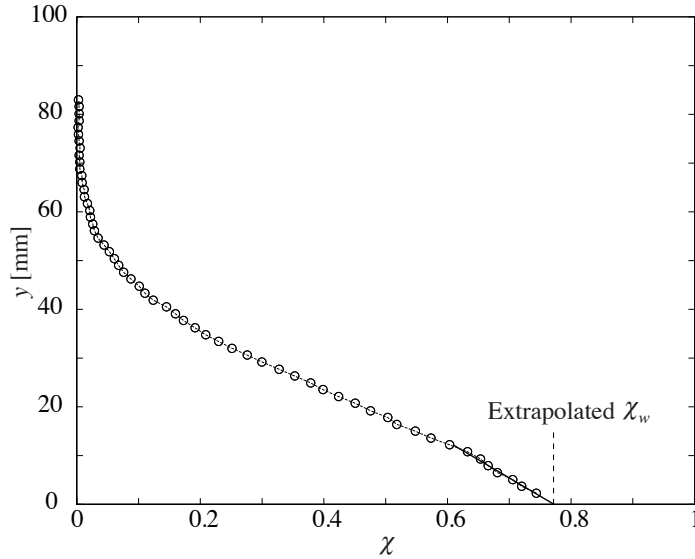


FIGURE 5.8.  $\chi_{wall}$  is extrapolated from the seven data points closest to the wall. This figure show the  $\chi$ -profile at  $x = 2550$  mm for adverse pressure gradient case II.

Since the  $\chi_w$  maximum is about 0.8 a state of steady reverse flow ( $\chi_w = 1$ ) is never reached. In the weaker case I the maximum value of the backflow coefficient is approximately 0.6 and in case III it is 0.9. Figure 5.4 shows  $\chi$  above the wall. The region of backflow events ( $\chi > 0$ ) extends to approximately 50% of the boundary layer thickness at the position of maximum  $\chi_w$ .

Dengel & Fernholz (1990) found a linear relationship between  $H_{12}$  and  $\chi_w$

$$H_{12} = A + B\chi_w \quad (5.2)$$

with  $A = 2.205$  and  $B = 1.385$ . Several other researchers, like Holm, Gustavsson & Muhammad-Klingmann (2000) and Muhammad-Klingmann & Gustavsson (1999), have confirmed this linearity but with other values of the constants. The comprehensive studies by Simpson, Strickland & Barr (1977) and Simpson *et al.* (1981) result in a steeper slope in equation 5.2 with  $A \approx 2$  and  $B \approx 3.5$ . However,  $\chi_w$  is probably under-predicted since their measurement position for  $\chi_w$  is 1.1 mm above the wall. Even so, compensating for this would make the slope even steeper since lower values of  $\chi_w$  are the most under-predicted.

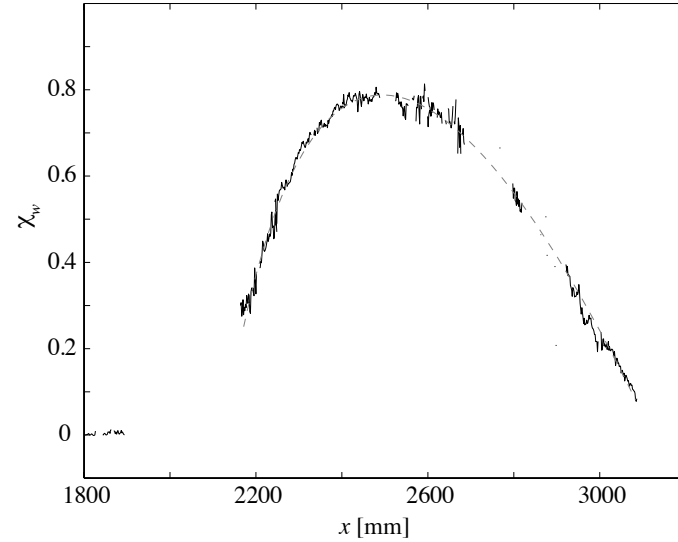


FIGURE 5.9. The backflow coefficient at the wall for case II.  $\chi_w$  is not measured but extrapolated from the data points in the region  $y \approx 1.5\text{--}10$  mm.

The variation of the shape factor for case II as function of  $\chi_w$  are shown in figure 5.10 a).<sup>1</sup> It can be seen in the figure that there exists a linear relationship between the shape factor and the backflow coefficient at the wall; both for increasing and decreasing  $\chi_w$  and  $H_{12}$ . Around the position of maximum bubble height, for  $\chi_w > 0.7$ , the linearity temporarily breaks down. In this case  $A = 1.8$  and  $B = 3.8$ , which agrees better with the results from Simpson *et al.* (1977, 1981) than those of Dengel & Fernholz (1990). This might be due to the fact that the latter experiments are performed in an axi-symmetric test section, without end-walls, whereas the work by Simpson and co-workers were made in a set-up similar to the one used in the present experiments. Note that even though  $\chi_w$  is slightly under-predicted the under-prediction probably decreases linearly with increasing  $\chi_w$ . This would make the inclination of the line somewhat larger, but it would still be linear. An even better fit to the data is achieved with two lines: the first one is fitted to the data points upstream of the bubble maximum and the second one to the data downstream of that position. In figure 5.10 b) the new linear fits are shown and interestingly, they are almost exactly parallel. The linear fit upstream of the maximum bubble

<sup>1</sup>The data from case I and case III are concentrated around the position of the maximum bubble height and there is not enough  $x$ -positions to create a good plot of  $H_{12}$  against  $\chi_w$  in the separated area.

height have the constants  $A = 1.9$  and  $B = 3.2$ . Downstream of the bubble maximum,  $A = 2.4$  and  $B = 3.2$ . Thus, there is an irreversible loss of fullness in the mean streamwise velocity profile because of the separation bubble. This is reasonable since the separation bubble is a large viscous zone resulting in a loss of energy in the mean flow and consequently a less full boundary layer.

As was mentioned previously the above finding is not supported by the data from Amy *et al.* (1996) which show a velocity profile at reattachment that has got the same shape factor as at detachment. On the other hand this behaviour resembles the hysteresis loops presented in the work by Simpson & Shivaprasad (1983). In that study the free stream velocity was varied periodically, generating a time dependent separation bubble, where the decline phase of the bubble always showed a higher value of  $H_{12}$  (for a given  $\chi_w$ ) compared to the growth phase.

It is not obvious that the shape factor and the backflow coefficient at the wall ought to have a linear relationship. Therefore it can be fruitful to look at the displacement thickness and the momentum loss thickness separately. In figure 5.11 a) and b) the integral parameters are plotted against the backflow coefficient. As could be seen earlier in figure 5.5,  $\delta_2$  is nearly constant upstream of the separation bubble maximum height. This is even more emphasized in figure 5.11 b) because  $\chi_w$  increases quickly in this region. Since  $\delta_1$  increases approximately linearly with  $\chi_w$ ,  $H_{12}$  also grows linearly in this region. At  $\chi_w = 0.7-0.8$  the curves turn back and since the momentum loss thickness starts to grow at the same time as the displacement thickness first stops growing and then decreases, the value of  $H_{12}$  decreases. In this area it is less apparent that  $H_{12}$  should evolve linearly. Even so, the  $\delta_1$  and  $\delta_2$  curves seem to arch similarly and thus the ratio will be linear.

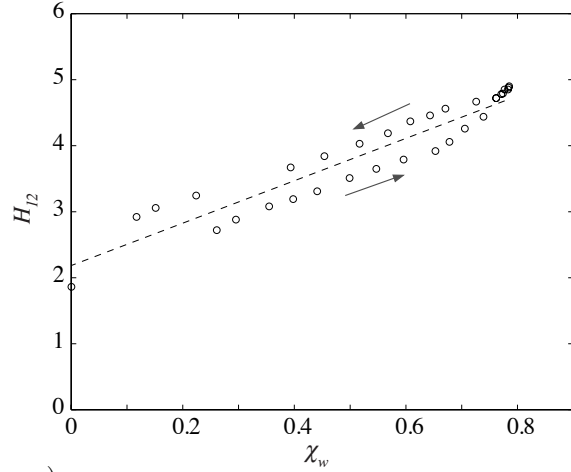
Simpson, Shivaprasad & Chew (1983) found that their data was closely fitted by the function

$$1 - \chi = \frac{1}{2} \operatorname{erf} \left( \frac{h - \bar{h}}{\sqrt{2}\sigma} \right) \quad (5.3)$$

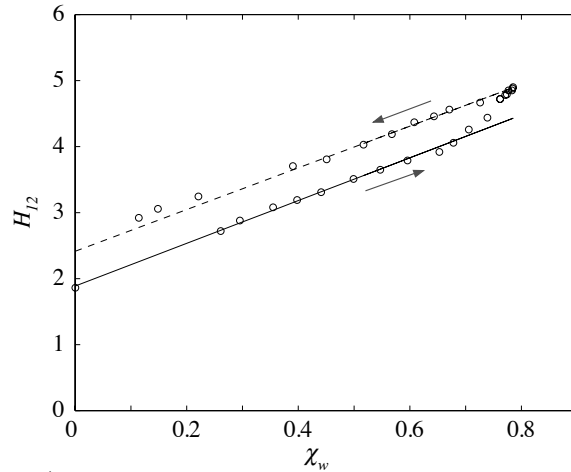
with the normalized shape factor  $h = (H_{12} - 1)/H_{12}$  and the constants  $\bar{h} = 0.73$  and  $\sigma = 0.10$ . The data shown in figure 5.12 from case II deviate very little from this expression. In this figure the hysteresis path mentioned before is even more apparent. It is interesting that the loop in the  $\chi - h$  plane produced by oscillating the free stream velocity closely resembles the one obtained by tracing the flow through a steady separation bubble.

### 5.3. Controlled case

The vortex generators used in the experiments reported here are described in table 1 in section 3.3. It is the same vortex generators as the ones that were used in the ZPG experiments. In the APG case, no cross-plane ( $yz$ )



a)



b)

FIGURE 5.10.  $H_{12}$  plotted against  $\chi_{wall}$  for case II. a) The dotted line shows equation 5.2 with  $A = 1.8$  and  $B = 3.8$ . b) The solid line is a linear fit to the data points upstream of the position of  $\chi_{wall,max}$  and up to  $\chi_{wall} = 0.7$ . The dotted line is a linear fit to the data downstream of the position of  $\chi_{wall,max}$  and up to  $\chi_{wall} = 0.7$ .

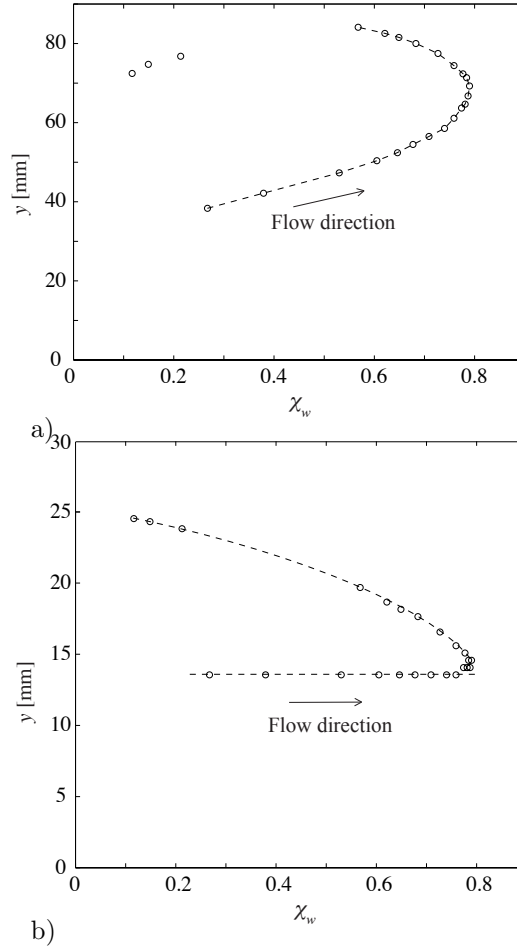


FIGURE 5.11. The displacement thickness and the momentum loss thickness plotted against  $\chi_{wall}$  for Case II. a)  $\delta_1$  b)  $\delta_2$

measurements were made and thus the circulation induced by the VGs could not be directly calculated. Instead the circulation per unit width  $\gamma_e$  is estimated by equation 3.2. According to Angele & Muhammad-Klingmann (2005a) and Angele & Grewe (2002), the measured value is about 60% of that estimated using equation 3.2. In the present set of experiments the circulation in the most upstream measurement from the ZPG data for the three tested VGs are compared to three different circulation estimates in figure 5.13.  $\Gamma_{tot}$  is the absolute streamwise vorticity integrated over the whole measurement plane

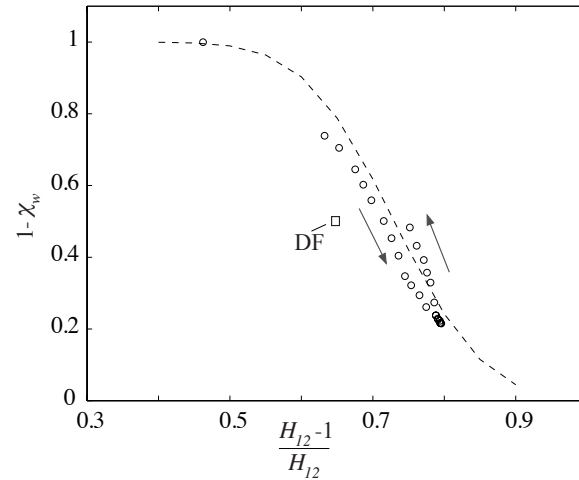


FIGURE 5.12. The data from case II plotted with the fit from equation 5.3.  $\bar{h} = 0.73$  and  $\sigma = 0.10$ . The square labeled *DF* is positioned at the point of separation from Dengel & Fernholz (1990).

and the other two are integrated from the area inside contours of constant  $\omega_x$  and constant  $Q_x$  respectively. Here the circulation calculated from the contour  $Q_x = 0.05 Q_{x,max}$  varies from 55% to 65% of the estimated circulation. No attempt to compensate for this difference between the real value and the value obtained from the equation will be made here. It is sufficient that this estimate seems to work in a consistent way when comparing the relative strength of the vortices produced by different vortex generator configurations.

Because of the rapidly growing boundary layer between  $x = 1.0$  m and  $x = 1.8$  m, the four different sized VG sets can be used to produce any vortex strength up to  $\gamma_e = 6.6$  m/s. A graphic description of this procedure is shown for case III in figure 3.14. The objective of this study is to investigate how the vortices affect the separated area and by changing the streamwise position of the vortex generators, as described above, the distance from the generation of the vortices to the point of separation is also changed. Thus the vortices produced far upstream will evolve and decay over a larger distance compared to vortices produced in a more downstream position. The vortices will also be subjected to different pressure gradients. These issues are discussed later in section 5.3.3.

A majority of the measurements that are presented here are taken at approximately  $x = 2.5$ – $2.6$  m. This is the position of maximum  $\chi_w$  and bubble height and will serve as the reference position when comparing the effect of different values of produced circulation. In all configurations the centre VG

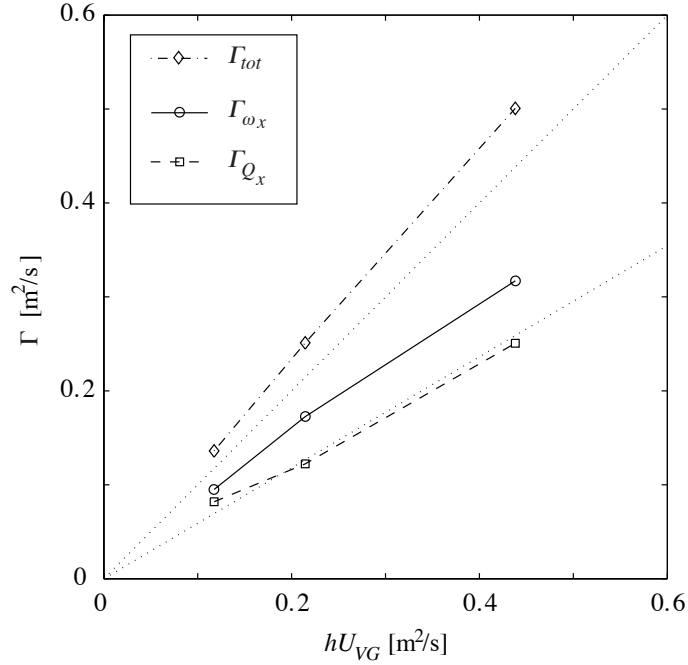


FIGURE 5.13. Circulation generated by 6, 10 and 18 mm vortex generators calculated in three different ways from the ZPG data.  $\Gamma_{tot}$  is calculated by integrating the absolute vorticity over the measured  $yz$ -plane,  $\Gamma_{\omega_x}$  is calculated by integrating the vorticity inside the contour of  $\omega_x \geq 0.1 \omega_{x,max}$  and  $\Gamma_{Q_x}$  is calculated by integrating the vorticity inside the contour of  $Q_x \geq 0.05 Q_{x,max}$ .

pair is positioned at  $z/D = 0$ , which can be seen in figure 5.14 The  $xy$ -planes are all measured at both  $z/D = 0$  and  $z/D = 0.5$ , which are referred to as the position of inflow and outflow, respectively. Obviously their actual  $z$ -position vary depending on VG size. Only for the 10 mm vortex generators there are  $xz$ -plane measurements. They typically cover  $z/D = 0$  to  $z/D = 1$  in the spanwise direction. No measurements in the  $yz$ -plane are reported here. Detailed results from APG case I are thoroughly presented in Angele & Muhammad-Klingmann (2005a) and the focus in this section is on case II and case III.

### 5.3.1. Reverse flow elimination

The main purpose of the vortex generators in separation control is to turn the mean reverse flow into the main flow direction. In figure 5.15 the streamwise

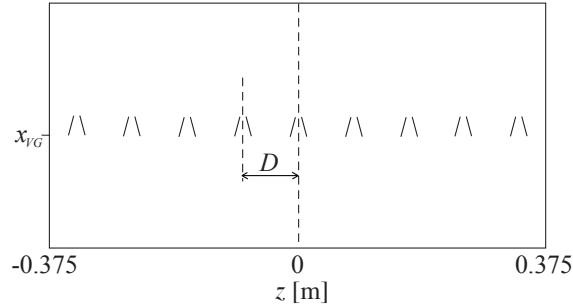


FIGURE 5.14. A top-view of the 10 mm VG array in the BL wind tunnel. All tested arrays are set up like this: the mid pair at  $z = 0$  and the centreline of the outermost pair at a distance  $D/2$  from the wall. The streamwise position of the array is defined as the position of the blade trailing edge.

mean velocity profiles  $U(y)$  at the position of inflow and the position of outflow are shown for some different VG configurations in case II. In table 6, the main characteristics of the five VG configurations are displayed. At the position of inflow, more streamwise momentum is transported downwards through the boundary layer and a slightly larger effect of the VGs can be seen compared to the position of outflow. The two weakest VGs of  $\gamma_e = 1.3$  and  $\gamma_e = 1.7$  have negligible influence on  $U$ , but when the circulation is increased to  $\gamma_e = 2.4$  separation is prevented. The velocity profile might look unaffected, with almost the same shape as a reattaching boundary layer, but figure 5.16 shows that the reverse flow is almost eliminated at the position of inflow and that  $\chi_w$  is about 0.1 at the position of outflow. This is the most efficient VG configuration for preventing separation in this particular flow case, since the drag generated by these VGs is expected to be less than that generated by the stronger VGs. Note how drastically the flow changes due to the relatively small increase in circulation from  $\gamma_e = 1.7$  to  $\gamma_e = 2.4$ . Even though this give a very pronounced efficiency maximum it could also causes a system designed for maximum efficiency to become unstable.

The three configurations with 18 mm VGs at different  $x$  positions, giving  $\gamma_e = 2.4$ ,  $\gamma_e = 5.2$  and  $\gamma_e = 6.4$ , respectively, were used by Angele & Muhammad-Klingmann (2005a) in the same test section as in the present study. The only difference is the stronger pressure gradient causing a larger separation bubble in the present case. Compared to their results, the present data shows less difference in the mean velocity profiles between the position of inflow and the position of outflow, *i.e.* the boundary layer is closer to a two-dimensional state.

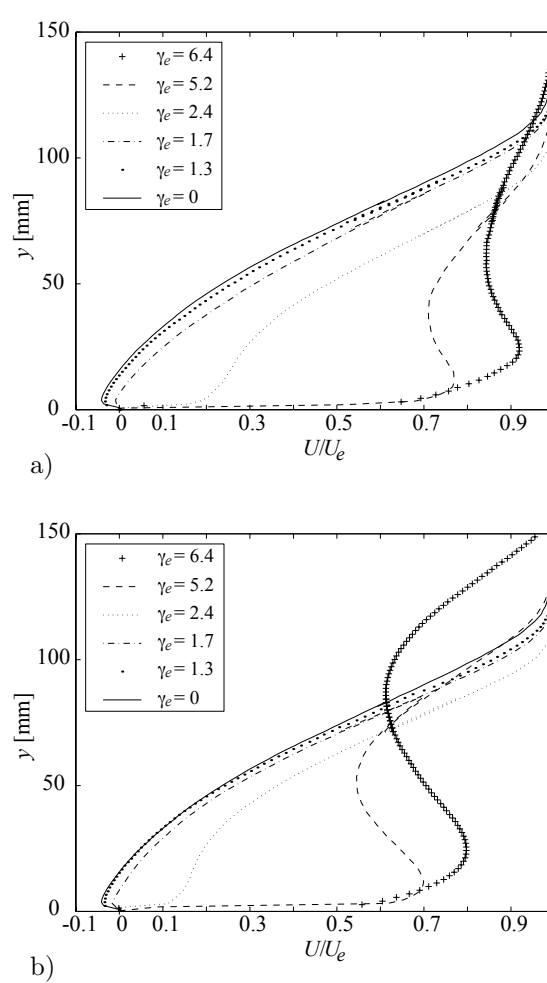


FIGURE 5.15. Streamwise mean velocity for different VGs at the spanwise position of a) inflow and b) outflow at  $x = 2550$  mm.

At  $\gamma_e = 5.2$  and  $\gamma_e = 6.4$  the  $U$ -profiles are clearly S-shaped with a negative velocity gradient region between the outer and inner part of the boundary layer. At the position of inflow, both show larger mean velocity gradients than in a ZPG boundary layer. For  $\gamma_e = 6.4$  the profile is almost plug-like. In this case, the vortices makes the boundary layer substantially thicker, especially at the outflow position. With  $\gamma_e = 2.4$  the boundary layer thickness is reduced, both

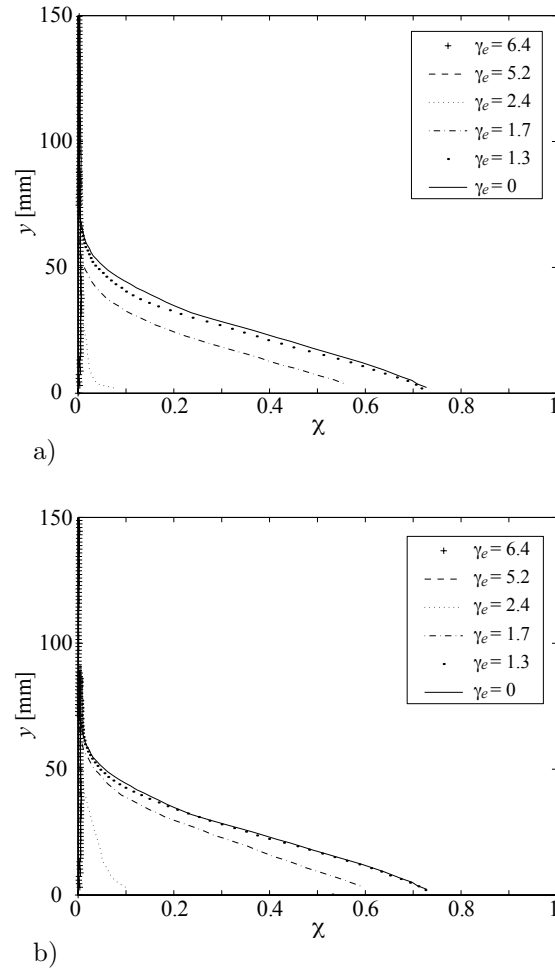


FIGURE 5.16. The backflow coefficient  $\chi$  for different VGs at the spanwise position of a) inflow and b) outflow at  $x = 2550$  mm.

compared to cases with stronger vortices and compared to cases with weaker vortices.

The wall normal mean velocity profiles in figure 5.17 are wiggly due to peak-locking (Angele & Muhammad-Klingmann (2005b)). Since the  $V$ -component is less than a tenth of the  $U$  component the accuracy of the  $V$  data is worse than that of the  $U$  data. However, as expected, the  $V(y)$ -profiles for  $\gamma_e = 3.3$  and 4.7 have a large negative peak near the wall at the position of inflow. The

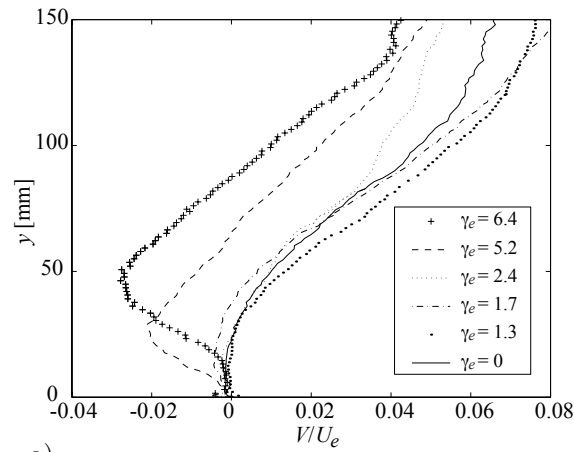
TABLE 6. Description of the VG configurations used in the experiment.

$x_{VG}$ (mm)	$(x_{sep} - x_{VG})/h$	$H_{12,\gamma=0}$	$U_\infty$ (m/s)	$h$ (mm)	$h/\delta$	$h/\delta_1$	$\gamma_e$
1100	66	1.4	26.5	18	1.20	5.4	4.8
1600	38	1.6	25.0	18	0.62	2.8	3.9
2000	16	2.0	20.5	18	0.32	0.9	1.8
2000	28	2.0	20.5	10	0.18	0.5	1.3
2000	47	2.0	20.5	6	0.11	0.3	1.0

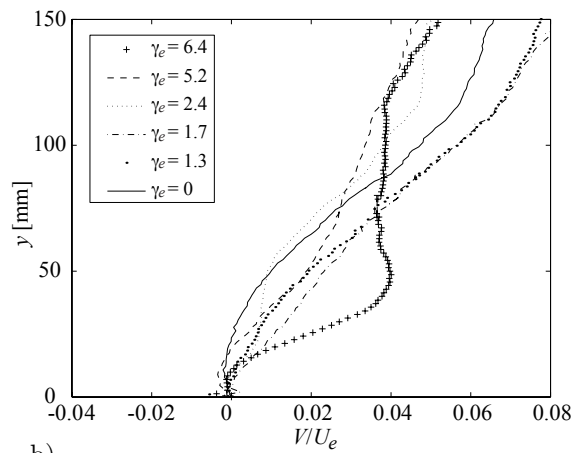
other curves show the same tendency, but it is less clear. At the position of outflow, the strongest VG produces a positive peak, while the others do not seem to change the velocity profile much.

When the pressure gradient is increased, the fullness of the mean velocity profiles at the same level of circulation ought to decrease. A comparison between case II and III at three different values of  $\gamma_e$  is made in figure 5.18. The circulation estimate is not identical in the two cases but close enough to make the comparison meaningful. At all three  $\gamma_e$ -values the flow is attached, but the lower limit is just below the values of  $\gamma_e = 2.4$  in case II and  $\gamma_e = 2.7$  in case III. If the strength of the vortices is further decreased, the flow separates. There is a distinct difference between the position of outflow and the position of inflow for all the three circulation levels. At the inflow location, the  $U(y)$ -profiles are very similar. The free stream velocity is lower in case III, but this is mainly due to the increased suction rate, that changes the free stream velocity when the flow is attached. Note that in the separated cases shown in figure ?? a) the blockage makes the free stream velocity almost constant. At  $\gamma_e = 6.4$  in case II and  $\gamma_e = 6.6$  in case III, the difference between the positions of inflow and outflow is larger, but that is probably due to the high level of mixing, that spreads the difference in the free stream velocity down through the boundary layer. The lower streamwise momentum at the spanwise position of outflow seem to make the flow more susceptible to the increased pressure gradient as can be seen in the right column in figure 5.18. Surprisingly, for the lowest circulation magnitude, the velocity profile for APG case II is more hollow than the one of case III. Another feature of the flow that is visible in the figure is that the increase in circulation results in a thicker boundary layer. This is true for all spanwise positions and at both pressure gradients.

The optimal value of circulation per unit width in APG case III is 2.7 m/s. In figure 5.19 the spanwise distribution of  $U$  for a number of  $xz$ -planes are shown with the optimal level of circulation. This figure is to be compared to the uncontrolled case shown in figure 5.2. Up to  $y = 10$  mm the flow seems



a)



b)

FIGURE 5.17. Wall normal mean velocity for different VGs at the spanwise position of a) inflow and b) outflow at  $x = 2550$  mm.

almost completely two-dimensional and higher up in the boundary layer the difference between the positions of inflow and outflow is still quite small.

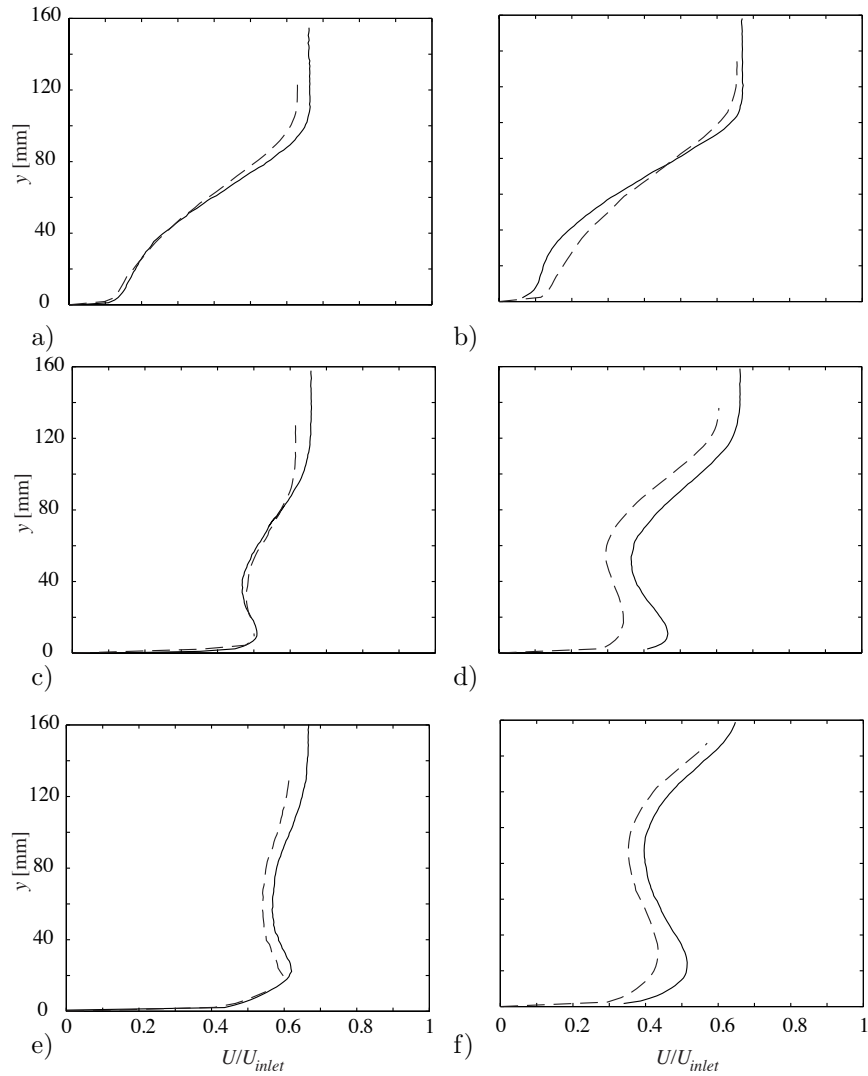


FIGURE 5.18. Streamwise mean velocity at  $x = 2550$  mm in Case II (solid line) and Case III (dashed line) at three different levels of estimated circulation. The first row show  $\gamma_e = 2.4/2.7$  m/s (2.4 refer to the circulation in case II and 2.7 to the circulation of case III) at the position of inflow a) and the position of outflow b), the second row show  $\gamma_e = 5.2/5.3$  m/s at the position of inflow c) and the position of outflow d) and the third row show  $\gamma_e = 6.4/6.6$  m/s at the position of inflow e) and the position of outflow f).

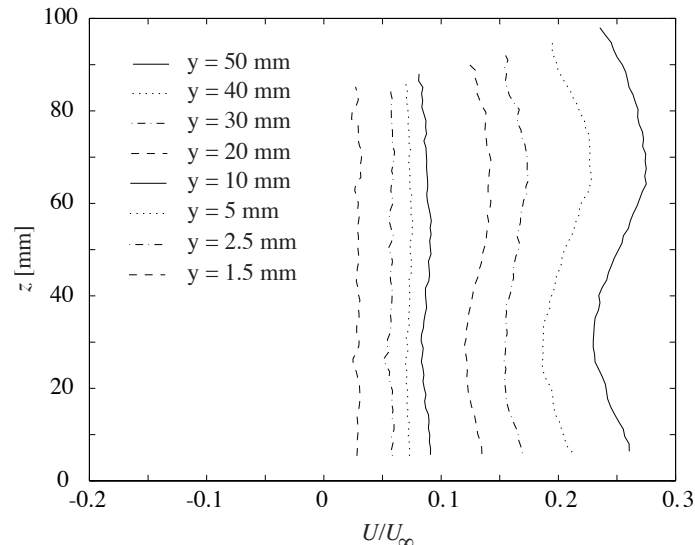


FIGURE 5.19. Streamwise mean velocity profiles at different wall-normal positions.  $x = 2.5$  m and the estimated circulation is  $\gamma_e = 2.7$  m/s.

Figure 5.20 shows what is perhaps the most important set of results in this section. Here the shape factors at  $x = 2.5$  m for case I, II and III are compared at different magnitudes of estimated circulation per unit width. The dashed line displays the result at the spanwise position of outflow and the dotted line the position of inflow. A fuller profile and hence a smaller  $H_{12}$  is expected at the position of inflow. This can be clearly seen in the figure where the two curves are slightly shifted. When there are no vortex generators present in the wind tunnel  $H_{12}$  is about 4, 5 and 7 in the respective cases. If the circulation is increased, something interesting can be seen: the value of the circulation at which the flow stays attached seems to be independent of the pressure gradient. A  $\gamma_e$  of about 2.5 m/s is sufficient in all three cases, even though the difference in size of the separated region is large in the uncontrolled cases. This makes it possible to use a level of circulation that is close to the optimal without risking separation if the pressure gradient changes. When the circulation is further increased, the shape factor levels off to about  $H_{12} = 1.3$  at the position of inflow and to  $H_{12} = 1.5$  at the position of outflow. Above  $\gamma_e \approx 5$  there is little influence on the shape factor from the variation of the pressure gradient.

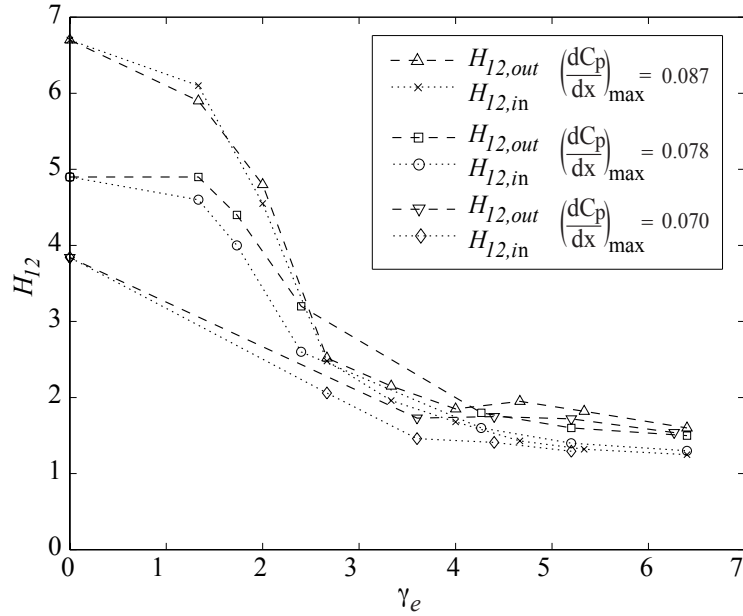


FIGURE 5.20. The shape factor  $H_{12}$  at the position of inflow and the position of outflow plotted against  $\gamma_e$  in case I, II and III. The measurements were made at the respective separation bubble's streamwise position of maximum bubble height.

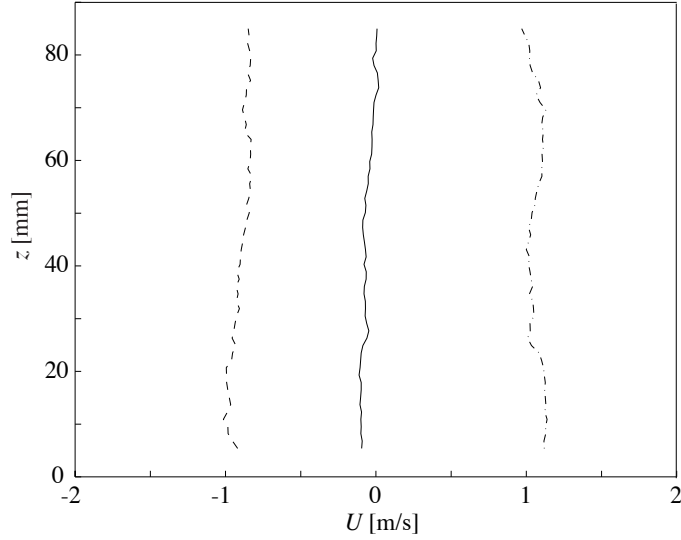


FIGURE 5.21. Streamwise mean velocity in the spanwise direction at  $x = 2.5$  m and  $y = 2$  mm. The pressure gradient is varied to produce three cases: A small backflow ( $U \approx -1$  m/s, dashed line), on the verge of separation ( $U \approx 0$  m/s, solid line) and no separation ( $U \approx 1$  m/s, dash-dotted line).

### 5.3.2. Instantaneous flow

In order to study how the instantaneous flow structures near the wall changes when the flow changes from mean reverse flow to mean positive flow, measurement in  $xz$ -planes at  $y = 2$  mm were performed in varying pressure gradients. Figure 5.21 show the instantaneous spanwise variation in  $U$  for three different pressure gradients. These are new APG cases that are not equal to the earlier cases I, II and III. The new pressure gradients cause a streamwise velocity at  $y = 2$  mm of 1, 0 and -1 m/s, respectively. There are 10 mm vortex generators at  $x = 1.9$  m and the circulation they produce varies around  $\gamma_e = 2$  due to changes in the boundary layer thickness at the position of the VG array when the pressure gradient is adjusted.

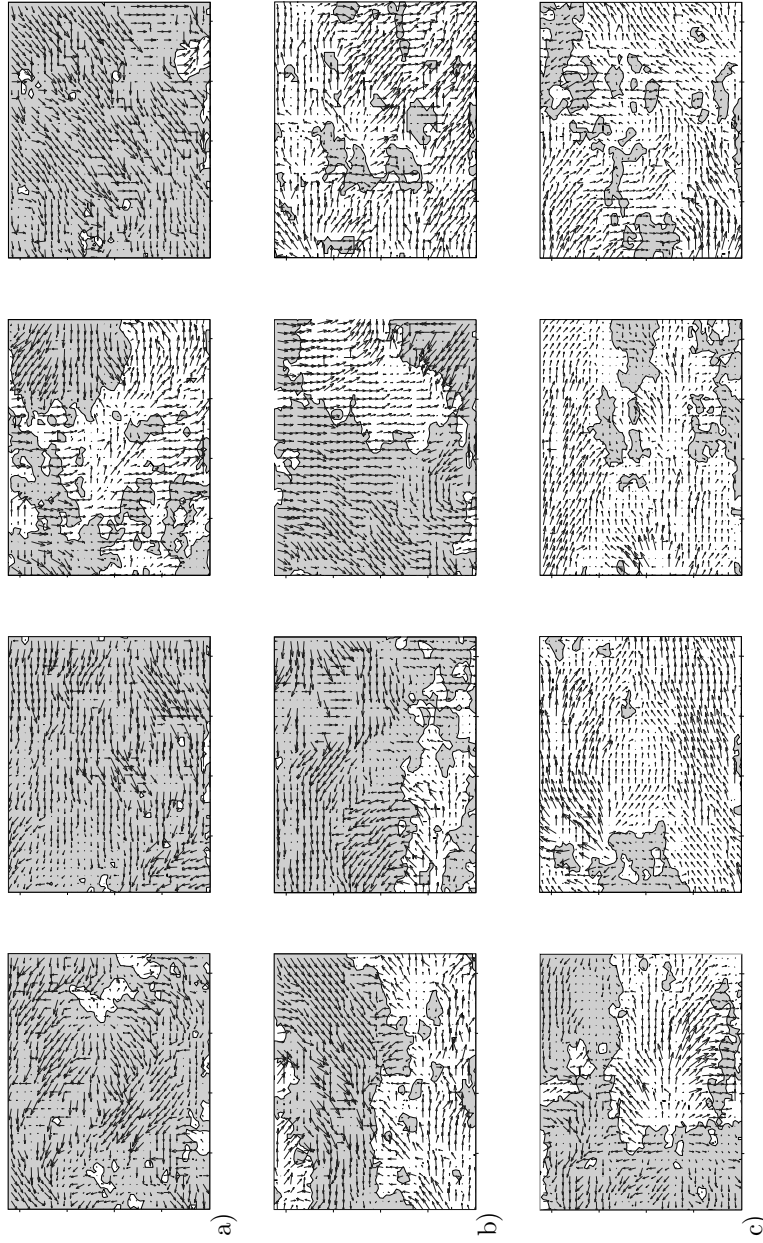


FIGURE 5.22. Instantaneous velocity vectors in a  $85 \times 85$  mm  $xz$ -plane 2 mm from the wall at the streamwise position of maximum bubble height. The grey areas show reversed flow. The pressure gradient is varied to produce three cases: a) A small backflow ( $U \approx -1$  m/s), b) on the verge of separation ( $U \approx 0$  m/s) and c) no separation ( $U \approx 1$  m/s).

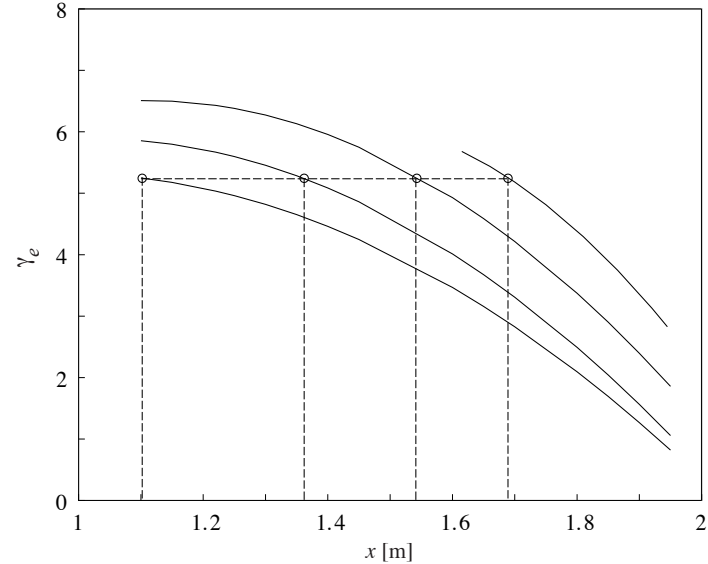


FIGURE 5.23.  $\gamma_e$  generated by the four different VG sizes in case III. The horizontal line indicates  $\gamma_e = 5.2$  and the  $x$ -positions where it intersects with the four lines of estimated circulation shows where the VGs should be placed to generate  $\gamma_e = 5.2$ .

Figure 5.22 a) show a sequence of instantaneous PIV images in an  $xz$ -plane at  $y = 2$  mm in the case of a small amount of mean backflow. This shows that the region of mean separation is built up by sequences of unsteady reverse flow with sudden bursts of positive flow. In figure 5.22 b)  $U = 0$  m/s in the same measurement area and the sequence show more positive flow events. Figure 5.22 c) shows the attached case, but still there are large areas of backflow visible. In all three pressure gradients the flow is ranging from almost fully separated to almost fully attached. The individual images of any of the rows could easily fit into any of the other rows. Thus, it is only in the mean sense that the flow is either attached or detached. Since there is no sign of the longitudinal vortices in the mean flow it is hardly surprising that they make no imprint on the instantaneous images.

Instantaneous images in the  $xy$ -plane give the same overall picture, although with the backflow events mainly taking place near the wall. No such images are presented here, but Angele & Muhammad-Klingmann (2005a) show a longer sequence of images in the middle of the separated region of case I.

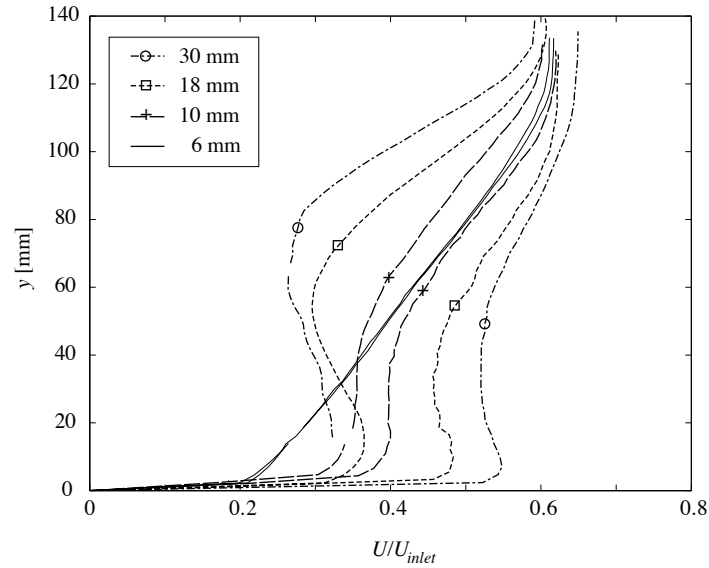


FIGURE 5.24. Mean velocity profiles at the spanwise positions of inflow and outflow for four different VG configurations. The estimated generated circulation is 5.2 for all cases since the VGs are placed at different  $x$ -positions and thus in boundary layers with different profiles. The 6 mm VG is mounted at  $x = 1100$  mm ( $x/h = 230$ ), the 10 mm VG at  $x = 1370$  mm ( $x/h = 120$ ), the 18 mm VG at  $x = 1550$  mm ( $x/h = 55$ ) and the 30 mm VG at  $x = 1700$  mm ( $x/h = 25$ ).

### 5.3.3. Streamwise position

An implicit assumption in the APG chapter of this thesis has been that the streamwise distance from the vortex generator array to the separated region is less important for flow control. This assumption needs to be investigated for the obvious reason of validity of, for example, figure 5.20, but also to know where to apply the VG array in a practical application. If the streamwise position of the vortex generating devices is of minor importance, a separation control system becomes less sensitive to changing boundary conditions.

If the circulation decay shown in figure 4.25 is applicable in the present APG the  $\gamma_e = 6.4$  ( $x_{sep} - x_{VG} = 66h$ ) vortices will have lost 60% of their circulation when they have reached the detachment point of the case II separation bubble. The  $\gamma_e = 2.4$  ( $x_{sep} - x_{VG} = 16h$ ) vortices will only have lost about 20% of their strength. In order to test the influence of the streamwise position of the VG array, the same magnitude of estimated circulation is produced

at four different  $x$ -positions. This is achieved by applying the 6, 10, 18 and 30 mm vortex generators at different streamwise positions so that  $Uh$  at  $y = h$  is kept the same in all configurations (figure 5.23). The normalised distance from the VG array to the measurement position span  $x/h = 25$  to 230 and two arrays are placed before the pressure gradient peak, one is placed at the peak position and one is positioned right after the maximum. In figure 5.24 the resulting mean streamwise velocity profiles at the spanwise positions of inflow and outflow at  $x = 2.55$  m are presented. For the 6 mm VG case the boundary layer has become completely two-dimensional and surprisingly linear. With the 10 mm VG array, the velocity profiles at the position of inflow and the position of outflow is slightly shifted, with a fuller inflow profile. For the next two cases of larger VGs and decreasing  $x/h$ , the shift of the profiles grow larger, which is not unexpected, but the strong symmetry of the  $U$  profiles in the figure is surprising. If an average of the  $U$  profile at the inflow and outflow positions are taken for each VG size the curves of the three largest VGs will almost collapse. Hence, the shape factor of the average mean velocity profiles will most likely be approximately the same. This is shown in figure 5.25, where the shape factor at the inflow and outflow positions are plotted versus the upstream distance to the vortex generator arrays. From this figure it is obvious that considering the large span in normalised streamwise array position the shape factor at  $x = 2.55$  m (approximate position of maximum bubble height) is very stable.

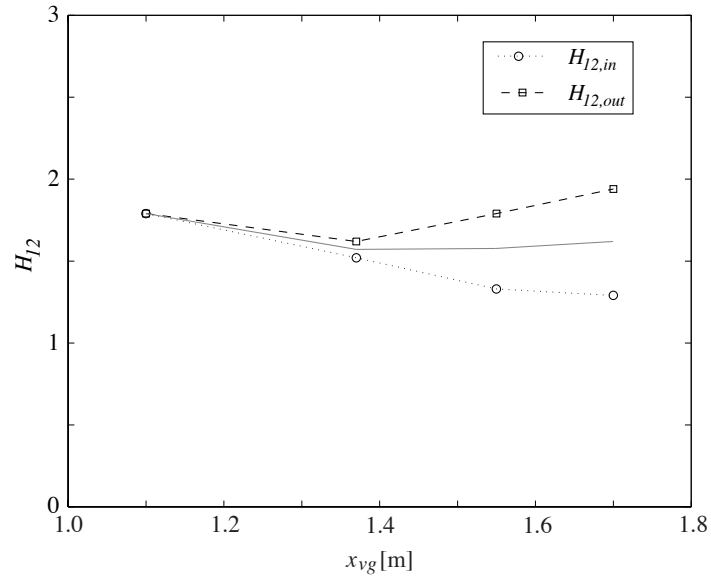


FIGURE 5.25.  $H_{12}$  measured at  $x = 2550$  mm for an estimated generated  $\gamma_e$  of 5.2 m/s. The circulation is produced at four different  $x$ -positions. The upper curve is  $H_{12}$  at the position of outflow and the lower curve is  $H_{12}$  at the position of inflow. The grey line shows the mean  $H_{12}$ .

## CHAPTER 6

### Conclusions

The present work focusses on two aspects of boundary layer separation control using vortex generators. The first aspect is the development of the vortices behind the vortex generators, the influence of their size with respect to the boundary layer thickness, the effect of yaw and also the influence of free stream turbulence. The second aspect deals with the implementation of vortex generators in three different turbulent boundary layers with adverse pressure gradient of different strengths. All three cases will separate without control. The main findings and conclusions are listed below.

#### *Longitudinal vortices in ZPG*

- The vortex paths scales with VG size for a VG array.
- The vortex centres appear to move towards spanwise equidistant positions ( $\Delta z = D/2$ ) after following a path predicted by inviscid theory. The wall normal distance of  $y = D/4$  follow from the vortex equidistance for circular vortices.
- The generation of circulation by the VGs scales excellently with the VG blade height and the velocity at the blade edge.
- The circulation decay levels off after approximately 200 vortex generator heights. At this position the dominant decay mechanism, which is wall friction, has become small due to decreased gradients.
- The magnitude of circulation produced in a VG array is independent of yaw angle due to the linear relationship between generated circulation and angle of attack from  $0^\circ$  to  $35^\circ$ .
- Free stream turbulence of moderate level was found not to affect the circulation generation and only slightly increased vortex circulation decay.

#### *The effect of vortex generators on turbulent boundary layer separation*

- The streamwise position where the VGs are placed was found not to be critical. Thus the VG row can be placed quite far upstream of the controlled region.
- For the three different APG cases approximately the same level of circulation was needed to inhibit separation.

- In the present study there is no evidence of a universal detachment shape factor  $H_{12}$ , that is independent of pressure gradient.
- The detachment shape factor increases with the size of the separated area for the three investigated APG cases.
- There is a linear relationship between the shape factor  $H_{12}$  and the wall reverse flow parameter  $\chi_w$  through the separated region upstream of the maximum bubble height. Downstream of the peak the linear relationship continues with the same slope, but with a somewhat shifted curve. This is valid for APG case II. The amount of data was too sparse to test this on the other configurations.

The present work confirms earlier results that vortex generators are efficient for separation control. However, a drawback is that they produce a penalty drag increase also in situations where no control is needed. A future direction of the work should aim at finding efficient and robust active vortex generators that could be used such that penalty drag is minimised.

## Acknowledgements

First, I would like to thank Scania for financing this project and for letting me come and work there once a week. I appreciate this chance to do some non-academic work once in a while.

I would like to thank my supervisor Prof. Henrik Alfredsson for accepting me as his student and for helping me to see the physics behind the equations. Special thanks to Dr. Kristian Angele for his encouragement and guidance. My assistant supervisor Dr. Jens Fransson is highly acknowledged for helping me to set up the experiment in the MTL wind-tunnel, but especially for teaching me how to perform experiments in a methodical way. Many thanks to all my colleagues at KTH and Scania. I would especially like to thank my former room mate Dr. Thomas Hällqvist.

Finally I would like to thank Cecilia for her love and patience. But also for bringing much needed structure to my life during periods of hard work.

This work has been carried out within the research environment that recently has formed the *Linné Flow Centre*.

## References

- AMY, E., ALVING, A. & FERNHOLZ, H. 1996 Turbulence measurements around a mild separation bubble and downstream of reattachment. *Journal of Fluid Mechanics* **322**, 297–328.
- ANGELE, K. 2003 Experimental studies of turbulent boundary layer separation and control. PhD thesis, Department of Mechanics, KTH, Stockholm.
- ANGELE, K. & GREWE, F. 2002 Investigation of the development of streamwise vortices from vortex generators in APG separation control using PIV. In *11th International Symposium Applications of Laser Techniques to Fluid Mechanics*.
- ANGELE, K. P. & MUHAMMAD-KLINGMANN, B. 2005a The effect of streamwise vortices on the turbulence structure of a separating boundary layer. *European Journal of Mechanics - B/Fluids* **24**, 539–554.
- ANGELE, K. P. & MUHAMMAD-KLINGMANN, B. 2005b A simple model for the effect of peak-locking on the accuracy of boundary layer statistics in digital PIV. *Experiments in Fluids* **38**, 341–347.
- ANGELE, K. P. & MUHAMMAD-KLINGMANN, B. 2006 PIV measurements in a weakly separating and reattaching turbulent boundary layer. *European Journal of Mechanics - B/Fluids* **25**, 204–222.
- CASTILLO, L. & WANG, X. 2004 Similarity analysis for turbulent boundary layer with pressure gradient: outer flow. *ASME Journal of Fluids Engineering* **126**, 297–304.
- COMPTON, D. & JOHNSTON, J. 1992 Streamwise vortex production by pitched and skewed jets in a turbulent boundary layer. *AIAA Journal* **30**, 640–647.
- CUTLER, A. D. & BRADSHAW, P. 1991 A crossed hot-wire technique for complex turbulent flows. *Experiments in Fluids* **12**, 17–22.
- CUTLER, A. D. & BRADSHAW, P. 1993a Strong vortex/boundary layer interactions. part I. Vortices high. *Experiments in Fluids* **14**, 321–332.
- CUTLER, A. D. & BRADSHAW, P. 1993b Strong vortex/boundary layer interactions. part II. Vortices low. *Experiments in Fluids* **14**, 393–401.
- DENGEL, P. & FERNHOLZ, H. H. 1990 An experimental investigation of an incompressible turbulent boundary layer in the vicinity of separation. *Journal of Fluid Mechanics* **212**, 615–636.
- GODARD, G. & STANISLAS, M. 2006 Control of a decelerating boundary layer. Part

- 1: Optimization of passive vortex generators. *Aerospace Science and Technology* **10**, 181–191.
- GUSTAVSSON, J. 1999 Turbulent flow separation. Master's thesis, Department of Mechanics, KTH, Stockholm.
- HÄGGMARK, C. 2000 Investigations of disturbances developing in a laminar separation bubble flow. PhD thesis, Department of Mechanics, KTH, Stockholm.
- GAD-EL HAK, M. 2000 *Flow control. Passive, active, and reactive flow management*. Cambridge University Press.
- GAD-EL HAK, M. & BUSHNELL, D. 1991 Status and outlook of flow separation control, AIAA-91-0037. In *29th Aerospace Sciences Meeting*.
- HANCOCK, P. 2000 Low Reynolds number two-dimensional separated and reattaching turbulent shear flow. *Journal of Fluid Mechanics* **410**, 101–122.
- HOLM, R. & GUSTAVSSON, A. 1999 A PIV study of separated flow around a 2D airfoil at high angles of attack in a low speed wind tunnel. *Tech. Rep.* TN 1999-52. FFA.
- HOLM, R., GUSTAVSSON, A. & MUHAMMAD-KLINGMANN, B. 2000 A PIV study of separated flow around a 2D airfoil. In *9th International Symposium on Flow Visualization*.
- JOHANSSON, A. V. & ALFREDSSON, P. H. 1982 On the structure of turbulent channel flow. *Journal of Fluid Mechanics* **122**, 295–314.
- JOHNSTON, J. 1999 Pitched and skewed vortex generator jets for control of turbulent boundary layer separation: a review. In *The 3rd ASME/JSME joint fluids engineering conference*.
- JOHNSTON, J., MOISER, B. & KHAN, Z. 2002 Vortex generating jets; effects of jet-hole inlet geometry. *International Journal of Heat and Fluid Flow* **23**, 744–749.
- JOHNSTON, J. & NISHI, M. 1990 Vortex generator jets, means for flow separation control. *AIAA Journal* **28**, 989–994.
- KALTER, M. & FERNHOLZ, H. H. 2001 The reduction and elimination of a closed separation region by free-stream turbulence. *Journal of Fluid Mechanics* **446**, 271–308.
- KEANE, R. & ADRIAN, R. 1992 Theory of cross-correlation in PIV. *Applied Scientific Research* **49**, 191–215.
- KHAN, Z. U. & JOHNSTON, J. 2000 On vortex generating jets. *International Journal of Heat and Fluid Flow* **21**, 506–511.
- LIN, J. C. 2002 Review of research on low-profile vortex generators to control boundary-layer separation. *Progress in Aerospace Sciences* **38**, 389–420.
- LIN, J. C., HOWARD, F. G. & BUSHNELL, D. M. 1990 Investigation of several passive and active methods for turbulent flow-separation control. *AIAA 90-1598*.
- LIN, J. C., HOWARD, F. G. & SELBY, G. V. 1989 Turbulent flow separation control through passive techniques, AIAA-89-0976. In *AIAA 2nd shear flow conference*.
- LINDGREN, B. & JOHANSSON, A. V. 2002 Evaluation of the flow quality in the MTL wind-tunnel. *Tech. Rep.* 2002:13. Department of Mechanics, KTH, Stockholm.
- LINDGREN, B. & JOHANSSON, A. V. 2004 Evaluation of a new wind-tunnel with expanding corners. *Experiments in Fluids* **36**, 197–203.
- LÖGDBERG, O. 2006 Flow control in an adverse pressure gradient boundary layer. In *Euromech Fluid Mechanics Conference 6*, p. 374.

- LÖGDBERG, O. & ALFREDSSON, P. 2005 Turbulent boundary layer separation-passive control. In *4th International Symposium on Turbulence and Shear Flow Phenomena. Vol 2*.
- MACIEL, Y. 2006 A study of a turbulent boundary layer in stalled-airfoil-type flow conditions. *Experiments in Fluids* **41**, 573–590.
- MEHTA, R. D. & BRADSHAW, P. 1988 Longitudinal vortices imbedded in turbulent boundary layers, part 2. vortex pair with 'common flow' upwards. *Journal of Fluid Mechanics* **188**, 529–546.
- MILANOVIC, I. & ZAMAN, K. 2004 Fluid dynamics of highly pitched and yawed jets in crossflow. *AIAA Journal* **42** (5), 874–882.
- MUHAMMAD-KLINGMANN, B. & GUSTAVSSON, J. 1999 Experiments on turbulent flow separation. In *IMEchE C557/153/99*.
- ÖSTERLUND, J. M. 1999 Experimental studies of a zero pressure-gradient turbulent boundary layer flow. PhD thesis, Department of Mechanics, KTH, Stockholm.
- ÖSTERLUND, J. M., JOHANSSON, A. V., NAGIB, H. M. & HITES, M. H. 2000 A note on the overlap region in turbulent boundary layers. *Physics of Fluids* **12**, 1–4.
- PANTON, R. 2005 Review of wall turbulence as described by composite expansions. *Applied Mechanics Review* **58**, 1–36.
- PAULEY, W. R. & EATON, J. K. 1988 Experimental study of the development of longitudinal vortex pairs embedded in a turbulent boundary layer. *AIAA Journal* **26**, 816–823.
- PEARCY, H. H. 1961 *Boundary layer and flow control, its principle and applications, Vol 2*, chap. Shock-induced separation and its prevention, pp. 1170–1344. Pergamon Press, Oxford, England.
- RAFFEL, M., WILLERT, J. & KOMPENHANS, J. 1997 *Particle Image Velocimetry. A practical guide*. Springer-Verlag.
- RIXON, S. G. & JOHARI, H. 2003 Development of a steady vortex generator jet in a turbulent boundary layer. *Journal of Fluids Engineering* **125**, 1006–1015.
- SCHUBAUER, G. & SPANGENBERG, W. 1960 Forced mixing in boundary layers. *Journal of Fluid Mechanics* **8**, 10–32.
- SELBY, G., LIN, J. & HOWARD, F. 1992 Control of low-speed turbulent separated flow using jet vortex generators. *Experiments in Fluids* **12**, 394–400.
- SHABAKA, I. M. M. A., MEHTA, R. D. & BRADSHAW, P. 1985 Longitudinal vortices imbedded in turbulent boundary layers. Part 1. Single vortex. *Journal of Fluid Mechanics* **155**, 37–57.
- SIMPSON, R. 1989 Turbulent boundary-layer separation. *Annual Review of Fluid Mechanics* **21**, 205–234.
- SIMPSON, R. L., CHEW, Y. T. & SHIVAPRASAD, B. G. 1981 Structure of a separating boundary layer. Part 1. *Journal of Fluid Mechanics* **113**, 23–51.
- SIMPSON, R. L. & SHIVAPRASAD, B. G. 1983 Structure of a separating boundary layer. Part 5. *Journal of Fluid Mechanics* **131**, 319–339.
- SIMPSON, R. L., SHIVAPRASAD, B. G. & CHEW, Y. T. 1983 Structure of a separating boundary layer. Part 4. *Journal of Fluid Mechanics* **127**, 219–261.
- SIMPSON, R. L., STRICKLAND, J. H. & BARR, P. W. 1977 Features of a separating

- turbulent boundary layer in the vicinity of separation. *Journal of Fluid Mechanics* **79**, 553–594.
- SKOTE, M. & HENNINGSON, D. 2002 Direct numerical simulation of a separated turbulent boundary layer. *Journal of Fluid Mechanics* **471**, 107–136.
- STANISLAS, M. & GODARD, G. 2005 Control of a decelerating boundary layer. comparison of different actuators using PIV. In *4th International Symposium on Turbulence and Shear Flow Phenomena. Vol 2*, pp. 659–664.
- TALAMELLI, A., WESTIN, K. J. A. & ALFREDSSON, P. H. 2000 An experimental investigation of the response of hot-wire X-probes in shear flows. *Experiments in Fluids* **28**, 425–435.
- TAYLOR, H. 1947 The elimination of diffuser separation by vortex generators. Report R-4012-3. United Aircraft Corporation.
- TÖRNBLOM, O. 2006 Experimental and computational studies of turbulent separating flows. PhD thesis, Department of Mechanics, KTH, Stockholm.
- WALLIS, R. 1952 The use of air jets for boundary layer control. Aero note 110. Aerodynamics Research Laboratories, Australia.
- WENDT, B. & HINGST, W. 1994 Flow structure in the wake of a wishbone vortex generator. *AIAA Journal* **32**, 2234–2240.
- WENDT, B., REICHERT, B. & JEFFRY, D. 1995 The decay of longitudinal vortices shed from airfoil vortex generators, AIAA-95-1797. Contractor report 198356. NASA.
- WENDT, B. J. 2001 Initial circulation and peak vorticity behavior of vortices shed from airfoil vortex generators. NASA/CR 2001-211144. NASA.
- WESTPHAL, R., EATON, J. & PAULEY, W. 1985 Interaction between a vortex and a turbulent boundary layer in a streamwise pressure gradient. In *Fifth Symposium of Turbulent Shear Flows*, pp. 266–277.
- WESTPHAL, R., PAULEY, W. & EATON, J. 1987 Interaction between a vortex and a turbulent boundary layer. Part 1: mean flow evolution and turbulence properties. TM 88361. NASA.
- WESTPHAL, R. V. & MEHTA, R. D. 1989 Interaction of an oscillating vortex with a turbulent boundary layer. *Experiments in Fluids* **7**, 405–411.
- YAO, C.-S., LIN, J. C. & ALLAN, B. G. 2002 Flow-field measurement of device-induced embedded streamwise vortex on a flat plate, AIAA 2002-3162. In *1st AIAA Flow control conference*.
- ZAGAROLA, M. 1998 Mean-flow scaling of turbulent pipe flow. *Journal of Fluid Mechanics* **373**, 33–79.
- ZHANG, H.-L., ZHANG, X. & HURST, D. 1996 An LDA study of longitudinal vortices embedded in a turbulent boundary layer. In *8th International Symposium on Application of Laser Techniques to Fluid Mechanics*.
- ZHANG, X. 2000 An inclined rectangular jet in a turbulent boundary layer-vortex flow. *Experiments in Fluids* **28**, 344–354.
- ZHANG, X. 2003 The evolution of co-rotating vortices in a canonical boundary layer with inclined jets. *Physics of Fluids* **15**, 3693–3702.